The Dissertation Committee for Pablo Bianucci
certifies that this is the approved version of the following dissertation:

Optical Resonators and Quantum Dots: An Excursion into Quantum Optics, Quantum Information and Photonics.

Committee:

Chih-Kang Shih, Supervisor

John T. Markert

Gennady Shvets

Xiaoqin Li

Emanuel Tutuc

Optical Resonators and Quantum Dots: An Excursion into Quantum Optics, Quantum Information and Photonics.

by

Pablo Bianucci, Lic.

Dissertation

Presented to the Faculty of the Graduate School of

The University of Texas at Austin

in Partial Fulfillment

of the Requirements

for the Degree of

Doctor of Philosophy

The University of Texas at Austin

August 2007

To my parents, with everlasting gratitude.

To Matilde, my other half.

Acknowledgments

Getting a PhD is like a rollercoaster: it has its ups, its downs and at times it makes you want to throw up. But I finally made it, in no small part due to the support of some special people. First and foremost in the list is my better half, Matilde, for her encouragement and continual inspiration have been very important for me. This dissertation is utterly dedicated to her. Next is my advisor, Ken Shih, whose dedication to his students made this possible. I am also indebted to my fellow labmates, in particular to Andreas Muller, John Robertson and Ned Flagg for their being there when I needed technical help and for our scientific discussions which I have always enjoyed. Triple thanks go to John for proofreading this dissertation. As an experimental physicist, I would not have been able to do any meaningful job without the support from the Machine Shop and the Cryogenics Shop. Jack Clifford was always ready to help me whenever I found creative new ways to ruin a piece, or when I forgot for the n-th time how to make threads in the lathe. Allan Schroeder, Ed Baez and Lanny Sandefur also deserve recognition for their help, as all the machinists do, too. A special nod goes to Dave Elias from the stockroom, who always made shopping for supplies a fun experience. The list of friends in Austin and Argentina would be too long to write down here, but you know who you are. Finally, I want to acknowledge my parents, Ruth and Hugo and my sister Laura for without them I would certainly not be here today. To all these people, from the deepest recesses of my gratitude, please accept a big Thank You!

Pablo Bianucci

The University of Texas at Austin

August 2007

Optical Resonators and Quantum Dots: An Excursion into Quantum Optics, Quantum Information and Photonics.

Publication No. _____

Pablo Bianucci, Ph.D.
The University of Texas at Austin, 2007

Supervisor: Chih-Kang Shih

Modern communications technology has encouraged an intimate connection between Semiconductor Physics and Optics, and this connection shows best in the combination of electron-confining structures with light-confining structures.

Semiconductor quantum dots are systems engineered to trap electrons in a mesoscopic scale (the are composed of $\approx$ 10000 atoms), resulting in a behavior resembling that of atoms, but much richer. Optical microresonators are engineered to confine light, increasing its intensity and enabling a much stronger interaction with matter. Their combination opens a myriad of new directions, both in fundamental

Physics and in possible applications.

This dissertation explores both semiconductor quantum dots and microresonators, through experimental work done with semiconductor quantum dots and microsphere resonators spanning the fields of Quantum Optics, Quantum Information and Photonics; from quantum algorithms to polarization converters.

Quantum Optics leads the way, allowing us to understand how to manipulate and measure quantum dots with light and to elucidate the interactions between them and microresonators.

In the Quantum Information area, we present a detailed study of the feasibility of excitons in quantum dots to perform quantum computations, including an experimental demonstration of the single-qubit Deutsch-Jozsa algorithm performed in a single semiconductor quantum dot.

Our studies in Photonics involve applications of microsphere resonators, which we have learned to fabricate and characterize. We present an elaborate description of the experimental techniques needed to study microspheres, including studies and proof of concept experiments on both ultra-sensitive microsphere sensors and whispering gallery mode polarization converters.

Contents

List of Tables

List of Figures

Chapter 1

Introduction

It all begins with light. Since very early times light has fascinated humans, being an important influence on their life. Consequently, the study of light always attracted the attention of scientists of all ages. In the 20th century, however, the invention of the semiconductor laser and optical fibers and their posterior refinements catapulted light into an even more important role as a medium for the transmission of ever-increasing amounts of information on which societies rely.

The technological revolution of optical communications has intimately connected the fields of Optics (study of light) and Semiconductor Physics (a subfield of Condensed Matter Physics). New advances in the growth of materials have enabled us to create semiconductor nanostructures with features so small that the electrons can be trapped within them causing completely new behaviors to arise. We can also create structures that confine light into small spaces for long times, enhancing many effects that were usually considered to be so small to the point of being negligible.

The combination of electron-confining structures (quantum dots) and light-confining structures (optical resonators) in the micro- and nano-scale is already opening up exciting new areas of research, both basic and applied, and is poised to become an exceedingly important component of areas as diverse as Quantum

Optics, Quantum Information and Photonics.

This dissertation is an attempt to document our journey into these areas, providing some general background into them and describing in detail our contributions.

Chapter 2 describes in certain detail the semiclassical theory of the interaction between light and two-level systems (as models of quantum dots). Chapter 3 reviews the different types of semiconductor quantum dots available today and optical techniques to study them. Chapter 4 includes both a brief introduction to the field of Quantum Information, the applicability of quantum dots to quantum computers and a more detailed description of our implementation of a simple quantum algorithm in a single semiconductor quantum dot. Chapter 5 is a review of the theory of a two-level system coupled with an optical resonator and of the different ways to achieve this system in an experimental setting. Chapter 6 moves away from Quantum Mechanics into Classical Optics by presenting, in a quite detailed way, the theory and practice of microsphere optical resonators. Chapters 7 and 8 discuss applications of microsphere resonators, with proof of concept experiments.

Chapter 2

Interaction between light and a two-level system

Ordinary matter is an extremely complex system, so its interaction with light is also necessarily very complicated. However, most of the physical insights and many useful applications come from considering a much simpler interaction: that of light with a quantum mechanical two-level system. This chapter will introduce a semiclassical theoretical description of this system. A fully quantum mechanical description can be found in Appendix A.

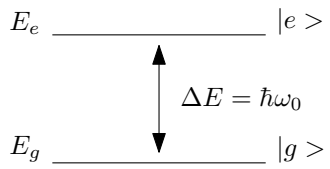

Figure 2.1: Schematic of a two level system.

2.1 The semiclassical Hamiltonian

A two-level system is the simplest possible quantum mechanical system to study. It is just a system that can only exist in two different states (or a superposition of both due to the linearity of Quantum Mechanics), which we will call $|g\rangle$ and $|e\rangle$, as shown in Fig. 2.1. We can start our analysis by formally writing the following Hamiltonian:

$$\hat{H} = \hat{H}_{\text{field}} + \hat{H}_{\text{S}} + \hat{H}_{\text{int}}, \tag{2.1}$$

where the three Hamiltonians correspond to the electromagnetic field, the two-level system and their interaction respectively.

We will always treat the two-level system quantum-mechanically, so the system Hamiltonian is simply

$$\hat{H}_{\text{S}} = E_e|e\rangle\langle e| - E_g|g\rangle\langle g| = \frac{E_e + E_g}{2}\hat{I} + \frac{E_e - E_g}{2}\hat{\sigma_z}, \tag{2.2}$$

where $\hat{I}$ is the identity matrix and $\hat{\sigma_z}$ is a Pauli matrix[135].

If the energy of the electric field is large enough (as is the case for a laser pulse), we can consider it like a classical field with a fixed energy (thus neglecting the field Hamiltonian, as it would be just a constant). The semiclassical interaction Hamiltonian in the dipole approximation (valid when the dimensions of the two-level system are much smaller than the relevant wavelengths of light) is

$$\hat{H}_{\text{int}}^{\text{SC}} = -\hat{\vec{d}} \cdot \vec{E}(t) = -\vec{d} \cdot \vec{E}(t)(|e\rangle\langle g| + |g\rangle\langle e|) = -\vec{d} \cdot \vec{E}(t)(\hat{\sigma}_+ + \hat{\sigma}_-), \tag{2.3}$$

where $\vec{d} = \langle g|e\hat{\vec{r}}|e\rangle$ is the dipole transition moment of the two-level system.

It is reasonable to assume that the field will have a slowly changing envelope modulating a harmonic function so we can write $\vec{E}(t) = \vec{\varepsilon}E(t)\cos(\omega t)$ with $\vec{\varepsilon}$

representing the polarization information. We can then do some algebra

$$\begin{aligned} \vec{d}\cdot\vec{E}(t) &= \vec{d}\cdot\vec{\varepsilon}E(t)\frac{e^{i\omega t}+e^{-i\omega t}}{2} && (2.4)\\ &= \frac{\vec{d}\cdot\vec{\varepsilon}}{2}E(t)(e^{i\omega t}+e^{-i\omega t}) && (2.5)\\ &= \frac{\hbar\Omega(t)}{2}(e^{i\omega t}+e^{-i\omega t}), && (2.6) \end{aligned}$$

defining along the way the Rabi Frequency $\Omega(t) = \frac{\vec{d}\cdot\vec{\varepsilon}}{\hbar}E(t)$.

The full semiclassical Hamiltonian is then given by

$$\hat{H} = \frac{E_e+E_g}{2}\hat{I} + \frac{E_e-E_g}{2}\hat{\sigma_z} - \frac{\hbar\Omega(t)}{2}(e^{i\omega t}+e^{-i\omega t})(\hat{\sigma}_+ + \hat{\sigma}_-). \quad (2.7)$$

Rotating wave approximation

The next step we can take is to transform the Hamiltonian (2.7) into a frame rotating with an angular frequency ωt, using a rotation $\hat{R} = e^{-i\frac{\omega t}{2}\hat{\sigma}_z}$. The new Hamiltonian is $\hat{H}_R = \hat{R}^\dagger\hat{H}\hat{R} - \hbar\omega/2\hat{\sigma}_z$, explicitly

$$\hat{H}_R = \frac{E_e+E_g}{2}\hat{I} + \left(\frac{E_e-E_g}{2} - \frac{\hbar\omega}{2}\right)\hat{\sigma_z} - \frac{\hbar\Omega(t)}{2}(1+e^{-i2\omega t})\hat{\sigma}_+ + (1+e^{i2\omega t})\hat{\sigma}_-. \quad (2.8)$$

The terms that oscillate with frequency $2\omega t$ will have a very small time averaged contribution, so we can neglect them and work in the Rotating Wave Approximation (RWA). Setting the zero energy to eliminate the term proportional to the identity matrix in Eq. (2.8), using that $E_e - E_g = \hbar\omega_0$ and introducing the detuning $\Delta\omega = \omega_0 - \omega$, we obtain the final RWA Hamiltonian:

$$\hat{H}_{\mathrm{SC}}^{\mathrm{RWA}} = \frac{\hbar\Delta\omega}{2}\hat{\sigma_z} - \frac{\hbar\Omega(t)}{2}(\hat{\sigma}_+ + \hat{\sigma}_-). \quad (2.9)$$

2.2 The density matrix formalism: Optical Bloch Equations

The density matrix formalism will allow us to treat the dynamics of the system in a more general way than just solving the Schrödinger equation. In particular, the density matrix can treat open systems which are in constant interaction with an environment that can't be measured (see, for instance, [113], Ch. 4 or [135], Ch. 3). For a two-level system, the density matrix is a 2×2 Hermitian matrix with a unit trace. It can be defined in terms of the $\{|g\rangle, |e\rangle\}$ basis projectors as

$$\hat{\rho} = \rho_{11}|e\rangle\langle e| + \rho_{10}|e\rangle\langle g| + \rho_{01}|g\rangle\langle e| + \rho_{00}|g\rangle\langle g|. \tag{2.10}$$

It is also possible to express it as a linear combination of the identity matrix and Pauli matrices

$$\hat{\rho} = \frac{1}{2}\hat{I} + u\hat{\sigma}_x + v\hat{\sigma}_y + w\hat{\sigma}_z, \tag{2.11}$$

with

$$u = \rho_{01} + \rho_{10}, \tag{2.12}$$

$$v = i(\rho_{01} - \rho_{10}), \tag{2.13}$$

$$w = \rho_{11} - \rho_{00}. \tag{2.14}$$

w is the "population inversion" of the system, while u and v are the dispersive and absorptive components of the dipole moment.

The evolution of the density matrix $\hat{\rho}$ is given by

$$\dot{\hat{\rho}} = -\frac{i}{\hbar}\left[\hat{\rho}, H\right]. \tag{2.15}$$

By inserting Eqs. (2.11), and (2.9) into Eq. (**??**), and by making use of the

Pauli matrices commutation relations, we get

$$\dot{\hat{\rho}} = \dot{u}\hat{\sigma}_x + \dot{v}\hat{\sigma}_y + \dot{w}\hat{\sigma}_z = -\Delta\omega\, v\hat{\sigma}_x + (\Omega(t)w - \Delta\omega\, u)\,\hat{\sigma}_y + \Omega(t)v\hat{\sigma}_z. \tag{2.16}$$

Equating the coefficients for the different Pauli matrices and adding phenomenological decay constants, we arrive at the well known Optical Bloch Equations[5]:

$$\dot{u} = -\frac{1}{T_2}u - \Delta\omega\, v, \tag{2.17}$$

$$\dot{v} = -\Delta\omega\, u - \frac{1}{T_2}v + \Omega(t)w, \tag{2.18}$$

$$\dot{w} = \Omega(t)v - \frac{1}{T_1}w. \tag{2.19}$$

The phenomenological constants T_1 and T_2 represent the population decay time and the dipole decoherence time respectively. In the presence of pure decoherence with a rate γ_d, $T_2^{-1} = T_1^{-1} + \gamma_d$.

2.3 Theory of optical coherent control

2.3.1 The Bloch vector model

The dynamics of a single two-level system in the rotating frame are built into the Optical Bloch Equations (2.17), (2.18) and (2.19). Those equations also give us a pictorial view of the evolution of the system if we consider the three variables as the components of a "pseudo-spin" vector $\vec{\rho} = (u, v, w)$[1] confined to move around a unit radius "Bloch sphere". Then we can rewrite the Optical Bloch Equations into a vector form,

$$\dot{\vec{\rho}} = \vec{G} \times \vec{\rho} - \bar{\Gamma}\vec{\rho} \tag{2.20}$$

[1]The pseudo-spin vector $\vec{\rho}$ should not be confused with the density matrix $\hat{\rho}$.

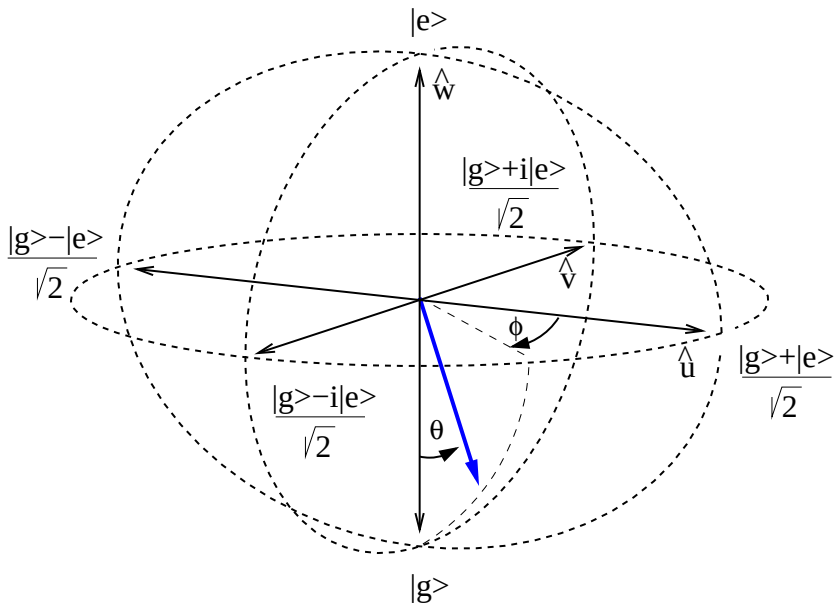

Figure 2.2: Bloch sphere representation of the two-level system.

with a "gyration vector" $\vec{G} = (\Omega(t), 0, \Delta\omega)$ and a "decoherence matrix"

$$\bar{\Gamma} = \begin{bmatrix} \frac{1}{T_2} & 0 & 0 \\ 0 & \frac{1}{T_2} & 0 \\ 0 & 0 & \frac{1}{T_1} \end{bmatrix}. \tag{2.21}$$

The gyration vector works as an "effective magnetic field" for the pseudospin vector, causing it to precess around it, as depicted in Fig. 2.2. In the absence of decoherence the pseudospin vector will have a unit length, staying confined to the Bloch sphere shell. Pure decoherence (represented by T_2) will shrink the vector while population decay (represented by T_1) will cause it to turn downwards towards the south pole.

2.3.2 Rabi Oscillations

Without considering decays ($T_1, T_2 \to \infty$) and exactly on resonance ($\Delta\omega = 0$), Eq. (2.20) has an analytic solution[5]. By defining a dimensionless quantity known as the "input pulse area" as

$$\theta(t) = \int_{-\infty}^{t} \Omega(t')\, dt' \tag{2.22}$$

we obtain the following solutions (for initial conditions $\vec{\rho}(0) = (u_0, v_0, w_0)$):

$$u(t) = u0, \tag{2.23}$$

$$v(t) = w_0 \sin\theta(t) + v_0 \cos\theta(t), \tag{2.24}$$

$$w(t) = -v_0 \sin\theta(t) + w_0 \cos\theta(t). \tag{2.25}$$

This is nothing more than a rotation of the pseudospin vector around the $\hat{u}$ axis. If the incoming light is a pulse so that its total input pulse area is θ, the net effect of the pulse will be to rotate the vector an angle θ (refer to Fig. 2.2 for illustration). Pulses with special values of θ have been given names because of their particular effects:

- $\pi/2$-*pulses* move the vector to the sphere equator, leaving the system in a equally weighted superposition of $|g\rangle$ and $|e\rangle$;
- π-*pulses* rotate the vector all the way up, leaving the system in the $|e\rangle$ state;
- 2π-*pulses* perform a complete rotation of the vector, leaving the system back in its original state.

2.3.3 Matrix propagation for multiple pulse experiments

An important case of coherent control is that performed with sequences of pulses separated in time (usually the pulses are selected from the set of special pulses discussed in the previous subsection). If decoherence can be neglected, there is a

very convenient way to understand the effect of pulse sequences on the two-level system. Even if decoherence is present, the qualitative results from this approach tend to be useful.

The absence of decoherence lets us go back from a density matrix (or pseudospin vector) formalism to a state vector one where the evolution of the system is represented by unitary 2x2 matrices. In this formalism we consider two different types of evolution: instantaneous manipulation pulses and free evolution (meaningful only as a delay between pulses). While in reality the pulses are never instantaneous, as long as they are shorter than the delays involved the results will be valid.

A *θ-pulse* is just a rotation of the pseudospin vector by an angle θ, as mentioned before, and its unitary matrix[2] is just an SU(2) rotation:

$$\hat{U}_\theta = \begin{bmatrix} \cos(\frac{\theta}{2}) & -\sin(\frac{\theta}{2}) \\ \sin(\frac{\theta}{2}) & \cos(\frac{\theta}{2}) \end{bmatrix}. \tag{2.26}$$

The free evolution (during a time τ_d) in the absence of manipulation pulses can be easily found from the free-system Hamiltonian (2.2) (adjusting a global phase for simplification),

$$\hat{U_s}(\tau_d) = e^{-i\frac{\hat{H}_S \tau_d}{\hbar}} = \begin{bmatrix} e^{-i\frac{\omega_0 \tau_d}{2}} & 0 \\ 0 & e^{i\frac{\omega_0 \tau_d}{2}} \end{bmatrix}. \tag{2.27}$$

Composing pulses and delays is as simple as multiplying matrices. A sequence of pulses $\left\{\hat{U}_{\theta_1}, \ldots, \hat{U}_{\theta_N}\right\}$ separated by delays $\{\tau_1, ..., \tau_{N-1}\}$ is represented by

$$\hat{U} = \hat{U}_{\theta_N} \hat{U}_{\tau_{N-1}} \ldots \hat{U}_{\tau_1} \hat{U}_{\theta_1}. \tag{2.28}$$

[2]There is some ambiguity as the basis to use for the matrices. In this dissertation, the correspondence is $|e\rangle \rightarrow (1,0)$ and $|g\rangle \rightarrow (0,1)$.

2.3.4 Quantum Interference

Quantum interference is a general effect occurring whenever the internal phase evolution of a quantum system can affect measurable properties. In the two-level system case, these properties are the populations of the $|g\rangle$ and $|e\rangle$ states (or, equivalently, the population inversion w).

The matrix formalism is appropriate to give us a more quantitative understanding of quantum interference. The simplest case is a two-identical-pulses experiment (see Ref. [32] for an experimental implementation). Both pulses have the same input pulse area θ, and are separated by a delay τ_d. Thus, the corresponding matrix is

$$\hat{U} = \hat{U}_\theta \hat{U}_{\tau_d} \hat{U}_\theta = \begin{bmatrix} e^{-i\omega\tau_d}\cos^2\left(\frac{\theta}{2}\right) - \sin^2\left(\frac{\theta}{2}\right) & -e^{-i\frac{\omega\tau_d}{2}}\sin\theta\cos\left(\frac{\omega\tau_d}{2}\right) \\ e^{-i\frac{\omega\tau_d}{2}}\sin\theta\cos\left(\frac{\omega\tau_d}{2}\right) & \cos^2\left(\frac{\theta}{2}\right) - e^{-i\omega\tau_d}\sin^2\left(\frac{\theta}{2}\right) \end{bmatrix}. \quad (2.29)$$

The final state after the second pulse is $|\psi_f\rangle = \hat{U}|\psi_0\rangle$, and in the case of a initial state $|\psi_0\rangle = |g\rangle$ we have

$$|\psi_f\rangle = -e^{-i\frac{\omega\tau_d}{2}}\sin\theta\cos\left(\frac{\omega\tau_d}{2}\right)|e\rangle + \left[\cos^2\left(\frac{\theta}{2}\right) - e^{-i\omega\tau_d}\sin^2\left(\frac{\theta}{2}\right)\right]|g\rangle. \quad (2.30)$$

When the measured signal is proportional to the amplitude squared of the $|e\rangle$ state, it will show an oscillatory dependence on the delay between the pulses, τ_d. More explicitly,

$$\text{Signal} \propto \sin^2\theta\cos^2\left(\frac{\omega\tau_d}{2}\right). \quad (2.31)$$

In the presence of decoherence, the coherence between the $|g\rangle$ and $|e\rangle$ states is progressively lost during the delay between the pulses, leading to a decaying envelope from which the T_2 decoherence time can be extracted.

Chapter 3

Semiconductor quantum dots

3.1 Quantum confined systems

As material systems decrease in size, quantum mechanical effects become more important in the description of their behavior. For instance, a semiconductor p-n junction (a macroscopic system) can be appropriately described with a semiclassical model[12], but an atom (a microscopic system) is a fully quantum mechanical system. In between these two we can find mesoscopic systems, composed of roughly thousands of atoms, where the distinction is blurred and some features are modified from the bulk ones by their small size. These changes become noticeable when the relevant dimensions of the system approach the DeBroglie wavelength of an electron in the material. Typically, this is on the order of 100 nm at low temperatures, so we can define this length as a "threshold". Structures with at least one characteristic dimension smaller than this threshold will show significant quantum confinement effects.

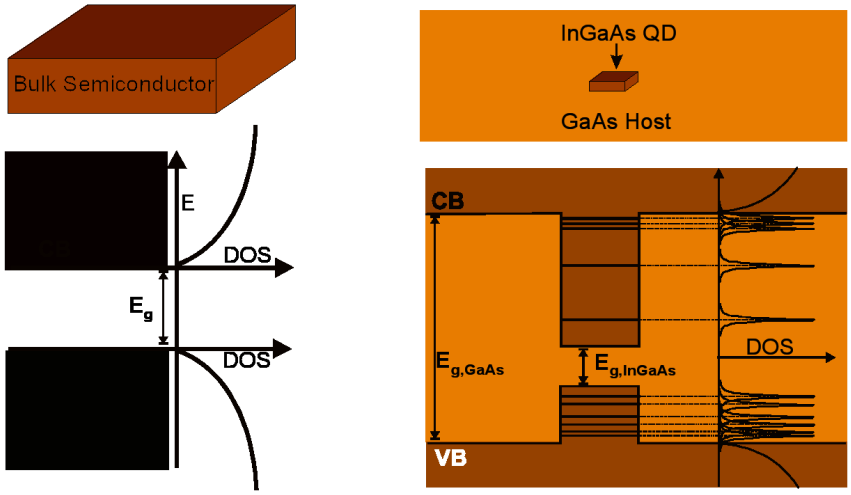

Figure 3.1: Electronic confinement in semiconductor quantum dots (courtesy of H. Htoon and A. Muller).

3.2 Semiconductor quantum dots

When an electron can be strongly confined in all directions, we obtain an effective zero-dimensional object usually called Quantum Dot (QD), whose behavior will be similar to that of atoms in some respects (like a discrete energy structure), but different in others (different kind of transitions allowed, a strongly coupled environment, etc.). Because of this, quantum dots have been also referred as "artificial atoms".

While there are many ways of creating quantum dots, we will restrict our attention to those composed of semiconducting materials, where the confinement in is provided by a spatial variation in the electronic bandgap (see Fig.3.1).

3.2.1 Expitaxially grown quantum dots

Epitaxial growth techniques are currently the best choice to grow high-quality crystalline films. Molecular Beam Epitaxy, in particular, is noted for its ability to grow crystalline materials one atomic layer at a time and is predominantly used to make

nanostructures such as Quantum Wells (QW), where a thin layer (a few nm high) of a low bandgap semiconductor sits between two layers of a higher bandgap one.

Interface fluctuations quantum dots

If the height uniformity of the middle layer of a quantum well is not perfect, after capping it the interface will show small islands of the low bandgap material surrounded on the sides by the higher gap material. This arrangement will provide a weak confining potential in the in-plane direction which coupled to the strong confinement in the growth direction, will create a quantum dot[167, 60, 59]. These quantum dots tend to have large transition dipole moments[73], which makes them interesting in cases where large coupling to electromagnetic fields are useful, such as coupling to an optical microresonator[128] or non-linear spectroscopy studies[145, 16]. These dots are typically made (but not always) of III-V materials such as InAs/GaAs or GaAs/AlAs.

Self-assembled quantum dots

When growing epitaxial layers of a material on top of a substrate with a different lattice constant, the mismatch causes strain that accumulates as the material is deposited. Depending on the materials, different outcomes can happen (for more details, see Ref. [130], Ch. 5). We are interested in the case most common in III-V semiconductors, known as Stranski-Krastanov growth mode. In this mode, after a critical number of layers is grown, the strain becomes so large that the top layers break up into small droplets that allow strain to be released laterally. If these droplets are composed of a material with a smaller bandgap than that of their matrix, they will create a strong confinement potential for electrons due to their small size[129]. Further epitaxial capping of the quantum dots completely embeds them in the matrix, reducing the number of material defects in the interface and

improving their optical properties.

The fabrication of self-assembled quantum dots can be controlled very precisely, allowing control of their shape, density and distribution. However, the grown samples usually show a broad distribution of sizes. Recent advances in growth techniques include vertically[58, 125, 101] and horizontally[21] coupled quantum dot molecules. Self-assembled quantum dots can be made of different materials, but they are most commonly made of InAs in a GaAs matrix. In our experiments, our quantum dots are $In_{0.5}Ga_{0.5}As$ in GaAs[15].

3.2.2 Colloidal quantum dots

Quantum dots can also be prepared in a solution, combining precursors in the appropriate conditions (concentration, temperature, etc.) and letting small particles aggregate[4]. This technique makes nanocrystalline particles of semiconductor material, and proper tuning of the fabrication process permits control of the size and composition of the nanoparticles. The particles can be made of just one material or have a layered structure[4]. They are typically made of II-VII materials (such as ZnSe, CdSe, HgTe, etc.). While the radiative efficiency of these colloidal quantum dots is very high, they show undesirable behaviors like bleaching[157], blinking and spectral diffusion[122].

3.2.3 Lithographically defined quantum dots

Finally, quantum dots can be defined by applying a voltage to lithographically defined gates on top of a quantum well[94]. These quantum dots are better suited to electrical rather than optical manipulation, so we won't discuss them in this work.

3.3 Optical study and manipulation of single quantum dots

The first optical studies of quantum dots were ensemble studies, measuring collective properties of large numbers of dots simultaneously. The advent of single dot spectroscopy opened up an avenue for a more complete understanding of relaxation processes in quantum dots and the optical manipulation of their quantum state. Two main approaches (or a combination of both) are typically used to reach the single dot level: spectral resolution of single dots, taking advantage of the broad distribution of resonant energies due to the broad size distribution of most quantum dot samples; and spatial resolution that involves sub-micron masks or etched mesas to minimize the number of dots involved in the experiment. Many specialized techniques have been devised on top of these approaches for optical studies of the properties of single quantum dots, and it would be outside the scope of this dissertation to enumerate them all. Brief reviews of them can be found in Refs. [120, 175].

3.3.1 Photoluminescence spectroscopy

The most basic technique (which is also the least expensive and most widely implemented) is the Photoluminescence (PL) spectroscopy. In this technique, an excitation laser generates photoexcited carriers which recombine radiatively in the quantum dot. The generated radiation is collected and spectrally dispersed by a spectrometer where sharp lines (due to long decay times) correspond to states of single dots. A wealth of information can be extracted using this technique, such as linewidths[111, 71], temperature dependence of properties[17], behavior under magnetic fields[19], spectral peak identifications (such as distinguishing different exciton shells or biexciton states)[20] among others.

There are several variations, many of which are usually available (sometimes simultaneously) in the same experimental setup:

Non-resonant PL spectroscopy

The excitation laser energy is higher than the host material bandgap so carriers are photoexcited in its conduction band. The carriers are then captured in the quantum dots, eventually relaxing and emitting light as they recombine. Since the dots are "flooded" with carriers, all radiative recombination channels can be observed and the full energy structure can be reconstructed (including higher excited states[106] and biexcitons[84]).

Quasi-resonant PL spectroscopy

In quasi-resonant PL the excitation laser energy is higher than that of the excitonic ground state to study and it is actually resonant with a higher excited state. This excited state is populated by the laser, and this population suffers a fast non-radiative relaxation to the ground state from where it recombines, emitting a photon. Ideally, only one dot is excited so this is a good technique for coherent control[81, 25]. This idea has also been used to study charged excitons[137, 56] and to increase the indistinguishability of photons emitted from a single dot in a microcavity[54].

Imaging PL spectroscopy

This variation involves using an imaging spectrometer instead of a line spectrometer, so that spatial information can be acquired in addition to the traditional spectral information. It is a invaluable tool for working at a single dot level in samples with a large number of quantum dots[82, 83]. Imaging PL is our technique of choice for characterization of single quantum dots without the need to artificially reduce the number of quantum dots in the sample (i.e., by patterning the sample).

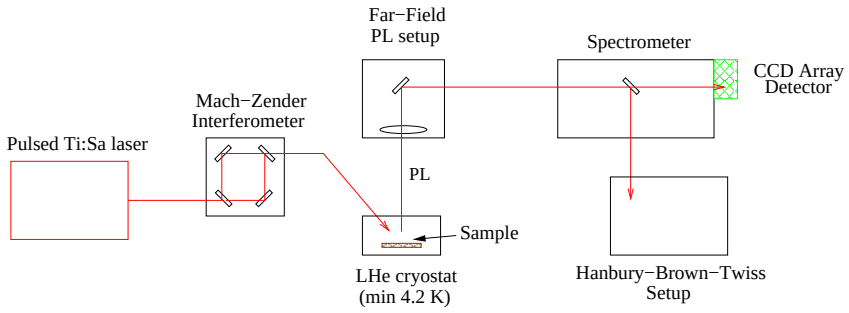

Figure 3.2: Photoluminescence spectroscopy setup.

Figure 3.2 displays a schematic of our experimental setup. We use a Spectra-Physics Tsunami Ti:Sapphire laser, configured in picosecond mode, as our source of light pulses. These pulses are routed through a Mach-Zender interferometer which we use as a pulse splitter to obtain a pair of pulses (with a controllable delay between them) from a single pulse from the laser. These pulses are sent to the sample at an angle of incidence of about 30 degrees from the normal). The quantum dot sample is kept at low temperatures (5 to 10 K) inside an Oxford Instruments MicroStat HiRes liquid Helium continuous flow cryostat. The laser pulses excite the quantum dots and emit PL, which is collected using far field optics (a Mitutoyo ultra-low working distance M-Plan NIR 100X microscope objective and a 20 cm focal length tube lens) and fed into an Acton Research Spectra Pro-500i spectrometer. The spectrometer can be used as a monochromator, directing the wavelength-resolved light into a Hanbury-Brown-Twiss setup[37] to measure its second-order correlation or as an imaging spectrograph, dispersing the light into a 2D liquid nitrogen-cooled CCD detector manufactured by Princeton Instruments. Figure 3.3 shows a sample image obtained in our setup.

Time-resolved PL spectroscopy

It is possible to use the spectrometer as a monochromator, and redirect the emission from a single peak into a time-resolved fluorescence setup. Coupled with a pulsed

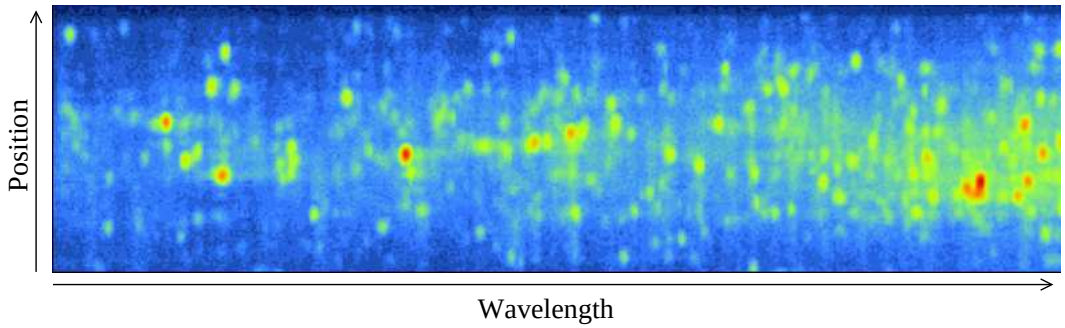

Figure 3.3: Spectrographic image of single quantum dots. The bright peaks correspond to emission from single quantum dots.

excitation, this enables direct measurement of the radiative decay times (T_1) of quantum dots[13].

3.3.2 Photoluminescence excitation spectroscopy

Photoluminescence Excitation spectroscopy (PLE), consists in monitoring the emission of a target state (peak in the spectrum) as the excitation laser scans a range of energies. Strong PLE peaks are related to efficient relaxation channels between different states, and the technique has been very useful in studying relaxation mechanisms in quantum dots[59, 60, 80, 153].

3.3.3 Side excitation spectroscopy

While PL is very versatile for studying linear properties, is has a fundamental drawback: If the light emitted by the quantum dot is at the same wavelength of the excitation laser, which is orders of magnitude stronger, the signal will be drowned in the "noise" of the scatered laser light so there is no "Resonant PL spectroscopy". Recently, in an effort leaded by Dr. A. Muller, our group developed a Resonant PL spectroscopy technique for quantum dots embedded in a planar microcavity using side excitation. This technique has been used to observe Mollow fluorescence[114]

in single quantum dots[116] A detailed description of the technique and its implementation can be found in Ref. [120].

The excitonic ground state has much longer coherence times than the higher excited states. Using this approach for manipulation of the ground state then would allow for better quantum operations in quantum dots.

3.3.4 Our PL spectroscopy setup

3.3.5 Experimental realizations of coherent control

The first experiment in optical coherent control of quantum dots involved two-pulse quantum interference to manipulate the excitonic state[32]. The next cornerstone in the coherent manipulation of single quantum dots came with the demonstration of Rabi oscillations in interface fluctuation quantum dots[144] and Rabi oscillations coupled with quantum interference in self-assembled quantum dots[93, 81]. Since then, different experimental paths on Rabi oscillations have been pursued to improve the quality and number of the observed oscillations. These paths involve improved PL experiments[164], photodiode photocurrent spectroscopy[176], two-photon Rabi oscillations[149], polarization discriminated oscillations[119] and even non-linear four-wave-mixing techniques[34, 127].

The observation of up to 10π Rabi oscillations using PL[164] was instrumental for studying damping of the oscillations, implying an important role of the wetting layer as the intensity of the laser pulses increases. Weak transitions between the continuum wetting layer states and the bound quantum dot states might introduce decoherence channels as the laser becomes more intense, similarly to previously reported effects[80, 153, 159]. However, the damping of the Rabi oscillations remains somewhat controversial, as other mechanisms such as phonon-assisted damping[57] and wetting layer mediated processes[161] have been proposed.

Chapter 4

Quantum dots and quantum information

The ability to quickly process information has led to technological revolutions that would have seemed impossible just a few decades ago. This rapid pace of advancement can be summarized in the so called "Moore's law", an empirical observation by Intel founder Gordon Moore noting that the number of transistors in a microprocessor seems to double every 24 months[115]. This exponential increase is still ongoing, but fundamental physical limitations will certainly slow it down in the near future. One possible way to work around these limitations is to employ quantum mechanical features for processing information. This idea, initially suggested by Richard Feynman[55], has spurred enormous amount of both theoretical and experimental work in order to probe its abilities, limitations and practical feasibility. This chapter will first briefly introduce the basics of this vast field and then discuss how semiconductor quantum dots fit within it, closing with a description of an experimental implementation of a quantum algorithm on a single quantum dot.

4.1 A brief introduction to Quantum Information

The most important branches of Quantum Information are Quantum Computation, dedicated to using quantum systems to process information, and Quantum Cryptography, the study of using Quantum Mechanics for the secure distribution of messages. This work will mostly discuss the former. Those looking for a more complete exposition can find an exhaustive introduction to the field in the textbook from Nielsen and Chuang[123].

4.1.1 Classical versus quantum bits

The minimal unit used for information is called a "bit". A classical bit is a system that can be in either one of two states, usually called "0" and "1". A classical computer takes a string of classical bits in a given initial state, manipulates them and returns a result in the form of a new state of the bits. A quantum bit (qubit for short) is a quantum mechanical system that has two possible states, $|0\rangle$ and $|1\rangle$. Analogously to the classical case, a quantum computer takes a string of qubits in a given state, manipulates them (through a unitary evolution) and then returns the result in the quantum state of the qubits.

What makes a quantum computer different than a classical one? There are, roughly, three main differences between classical computers and quantum computers.

Massive parallelism

The linearity of quantum mechanics means that if the state of a qubit is a linear superposition of the basis states ($|\psi\rangle = \alpha|0\rangle + \beta|1\rangle$), the evolution of the quantum computer will be just the superposition of the evolution of the basis states ($\hat{U}|\psi\rangle = \hat{U}\alpha|0\rangle + \hat{U}\beta|1\rangle$). This means that a quantum computer can run a "quantum program" using all possible inputs at the same time. A classical computer is limited to running using a single input per run.

Interference

Even though Quantum Mechanics allows us to run a quantum computer using all possible inputs simultaneously, it does not let us extract all the answers together (thanks to the properties of quantum measurements). However, it is possible to extract useful information from the superposition of results with a proper use of interference between quantum amplitudes. This is not present in classical computers, since they give just one result at a time.

Entanglement

Entanglement is a very intriguing property of Quantum Mechanics, with absolutely no classical analog. It is a property of many-body quantum systems, that have states which cannot be described as a simple product of single-particle states. Entangled states show correlations which are stronger than those predicted by any local theory[22, 42]. While it is a subject of ongoing research, there is a certain belief that entanglement plays a critical role on quantum information processing[123].

4.2 Using Quantum Dots as quantum bits

Quantum dots give us a good approximation to a two-level system, so we can use them as qubits by identifying the absence of an exciton (state $|g\rangle$ from Ch. 2) with the qubit state $|0\rangle$ and the presence of it ($|e\rangle$) with the qubit state $|1\rangle$. As it was also discussed in Ch. 2, the interaction with an electric field gives us the means to optically control the qubit. Short resonant laser pulses can move the pseudospin vector along a meridian in the Bloch sphere, and the use of detuned pulses would allow the vector to explore the rest of the sphere. However, there is a more interesting way of achieving this. If we go back (after doing the RWA) from the rotating frame into the laboratory frame, we'll see that the free-evolution of the

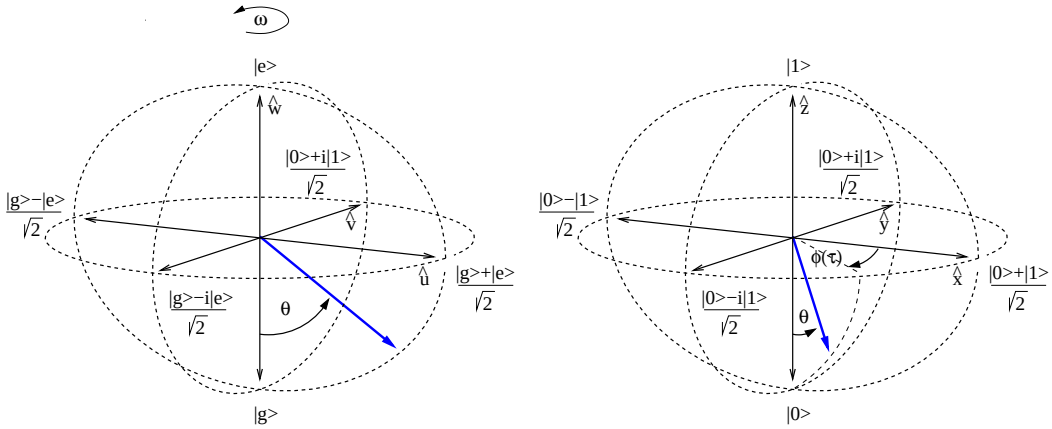

Figure 4.1: Comparison between the Bloch sphere (right) and the qubit sphere (left).

pseudospin vector is to precess around the $\hat{z}$ axis. It then stands to reason that the motion of the vector due to a resonant pulse will depend on the precise moment in which it arrives to the quantum dot. Proper timing of the appropriate pulse can then move the vector to an arbitrary position within the sphere. By moving back into the laboratory frame sphere, which we will call "qubit sphere" (see Fig. 4.1), we gain fast "free"[1] qubit rotations around the $\hat{z}$ axis. Combining it with pulses that change the latitude (θ angle) of the vector, we can do arbitrary manipulation of the state of the exciton.

4.2.1 Quantum dots and the DiVincenzo criteria

Any physical quantum system that can be taken (exactly or in an approximate way) as a two-level system can be used as a qubit. However, if we want the system to be the basis of a reasonably practical quantum computer, it has to satisfy certain criteria, introduced by D. P. DiVincenzo in 2000 [49]. According to these criteria, a physical system appropriate for scalable quantum information processing has to:

1. Be a scalable physical system with well-defined qubits.

[1]The cost to pay for the "free" operations is the precise timing required for any manipulation, but it is acceptable as it is in NMR quantum computing[45].

2. Be initializable to a simple fiducial state such as $|000...\rangle$.

3. Have decoherence times much longer than the time required for operations.

4. Have a universal set of quantum gates.

5. Permit high quantum efficiency, qubit-specific measurements.

There is more than one way to define an optically controllable qubit in a quantum dot. The initial proposals considered the two-level system composed by the excitonic ground state and the excitonic vacuum state (crystal ground state) as a qubit[155, 27, 110]. More recently, proposals and experiments have been oriented towards utilizing the spin of an electron trapped in a charged quantum dot as a qubit[40]. This spin qubit can be controlled directly using Electron Spin Resonance (ESR) techniques[100] or indirectly via optical Raman assisted spin flips[50]. The rest of this chapter will refer to excitonic qubits.

Requirement 1: Scalability

The scalability of a qubit depends strongly on the particular scheme used to implement it. For instance, it is possible to implement an n-qubit system using a quantum dot with 2^n non-degenerate excitonic states (as it was done in the 2-qubit implementation of a two-qubit gate[105]), but it would not be a scalable scheme because the number of required states would increase exponentially with the number of qubits. A scalable scheme would be one where there is only one exciton per quantum dot, so the number of quantum dot required increases only linearly with the number of qubits. Each quantum dot would need a somewhat different resonant energy to permit individual manipulation or to be precisely spatially located so that the excitation and measurement could be restricted to it (or maybe a combination of both). There are no fundamental issues against this scheme, just matters of practical considerations (like the number of lasers needed) and materials

science. Recent advances that have enabled the growth of quantum dots in ordered arrays[75, 96, 169] suggest that the materials issues might eventually be solved.

Requirement 2: Initialization

Initialization of excitonic qubits is simple. Since the exciton vacuum state $|g\rangle$ is defined to be the $|0\rangle$ state, the initialization procedure is just to let any remaining population decay (thermal population, even at room temperature, would be negligible) so that all qubits go to the $|0\rangle$ state. Given the typical radiative decay times of self-assembled quantum dots (on the order of 1 ns), this would be a "slow" operation, but it would be acceptable as an initialization process.

Requirement 3: Decoherence times

How many operations can be performed within the decoherence time is a critical qualification of any would-be qubit. Excitons have short radiative lifetimes, but short operation times somewhat compensate for that. An overly optimistic estimation of the decoherence time of an exciton (using the excitonic ground state, not a higher excited state which will make it shorter) is around 1 ns. The operation time depends on the kind of operation: Rotations around $\hat{z}$ are very fast, with a full rotation taking exactly one optical period ($\approx$ 6 fs), while latitude rotations usually take around 10 picoseconds. The operation time is limited by the slowest rotations, so it will be on the order of 10 picoseconds. It would then be possible to fit 100 operations in the decoherence time using this scheme. In an experiment, we were able to estimate a number of 18 operations during the decoherence time of a quasi-resonantly excited quantum dot[165]. Theoretical studies on quantum error correction have estimated coarsely that if about 10^4 operations can be implemented on a qubit before its decoherence time, then the said qubit can be used to perform "fault-tolerant" quantum computation[98]. Thus, we see that the prospects of fault-

tolerant quantum computers using excitons in quantum dots are not very bright. Future advances in fabrication (increasing the decoherence times) and manipulation (allowing for faster manipulations without deleterious effects) might improve this and change the situation.

Requirement 4: Universal set of quantum gates

A universal set of quantum gates is a discrete set of unitary operations that can be applied to a set of qubits so that a sequence of these operations can approximate an arbitrary unitary evolution of the qubits[123]. There is not a single universal set, but one of them is composed by arbitrary single qubit operations and a two-qubit entangling gate (such as Controlled-NOT or Controlled-ROT). We have seen already that arbitrary single qubit operations can be implemented in quantum dots (and some have been, as the Rabi oscillations in Refs. [144, 93, 81, 176] have shown). However, two-qubit entangling gates are a more problematic issue. While a two-qubit CROT gate was implemented in a single quantum dot[105], in order for our quantum dot quantum computer to be scalable we would need to implement a two-quantum dot gate. Entanglement has been experimentally demonstrated in vertically coupled quantum dots[18] but it is not clear that the vertically coupled quantum dots will be able to scale well. There have been many theoretical proposals for entangling gates with laterally coupled quantum dots, but no experimental demonstrations yet. Again, materials science might hold the key for solving this issue, as new methods for growing laterally coupled quantum dot molecules are being demonstrated[21].

Requirement 5: High efficiency qubit-specific measurements

Finally, we have to address the issue of qubit measurement. In principle, excitons in quantum dots give us an excellent readout of their state as they will only emit a photon when their are in the $|1\rangle$ state. If the quantum dots are distinguishable in

either energy or spatial location (or both), it is also possible in principle to make the measurement qubit specific. The limitations in the efficiency of the measurement lie in practical considerations such as imperfect collection of the emission and limited quantum efficiency of the single photon detectors which might be sidestepped by clever algorithm design and multiple executions of the experiment.

Requirements summary

In summary, most of the requirements can be satisfied in principle and are limited by material or practical considerations which might be lifted in the future. Requirement 4 might have some fundamental obstacles, but more research is needed to find out. Requirement 3, the number of operations that can be performed within the decoherence time, presents more of a fundamental roadblock as solid state systems tend to have short decoherence times and the operations cannot be performed fast enough (without affecting even more the quantum coherence of the system[164, 161])to reach the required threshold for fault-tolerant quantum computing. While there might be some breakthrough allowing this obstacle to be overcame, other qubit implementation schemes (such as the spin of electrons trapped in quantum dots[87], trapped ions[95, 30] or superconducting qubits[47, 143]) show more promise as a building blocks of a realistic quantum computer.

4.3 Experimental realization of a quantum algorithm in a quantum dot

While it is not clear at all that excitons in quantum dots will ever result in a workable multi-qubit quantum computer, we can still use them as single-qubit quantum computers (and maybe even as two-qubit computers for the right problems). This will not solve any practical problems, but it is useful as a tool to study both quan-

tum information and the dynamics of quantum dots. One particular problem that is well suited to be solved in a single-qubit computer is the Deutsch problem.

4.3.1 The Deutsch problem

The Deutsch problem[46] involves global properties of binary functions on a subset of the natural numbers. Given a natural number N, we can define a set $\{X_N\}$ with all the natural numbers that can be represented with N bits. A binary function $f : X_N \to \{0, 1\}$ is called balanced if it returns 0 for exactly half of the elements of X_N and 1 for the other half. Given a function that is either balanced or constant, the Deutsch problem consists of finding out which type it is. A general classical algorithm requires evaluating the function on more than half of the elements, requiring at least $2^{N-1} + 1$ evaluations. This causes the classical run time to grow exponentially with the input size.

The $N = 1$ case can be cast in a more "realistic"(and intuitive) way. Let's suppose we are given a coin which can be either genuine or fake. A genuine coin will have both a head and a tail, while a fake one will have either two heads or two tails. We can actually map a coin to a 1-bit function f_c in the following way: $f_c(0) = 0$ means the top side of the coin is a head, while $f_c(0) = 1$ means it is a tail. Similarly, $f_c(1) = 0$ if the bottom side is a head and $f_c(1) = 1$ it is is a tail. For a fake coin $f_c(0) = f_c(1)$, so f_c will be constant, while for a real coin f_c will be balanced. Thus, finding out whether a given coin is genuine or fake is equivalent to solving the Deutsch problem in 1 bit.

4.3.2 The Deutsch-Jozsa algorithm

The Deutsch-Jozsa algorithm provides a way to solve the Deutsch problem on a quantum computer using a quantum subroutine that evaluates f. The problem and its solution provide an example of Oracle-based quantum computation[24, 23],

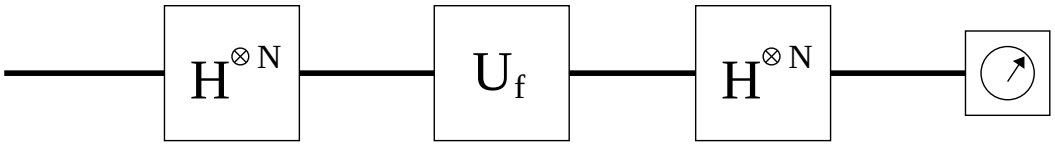

Figure 4.2: Optimized version of the Deutsch-Jozsa algorithm.

where it is assumed that a quantum subroutine or Oracle contains the information about the unknown function. The algorithm gives a recipe on how to prepare (encoding) and read out (decoding) the qubit in an efficient way. In an experimental demonstration, we have not only to implement the algorithm (encoding and decoding operations), but we also have to build the Oracle. The specific structure of the Oracle, encoding and decoding is not unique and several versions can be found in the literature[46, 41, 43, 44]. The one we are using here[44] allows us to implement the N=1 case with a single qubit.

Figure 4.2 shows a quantum circuit depiction of the algorithm. This circuit uses the following quantum transformations:

1. A Hadamard transformation independently applied to each qubit, $\hat{H}^{\otimes N} = \hat{H} \otimes \ldots \otimes \hat{H}$. A single qubit transformation is represented by

$$\hat{H} = \frac{1}{\sqrt{2}} \begin{bmatrix} 1 & 1 \\ 1 & -1 \end{bmatrix}. \tag{4.1}$$

2. A f-controlled gate, whose operation is defined as

$$\hat{U}_f|x\rangle = (-1)^{f(x)}|x\rangle. \tag{4.2}$$

The final step in the algorithm measures the expectation value of the $|0\rangle\langle 0|$ operator. This expectation value for a constant function will be equal to 1 while for a balanced function it will be equal to 0. When N=1 there are only four possible functions

$f_j : \{0,1\} \to \{0,1\}$:

$$f_1(x) = 0, \tag{4.3}$$

$$f_2(x) = 1, \tag{4.4}$$

$$f_3(x) = x, \tag{4.5}$$

$$\text{and } f_4(x) = 1 - x. \tag{4.6}$$

Of these four, f_1 and f_2 are constant while f_3 and f_4 are balanced. The explicit matrix forms of the $\hat{U}_f$ operators are:

$$\hat{U}_{f_1} = \begin{bmatrix} 1 & 0 \\ 0 & 1 \end{bmatrix} = \hat{I}, \quad \hat{U}_{f_2} = -\begin{bmatrix} 1 & 0 \\ 0 & 1 \end{bmatrix} = -\hat{I}, \tag{4.7}$$

$$\hat{U}_{f_3} = \begin{bmatrix} 1 & 0 \\ 0 & -1 \end{bmatrix} = \hat{\sigma_z}, \text{ and } \hat{U}_{f_4} = -\begin{bmatrix} 1 & 0 \\ 0 & -1 \end{bmatrix} = -\hat{\sigma_z}. \tag{4.8}$$

We can see that the balanced functions share the same f-controlled operator except for a global phase. This is also true for the constant functions. If the qubit is initially in the state $|0\rangle$, the encoding transformation consists in one Hadamard operation that transforms the qubit to

$$\frac{1}{\sqrt{2}}(|0\rangle + |1\rangle). \tag{4.9}$$

By applying $\hat{U}_{f_j}$ to the state in Eq. 4.9 we obtain

$$\hat{U}_{f_j}\frac{1}{\sqrt{2}}(|0\rangle + |1\rangle) = \frac{1}{\sqrt{2}}[(-1)^{f_j(0)}|0\rangle + (-1)^{f_j(1)}|1\rangle]. \tag{4.10}$$

For a constant function this gives

$$(-1)^{f_j(0)}\frac{1}{\sqrt{2}}(|0\rangle + |1\rangle), \tag{4.11}$$

while for a balanced function we get

$$(-1)^{f_j(0)}\frac{1}{\sqrt{2}}(|0\rangle - |1\rangle). \tag{4.12}$$

As a decoding procedure, we apply again the Hadamard transformation. We obtain

$$(-1)^{f_j(0)}|0\rangle \tag{4.13}$$

for a constant function, and

$$(-1)^{f_j(0)}|1\rangle \tag{4.14}$$

for a balanced function. Therefore, by measuring one of the two states, one can decide in a deterministic way to which class f belongs. We remark that if we were to obtain an answer using only classical operations, we would need to evaluate the unknown f function twice, obtaining both $f(0)$ and $f(1)$ and then comparing them. Conversely, the described quantum procedure only requires one call of the quantum subroutine $\hat{U}_f$. Therefore the N=1 case of the Deutsch-Jozsa algorithm already shows that the quantum algorithm outperforms its classical counterpart by a factor of two in the number of evaluations.

4.3.3 Implementation in a single quantum dot

We have been able to implement the single-qubit Deutsch-Jozsa algorithm discussed above using the excitonic states of a self-assembled InGaAs quantum dot as a qubit. The level scheme we used is depicted in Fig. 4.3. The absence of an exciton is taken as the $|0\rangle$ state of the qubit, while the first excited excitonic state is taken as $|1\rangle$. The $|1\rangle$ state population is monitored via a non-radiative transition to the exciton ground state (labeled as $|1'\rangle$) whose radiative recombination is recorded using a micro-photoluminescence setup[82, 79, 80, 81, 119].

We will use two different unitary transformations to realize the Deutsch-Jozsa

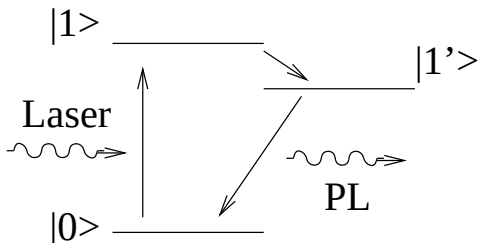

Figure 4.3: Quantum level structure. The excitonic ground state and first excited state are labeled $|1'\rangle$ and $|1\rangle$ respectively. The state $|0\rangle$ corresponds to the absence of an exciton in the quantum dot.

algorithm: a $\frac{\pi}{2}$ single qubit rotation and a phase shift. The corresponding explicit matrix forms are (as introduced in Sec. 2.3.3):

$$\hat{U}_{\frac{\pi}{2}} = \frac{1}{\sqrt{2}} \begin{bmatrix} 1 & -1 \\ 1 & 1 \end{bmatrix} \tag{4.15}$$

and

$$\hat{U}(\phi) = \begin{bmatrix} e^{-i\frac{\phi}{2}} & 0 \\ 0 & e^{i\frac{\phi}{2}} \end{bmatrix}. \tag{4.16}$$

The single qubit rotation is realized by a $\pi/2$ pulse resonant with the $|0\rangle$ to $|1\rangle$ transition. The phase gate $\hat{U}(\phi)$ is realized by controlling the phase of the optical pulses with respect to the first pulse which is used as a reference. This is achieved experimentally by a piezoelectric translation stage that controls the phase locking between the pulses. By choosing specific values for ϕ, $\hat{U}(\phi)$ becomes equivalent to the f-controlled operators, as shown in Table I. In this version of the algorithm, the Oracle distinguishes the operations within the same class only by a global phase in the single qubit space. We can always think about an additional reference qubit in the Oracle to make this phase physically measurable. However, this reference qubit will never come into play in the real algorithm since it is part of the internal structure of the Oracle.

Notice that although $\hat{U}_{\frac{\pi}{2}}$ and $\hat{H}$ behave in a similar way, they are not the same operator. It is easy to show that the only effect of this change is that the interpretation of the final result has to exchange balanced with constant functions. We can think about the quantum evolution of the qubit during the algorithm using the picture of a pseudo-spin in the qubit sphere. The first pulse corresponds to an effective magnetic field in the $+\hat{y}$ direction that brings the pseudo-spin from $-\hat{z}$ to the $-\hat{x}$ direction. The phase shift corresponds to a rotation of the pseudo-spin around the $\hat{z}$ axis in multiples of π. The second pulse will bring the pseudo-spin back to the $-\hat{z}$ direction in the case of a balanced function (by destructive interference), and to the $+\hat{z}$ direction in the case of a constant function. In this picture the N=1 Deutsch algorithm shows clearly its equivalence to a Mach-Zehnder interferometer experiment[43].

The sample consisted of $In_{0.5}Ga_{0.5}As$ MBE grown self-assembled quantum dots, kept at a temperature of 5 K inside a continuous flow liquid helium cryostat. The quantum dots were resonantly excited with pulses from a mode-locked Ti:Sa laser. The pulses were linearly polarized in a way to make sure only one state out of an anisotropy induced doublet was excited[119]. By using a spectrometer combined with a two-dimensional liquid nitrogen cooled charge-coupled device (CCD) array detector, we were able to detect the integrated photoluminescence signals of many quantum dots at the same time[79]. This enabled us to search for a quantum dot with a large enough dipole moment (and thus a good signal-to-noise ratio) and a dephasing time larger than 20 ps for the excited state, which is the case for about 1% of the dots. We did not select any specific polarization at the detection.

The use of the excitonic ground state photoluminescence as the means of detection prevented us from being able to use this state as the $|1\rangle$ state of our qubit. This entailed a severe decrease in the dephasing time of the qubit, as the non-radiative decay from the excited state to the exciton ground state (necessary

for our detection scheme to work) puts an upper bound in the coherence time of the exciton[2]. This upper bound is significant, since measured dephasing times for excitonic ground states are on the order of hundreds of picoseconds[33, 28, 17] while those for carefully chosen excited states (i.e. no further than approximately 20 meV apart from the corresponding ground state) range in the tens of picoseconds[80].

The actual implementation of the algorithm was similar to that of standard wave packet interferometry measurements[32, 93], but in the nonlinear excitation regime[81]. In order to establish the appropriate excitation intensity for a $\frac{\pi}{2}$ pulse, we first recorded Rabi Oscillations of the excited state[93, 81]. We also performed a low intensity wave packet interferometry measurement to estimate the dephasing time of the quantum dot[32, 93]. In that experiment, the photoluminescence signal is proportional to the wavefunction autocorrelation. By fitting the decay of the autocorrelation signal with an exponential function we were able to measure the dephasing time of the exciton in the dot, obtaining 40 ps as a result.

In the main experiment, the time delay between two identical resonant $\frac{\pi}{2}$ laser pulses (approximately 5 ps long) was scanned while simultaneously recording the photoluminescence. A mechanical translation stage controlled the coarse delay between the two pulses while a piezoelectric stage changed the fine delay. The fine delay is used to control the phase shift of the second pulse with respect to the first one. It can be mapped to the relative phase by the relation $\phi = \omega_0 \tau$, where $\hbar\omega_0$ is the laser energy, and has been calibrated by performing wavepacket interferometry at low intensity on the quantum dot, keeping the mechanical stage at a fixed position.

The encoding and decoding consist of the preparation of the two pulses with the same phase. We can imagine that the Oracle controls the fine delay knob, and, by changing the relative phase, determines which one of the four functions is being implemented. Figure 4.4a shows the intensity of the detected photoluminescence

[2]Other mechanisms might further reduce the coherence time.

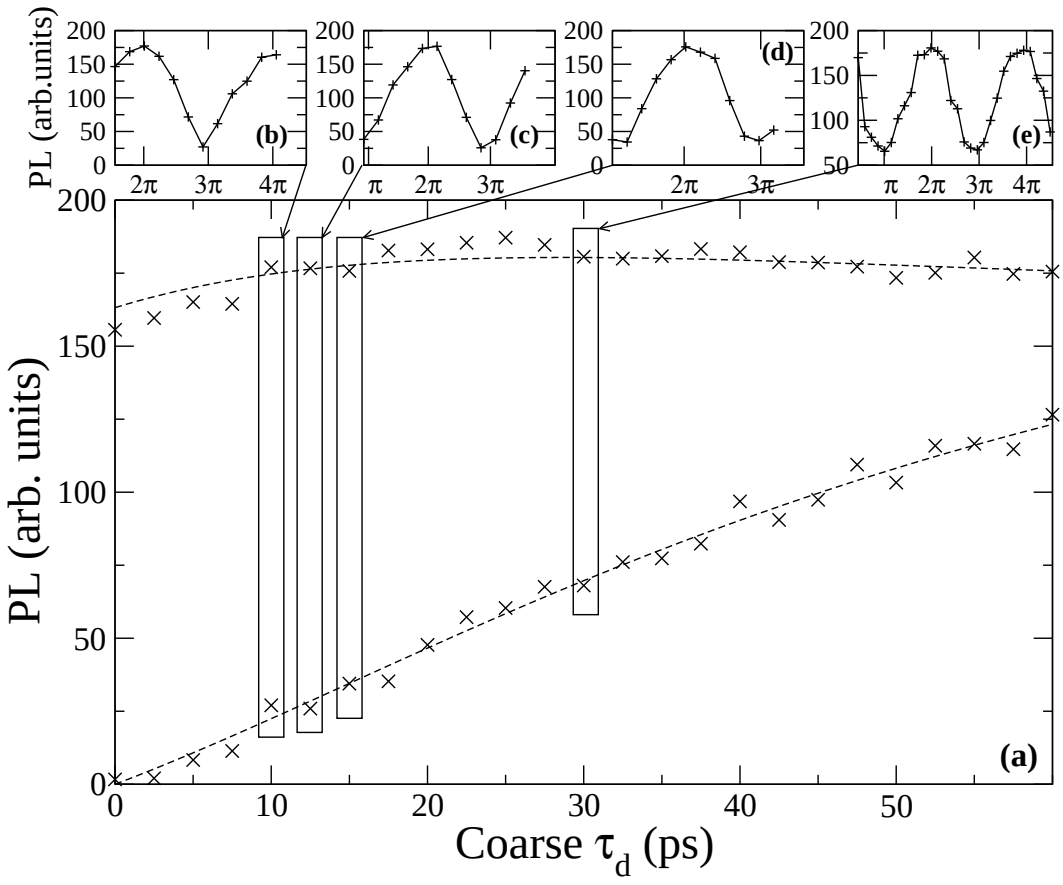

Figure 4.4: Central plot: Envelope of the photoluminescence (PL) as a function of the coarse pulse delay. PL signals as a function of the phase difference between the two pulses are shown in the insets.

as a function of the coarse delay between the two pulses. The lower and upper signals correspond to constructive and destructive interference depending on the relative phase of the two pulses. The contrast between the maxima and minima of the signal decreases as the delay between the pulses approaches the dephasing time of the dot (40 ps), leading to lower fidelities. Figures 4.4b-e describe the detailed behavior of the signal for various values of the phase difference between the two pulses.

We can now interpret this result in terms of the DJ quantum algorithm. As

expected, the maximum population at $|1\rangle$ (that is maximum photoluminescence) occurs for even numbers of π in the relative phase between the two pulses, corresponding to the constant quantum subroutines $\hat{U}_{f_{1,2}}$. On the other hand, minima occur for odd numbers of π in the phase shift between the two pulses, corresponding to the balanced quantum subroutines $\hat{U}_{f_{3,4}}$. The probability of successfully solving the problem is related to the contrast of the maxima and minima in the interference process. We remark that the first three insets in Fig. 4.4 (all with a delay between the pulses between 10 and 20 ps) have a contrast of the order of 75%. This implies a fidelity for the quantum operations comparable to other similar implementations[105]. The fidelity is mainly limited by the dephasing time of the excited state of an exciton in the quantum dot. Making the coarse delay between the pulses as short as possible gives the best fidelity (as can be seen in Fig. 4.4), but this delay must be no shorter than twice the excitation pulse width, so that any optical interference arising out of the overlap of the two pulses is negligible. Also, a detection scheme able to resonantly excite and then measure the exciton ground state such as the side-excitation technique introduced in Ch. 3 would allow for much larger fidelities, due to the increased coherence times.

Experimental phase shift	Operation
$4n\pi$	$\hat{U}_{f_1}$
$\pi + 4n\pi$	$-i\hat{U}_{f_3}$
$2\pi + 4n\pi$	$\hat{U}_{f_2}$
$3\pi + 4n\pi$	$-i\hat{U}_{f_4}$

Table 4.1: Experimental phase shifts and their implemented operations.

By using an interferometric set-up on an excitonic qubit system, we have been able to implement the single-qubit Deutsch-Jozsa algorithm. Although the 1-qubit version of the algorithm does not show all the features of Quantum Computing (in particular entanglement), it is an experimental demonstration of simple quantum computation, including superpositions and interference, in a solid state system.

Chapter 5

Cavity Quantum Electrodynamics

Optical cavities (also called optical resonators) confine the electromagnetic field and modify its density of states. This modified electromagnetic density of states results in changes of the behavior of two-level systems coupled to the field in a cavity. These effects can be small or dramatic, as will be discussed in this chapter.

5.1 Jaynes-Cummings model

The simplest model possible in Cavity Quantum Electrodynamics (CQED) is that of a two-level system coupled to a single mode of the electromagnetic field in a cavity, introduced by Jaynes and Cummings[89, 139]. The Jaynes-Cummings Hamiltonian can be found by taking the fully quantum mechanical Hamiltonian (A.33) and keeping a single mode of the field, resulting in

$$\hat{H}^{\mathrm{JC}} = \frac{\hbar\omega_0}{2}\hat{\sigma_z} + \hbar\omega\hat{a}^\dagger\hat{a} + \hbar g(\hat{\sigma}_+\hat{a} + \hat{\sigma}_-\hat{a}^\dagger), \tag{5.1}$$

where $g = -i\sqrt{\frac{\omega}{\hbar 2\epsilon V}}\vec{d}\cdot\vec{M}(\vec{r}_0)$ is the coupling constant between the two-level system and the cavity. The $\hat{\sigma}_+\hat{a}$ and $\hat{\sigma}_-\hat{a}^\dagger$ operators can be interpreted as the absorption of a cavity photon by the system in the ground state, and the emission of a photon in the cavity by an excited two-level system.

By restricting ourselves to the 1-quanta manifold (with only one excitation in the complete system, composed by the states $\{|0_s1\rangle, |1_s0\rangle\}$) we can further simplify the Hamiltonian by noting that (within this manifold only) $\hat{a}^\dagger\hat{a} = (\hat{I} - \hat{\sigma}_z)/2$:

$$\hat{H}^{\mathrm{JC}} = \frac{\hbar\omega}{2}\hat{I} + \frac{\hbar\Delta\omega}{2}\hat{\sigma_z} + \hbar g(\hat{\sigma}_+\hat{a} + \hat{\sigma}_-\hat{a}^\dagger). \tag{5.2}$$

Then we can diagonalize it exactly[113], resulting in energy eigenvalues

$$E_- = \frac{\hbar\omega}{2} - \frac{\hbar\Omega_0}{2}, \tag{5.3}$$

$$E_+ = \frac{\hbar\omega}{2} + \frac{\hbar\Omega_0}{2}, \tag{5.4}$$

introducing the generalized vacuum Rabi frequency,

$$\Omega_0 = \sqrt{4g^2 + \Delta\omega^2}. \tag{5.5}$$

The corresponding eigenvectors are

$$|-\rangle = \cos\alpha|1_s0\rangle - \sin\alpha|0_s1\rangle, \tag{5.6}$$

$$|+\rangle = \sin\alpha|1_s0\rangle + \cos\alpha|0_s1\rangle, \tag{5.7}$$

where

$$\cos\alpha = \frac{\Omega_0 - \Delta\omega}{\sqrt{(\Omega_0 - \Delta\omega)^2 + 4g^2}} \tag{5.8}$$

$$\sin\alpha = \frac{2g}{\sqrt{(\Omega_0 - \Delta\omega)^2 + 4g^2}}. \tag{5.9}$$

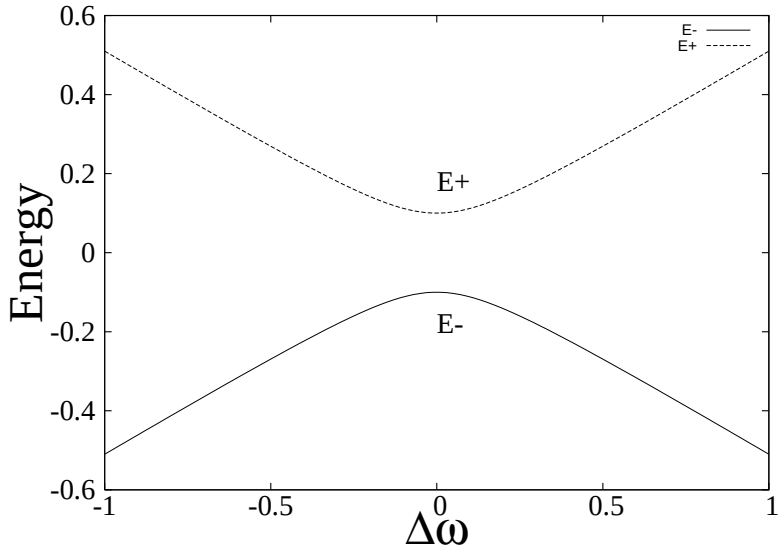

Figure 5.1: Energy structure of the dressed two-level system.

The states (5.7) are sometimes referred as "dressed states", because the interaction with the field "dresses" the bare atom-field states of the non-interacting system. The energies for both the bare and dressed states are shown in Fig. 5.1, where we can see that when the interaction is present, there is a splitting (equal to the vacuum Rabi splitting Ω_0) of the energy levels as compared to the bare case.

5.1.1 Lossy Jaynes-Cumming model

As written, Hamiltonian 5.1 does not include any losses or dephasing. It is possible to take those into account using a master equation formalism[7]. Now, the energy levels (both cavity and two-level system) are broadened by the losses, and the behavior of the full system will depend on how big the losses are with respect to the coupling. There are two well-defined regimes: weak coupling and strong coupling.

Weak coupling

When the coupling is weak compared to the losses ($g << |\Delta\omega_c - \Delta\omega_a/4$, where $\Delta\omega_c$ and $\Delta\omega_a$ are the full witdh half-maximum (FWHM) linewidth of the cavity and two-level system states), the qualitative behavior is similar to the uncoupled case, with a crossing of the energy levels at resonance. The effect of the interaction is to modify the linewidth of the two-level system state, effectively modifying its decay rate. This phenomenon is well known as the Purcell effect[133]. Under the weak coupling assumptions, the modified spontaneous emission rate can be written in terms of the original emission rate as[62, 63]

$$F_p = \frac{\tau_{\text{free}}}{\tau_{\text{cav}}} = \frac{3Q(\lambda/n)^3}{4\pi^2 V} \frac{\Delta\omega_c^2}{4(\omega_0 - \omega)^2 + \Delta\omega_c^2} \frac{|\vec{d} \cdot \vec{M}(\vec{r}_0)|^2}{|\vec{d}|^2} \tag{5.10}$$

Strong coupling

If the coupling is strong enough to overcome the broadening of the lines so the splitting can be resolved and $g > |\Delta\omega_a - \Delta\omega_c|/4$, the behavior now resembles that of the ideal Jaynes-Cummings Hamiltonian, showing a clear Vacuum Rabi splitting at resonance.

5.2 Physical implementations

There are many different physical systems which can be approximated by the model explained above, and that have shown experimentally both the weak and strong coupling regimes. A very good review of the best ones working within the optical range of wavelengths is given in [156]. We can broadly categorize the systems by the "two-level system" they use.

5.2.1 Single atoms

The first successful attempts at studying CQED at optical frequencies were done with atomic beams and trapped atoms. The first successful cavities were Fabry-Perot cavities, where both the Purcell modification of the emission from single atoms[77] and Vacuum Rabi Splitting[152] were observed. More recently, strong coupling using a monolithic toroidal microcavity has also been demonstrated[8].

5.2.2 Single quantum dots

Quantum dots have a distinct advantage with respect to atoms for CQED, which is the fact that they are stationary with respect to the cavity so the quantum dot will be coupled to the cavity at all times. Besides, in many implementations the quantum dot and the cavity are a monolithic system. These properties enable us to speculate on optoelectronic CQED devices such as single-photon sources for quantum cryptography and quantum information processing[172], "thresholdless" lasers[132] and even more speculative quantum information CQED devices as interfaces between stationary quantum dot qubits and flying photon qubits[173].

The most favored microcavities are photonic crystal cavities and micropillars, but other designs such as microspheres, microdisks and all-epitaxial microcavities have also been used to explore CQED phenomena. Ref. [63] has a very detailed introduction to the topic of CQED in quantum dots.

Micropillars

Micropillar cavities are fabricated by growing two semiconductor DBR mirrors beneath and above the quantum dots to provide optical confinement in the growth direction. An etching process then defines pillar structures, which provide lateral confinement[64]. A further improvement is the use of an oxide aperture for the lateral confinement, that increases the Q factor of the cavity and reduces its mode

volume[147]. Micropillar cavities have Q factors between 1000-150000 and mode volumes on the order of a few cubic wavelengths. Many CQED effects have been demonstrated in micropillars, including the Purcell effect[65, 138], strong coupling[134] and single photon emission from a strongly coupled quantum dot cavity system[131].

Photonic crystal cavities

Photonic crystal cavities exploit in-plane Bragg reflections to provide in-plane confinement. After the sample growth, a periodic array of holes containing a carefully designed defect[3] is etched on the sample. Removal of a sacrificial layer of material grown below the quantum dot matrix leaves a thin slab which provides optical confinement in the growth direction by total internal reflection[91]. Photonic crystal cavities in III-V materials have moderately high Q factoris between 500-50000 (Silicon based cavities can achieve much larger Q factors[11]), and very small mode volumes, even smaller than 1 cubic wavelength. Many CQED effects have also been observed in these cavities, such as the Purcell effect[14, 51], few-emitter lasing[148] and strong coupling[174, 78]. An interesting advancement is the ability to deterministically couple quantum dots with the cavity, as demonstrated in Ref. [14].

All-epitaxial microcavities

A new type of microcavity, designed by the Deppe group, is grown completely by an epitaxial method[118]. The growth direction confinement is provided by a pair of DBR reflectors, while the in-plane confinement is obtained by placing the quantum dots in raised mesas. These cavities possess excellent mechanical and thermal properties due to their fully monolithic construction, and they are well suited for electrical injection. Purcell enhancement and inhibition of spontaneous emission have been demonstrated in this system[117].

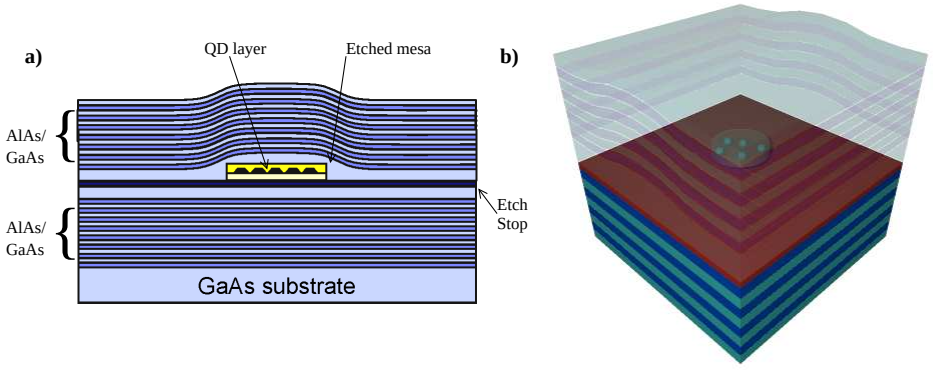

Figure 5.2: **a)** Schematic of an all-epitaxial cavity[118], courtesy of A. Muller. **b)** 3D schematic of the same cavity.

Whispering Gallery Mode cavities

In Whispering Gallery Mode (WGM) cavities, the optical confinement comes from total internal reflection on the cavity boundaries. There are several variations, such as disks, toroids and spheres. Microdisks are the simplest to fabricate with embedded quantum dots by sample post-processing[142]. Both the Purcell effect[61, 53] and strong coupling have been shown in microdisk cavities[128]. Microtoroids and microspheres are simple to fabricate (see chapter 6 for a more detailed description of the microsphere fabrication) in silica using reflow techniques, but they don't have any obvious way to embed quantum dots in them. Nevertheless, strong coupling between a microsphere and nitrogen vacancies in diamond nanocrystals deposited on its surface has been experimentally demonstrated[126].

Chapter 6

Microsphere resonators

Microsphere resonators have some fundamental and technical characteristics that make them attractive. On the fundamental side, they have very low losses and correspondingly large photon lifetimes. On the technical side, they are simple and inexpensive to manufacture. This chapter will discuss the theory describing resonant modes of a sphere, fabrication of silica (amorphous silicon dioxide, SiO_2) microspheres and measurement techniques.

6.1 Theory for Whispering Gallery Modes in a sphere

6.1.1 Mie theory of a spherical resonator

The Whispering Gallery Modes (WGMs) of dielectric spheres are resonant modes of the electromagnetic field whose characteristics (fields distribution, frequency) depend on the sphere morphology (radius, index of refraction of the material) and are also known as Morphology Dependent Resonances (MDR). The forthcoming discussion will follow chapter 4 of Bohren and Huffman[31], using a mostly formal approach. It is also worthwhile to mention (for interested readers) the approach by Johnson[90] that connects the problem of MDRs with quasi-bound quantum

mechanical states and can provide further insights into the resonances.

The field equations

We start by assuming we have harmonic fields,

$$\vec{E} = \vec{E}_0 e^{i(\vec{k}\cdot\vec{x}-\omega t)}, \quad \vec{H} = \vec{H}_0 e^{i(\vec{k}\cdot\vec{x}-\omega t)}. \tag{6.1}$$

In a linear, isotropic and homogeneous dielectric medium with dielectric constant ε and magnetic permittivity μ, these fields have to satisfy the Maxwell equations

$$\nabla\cdot\vec{E} = 0, \qquad \nabla\cdot\vec{H} = 0; \tag{6.2}$$

$$\nabla\times\vec{E} = i\omega\mu\vec{H}, \quad \nabla\times\vec{H} = -i\omega\varepsilon\vec{E}. \tag{6.3}$$

Taking the curl of the curl equations (6.3) and using a vector identity we conclude that both fields satisfy the vector Helmholtz equation,

$$\nabla^2\vec{E} + k^2\vec{E} = 0, \quad \nabla^2\vec{H} + k^2\vec{H} = 0, \tag{6.4}$$

where $k^2 = \omega^2\varepsilon\mu$.

Fundamental solutions

In order to find solutions of the Helmholtz vector equation, it is most convenient to reduce it to a scalar equation. We can achieve that by introducing a scalar function ψ and a constant vector $\vec{c}$ and using them to define the divergenceless vector functions

$$M = \nabla\times\vec{c}\psi, \quad N = \frac{\nabla\times\vec{M}}{k}, \tag{6.5}$$

such that $-\nabla\times\vec{N} = k\vec{M}$.

We can use vector identities to prove that $\vec{M}$ and $\vec{N}$ will satisfy the vector

Helmholtz equation if ψ is a solution to the scalar Helmholtz equation

$$\nabla^2\psi + k^2\psi = 0. \tag{6.6}$$

In a problem with spherical symmetry, we can make $\vec{M}$ a solution to the vector Helmholtz equation in spherical coordinates by choosing ψ to be a solution to the scalar Helmholtz equation in spherical coordinates and $\vec{c} = \vec{r}$. Then $\vec{M}$ and $\vec{N}$ will be the fundamental solutions with spherical symmetry for the Maxwell equations. Due to its construction, $\vec{M}$ won't have a radial component ($\vec{M} \cdot \hat{r} = 0$).

In spherical coordinates, the scalar Helmholtz equation becomes

$$\frac{1}{r^2}\frac{\partial}{\partial r}\left(r^2\frac{\partial\psi}{\partial r}\right) + \frac{1}{r^2\sin\theta}\frac{\partial}{\partial\theta}\left(\sin\theta\frac{\partial\psi}{\partial\theta}\right) + \frac{1}{r^2\sin\theta}\frac{\partial^2\psi}{\partial\phi^2} + k^2\psi = 0. \tag{6.7}$$

We use separation of variables to write a solution of the form $\psi(r,\theta,\phi) = R(r)\Theta(\theta)\Phi(\phi)$, leading to the three separated equations

$$\frac{d^2\Phi}{d\phi^2} + m^2\Phi = 0, \tag{6.8}$$

$$\frac{1}{\sin\theta}\frac{d}{d\theta}\left(\sin\theta\frac{d\Theta}{d\theta}\right) + \left[l(l+1) - \frac{m^2}{\sin\theta}\right]\Theta = 0, \tag{6.9}$$

$$\frac{d}{dr}\left(r^2\frac{dR}{dr}\right) + \left[k^2r^2 - l(l+1)\right]R = 0, \tag{6.10}$$

where m and l are separation constants.

Equation (6.8) has two linearly independent solutions (one odd, one even):

$$\Phi_e = \cos(m\phi), \quad \Phi_o = \sin(m\phi). \tag{6.11}$$

The condition that ψ must be a single valued function of the azimuthal angle ψ requires that m be an integer. We can generate all possible linearly independent solutions by restricting m to be equal to or greater than 0.

The solutions to equation (6.9) are the associated Legendre polynomials $P_l^m(\cos\theta)$[2] of degree l and order m.

Finally, equation (6.10) is the spherical Bessel differential equation. Consequently, its solutions are going to be the spherical Bessel functions

$$j_l(kr) = \sqrt{\frac{\pi}{2kr}} J_{l+\frac{1}{2}}(kr), \quad y_l(kr) = \sqrt{\frac{\pi}{2kr}} Y_{l+\frac{1}{2}}(kr). \tag{6.12}$$

It will be useful to introduce two linear combinations of the spherical Bessel functions, namely the spherical Hankel functions

$$h_l^{(1)}(kr) = j_l(kr) + iy_l(kr), \quad h_l^{(2)}(kr) = j_l(kr) - iy_l(kr), \tag{6.13}$$

which are also solutions of Eq. (6.10).

Now, we can write the even and odd expressions for ψ:

$$\psi_{elm} = Y_{el}^m(\theta,\phi) z_l(kr), \tag{6.14}$$

$$\psi_{olm} = Y_{ol}^m(\theta,\phi)(\cos\theta) z_l(kr), \tag{6.15}$$

where $Y_{el}^m(\theta,\phi) = \cos(m\phi)P_l^m(\cos\theta)$ and $Y_{ol}^m(\theta,\phi) = \sin(m\phi)P_l^m(\cos\theta)$ are spherical harmonics[1] and z_n is any of the four spherical functions j_l, y_l, $h_l^{(1)}$ or $h_l^{(2)}$ we have introduced.

The vector solutions are then

$$\vec{M}_{\{e,o\}lm} = \nabla \times (\vec{r}\psi_{\{e,o\}lm}), \tag{6.16}$$

$$\vec{N}_{\{e,o\}lm} = \frac{\nabla \times \vec{M}_{\{e,o\}lm}}{k}. \tag{6.17}$$

[1]The usually defined spherical harmonics Y_l^m (see Jackson[88], p. 108 for instance) satisfy $Y_l^m = Y_{ol}^m + iY_{el}^m$.

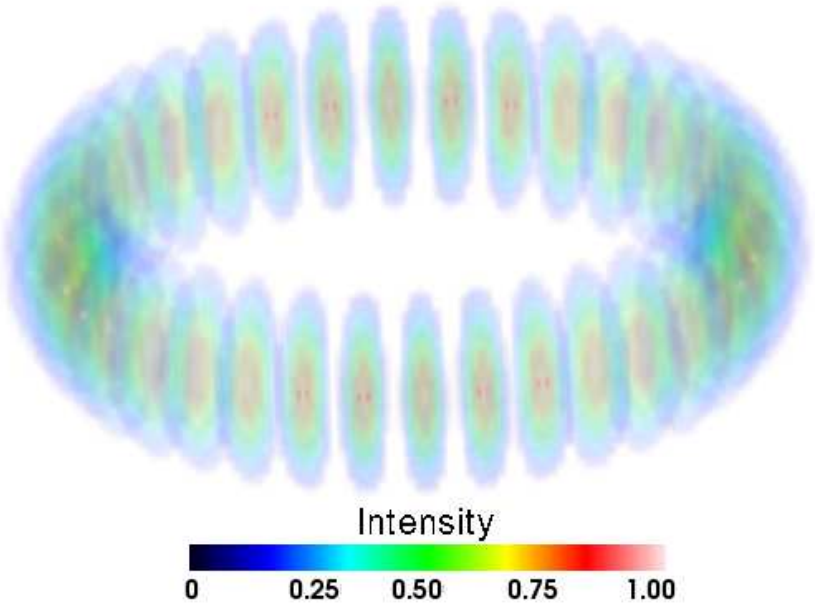

Figure 6.1: Field intensity distribution for a mode with $l = 18$, $m = 18$ and radial number $p = 1$.

The explicit expression of these solutions is

$$\begin{aligned}
\vec{M}_{\{e,o\}lm} &= \frac{-m}{\sin\theta}\left\{\sin(m\phi),\cos(m\phi)\right\} P_l^m(\cos\theta) z_l(kr)\hat{\theta} \\
&\quad - \left\{\cos(m\theta),\sin(m\theta)\right\} \frac{dP_l^m(\cos\theta)}{d\theta} z_l(kr)\hat{\phi}, \qquad (6.18) \\
\vec{N}_{\{e,o\}lm} &= \frac{z_n(kr)}{kr}\left\{\cos(m\phi),\sin m\phi\right\} l(l+1) P_l^m(\cos\theta)\hat{r} \\
&\quad + \left\{\cos(m\phi),\sin(m\phi)\right\} \frac{dP_l^m(\cos\theta)}{d\theta}\frac{1}{kr}\frac{d}{d(kr)}\left[krz_l(kr)\right]\hat{\theta} \\
&\quad - m\left\{\sin(m\phi),\cos(m\phi)\right\} \frac{P_l^m(\cos\theta)}{\sin\theta}\frac{d}{d(kr)}\left[krz_l(kr)\right]\hat{\phi}. \qquad (6.19)
\end{aligned}$$

When $l \approx m$, the angular distribution will be peaked around the equator of the sphere. Those modes, closely confined to the sphere equation, are the WGMs we are interested in, as can be seen in Fig. 6.1.

Boundary conditions

Up to now we have the fundamental solutions for the fields in a spherical symmetry. In order to find the particular fields and their frequencies, we need to take into account the boundary conditions. This is where we need the particular geometry of the resonator. In our case, we will consider a sphere of radius a, dielectric constant ε_s and magnetic permittivity μ_s (index of refraction $n_s = (\varepsilon_s \mu_s)^{-1/2}$) , surrounded by an infinite medium with refraction index $n_o = (\varepsilon_o \mu_o)^{-1/2}$. Thus we will have different fields inside $(\vec{M}^I, \vec{N}^I)$and outside $(\vec{M}^O, \vec{N}^O)$.

Radial boundary conditions will define which spherical functions to use. The inside fields will be finite if we choose their radial dependence be the spherical Bessel function,

$$\{\vec{E}^I, \vec{H}^I\} \propto j_l(kr). \tag{6.20}$$

For the outside fields, we choose the radial dependence to be a spherical Hankel function because it corresponds asymptotically to an outgoing spherical wave (see Bohren[31], p. 94). Adding an r-independent factor to take into account the discontinuity in the media, we have

$$\{\vec{E}^O, \vec{H}^O\} \propto B(k) h_l^{(1)}(kr). \tag{6.21}$$

The other boundary condition to satisfy is that the tangential components of the $\vec{E}$ and $\vec{H}$ fields must be continuous at the sphere surface where the refraction index is discontinuous,

$$\vec{E}^O(a, \theta, \phi) \times \hat{r} = \vec{E}^I(a, \theta, \phi) \times \hat{r}, \tag{6.22}$$

$$\vec{H}^O(a, \theta, \phi) \times \hat{r} = \vec{H}^I(a, \theta, \phi) \times \hat{r}. \tag{6.23}$$

In order to continue the analysis, we have to consider the TE and TM cases sepa-

rately.

Boundary conditions: TE case

In the TE (transverse electric) case, the electric field has no radial component, so we can write

$$\vec{E}(r,\theta,\phi) = E_0\vec{M}(r,\theta,\phi). \tag{6.24}$$

From the Maxwell Equations (6.3) and the relationship between $\vec{M}$ and $\vec{N}$ in Eq. (6.5) we can then find that

$$\vec{H}(r,\theta\phi) = -iE_0\sqrt{\frac{\varepsilon}{\mu}}\vec{N}(r,\theta\phi). \tag{6.25}$$

The electric field boundary conditions (6.22) together with the explicit expression of $\vec{M}$, Eq. (6.18), result directly in the condition

$$B(k)h_l^{(1)}(k_o a) = j_l(k_s a), \tag{6.26}$$

where $k_o = 2\pi\lambda/n_o$ and $k_s = 2\pi\lambda/n_s$ are the wavenumbers outside and inside the sphere respectively.

The magnetic field boundary conditions (6.23) are slightly more involved. We can start with

$$B(k)\sqrt{\frac{\varepsilon_o}{\mu_o}}\vec{N}^O(a,\theta,\phi) = \sqrt{\frac{\epsilon_s}{\mu_s}}\vec{N}^I(a,\theta,\phi), \tag{6.27}$$

$$B(k)\vec{N}^O(a,\theta,\phi) = \frac{\mu_o n_o}{\mu_s n_s}\vec{N}^I(a,\theta,\phi). \tag{6.28}$$

Using the explicit component expression of $\vec{N}$ and Eq. (6.26) we then obtain

$$\frac{j_l(k_s a)}{k_o a}\frac{d}{d(k_o a)}\left[k_o a h_l^{(1)}(k_o a)\right] = \frac{\mu_o b}{\mu_s}\frac{h_l^{(1)}(k_o a)}{k_s a}\frac{d}{d(k_s a)}\left[k_s a j_l(k_s a)\right], \tag{6.29}$$

where $b = n_s/n_o$ as a shorthand.

We can clarify the expression by defining $x = k_o a$ so that $k_s = bk_o$ and $d/d(k_s a) = d/d(bx)$:

$$\frac{1}{h_l^{(1)}(x)} \frac{d}{dx} \left[x h_l^{(1)}(x) \right] = \frac{\mu_o}{\mu_s j_l(mx)} \frac{d}{d(bx)} \left[bx j_l(bx) \right]. \tag{6.30}$$

Boundary conditions: TM case

In the TM (transverse magnetic) case, it is now the magnetic field that has no radial component, thus

$$\vec{H}(r, \theta, \phi) = H_0 \vec{M}(r, \theta, \phi). \tag{6.31}$$

In a manner analogous to the TE case, the electric field will be

$$\vec{E}(r, \theta\phi) = i H_0 \sqrt{\frac{\mu}{\varepsilon}} \vec{N}(r, \theta\phi). \tag{6.32}$$

The magnetic field boundary conditions (6.23) will now give us the same result as Eq. (6.26), while the electric field boundary conditions (6.22) will give us the condition

$$\frac{1}{h_l^{(1)}(x)} \frac{d}{dx} \left[x h_l^{(1)}(x) \right] = \frac{\mu_s}{\mu_o b^2 j_l(bx)} \frac{d}{d(bx)} \left[bx j_l(bx) \right]. \tag{6.33}$$

Given the radius of the sphere and the refractive indices of both the sphere and the surrounding medium, Eqs. (6.30) and (6.33) can be solved numerically (or asymptotically approximated[104, 136]) to find out the resonant wavelengths of modes with a given value of l. There are many solutions to these equations, which differ in the number of nodes of the field in the radial direction. The order of the solution gives rise to another number, p, the radial mode number (a mode with radial number p will have $p - 1$ radial nodes inside the sphere, see Fig. 6.2). The higher the p number is, the peak intensity will be further away from the sphere

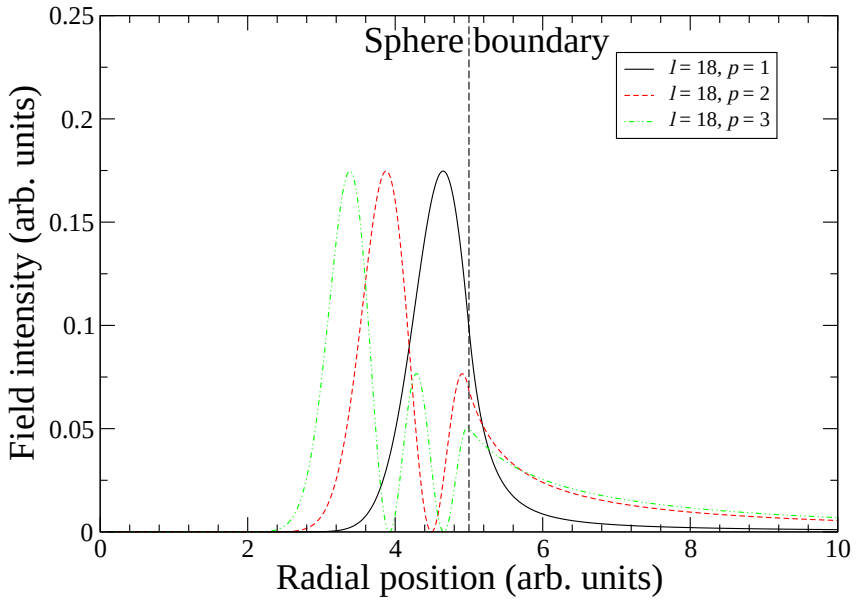

Figure 6.2: Radial intensity profiles for three mode functions with $l = 18$ and $p = 1, 2, 3$.

surface and the decay outside the surface will be softer. Together with the already shown mode functions, $\vec{M}_{\{e,o\}lm}$ and $\vec{N}_{\{e,o\}lm}$, the calculated value x_{lp} provides a complete characterization of the mode.

Broken spherical symmetry

Astute readers probably noticed that the resonance conditions (6.30) and (6.33) don't involve the m index of the mode. This is because modes differing only in m are degenerate when there is spherical symmetry. If the sphere is not perfect but rather has a slight eccentricity ϵ in its equatorial cross-section, the modes with same l and different m values will split, the splitting being approximately[66]

$$\frac{\Delta\omega}{\omega} = \pm\frac{\epsilon^2(l^2 - m^2)}{4l^2} \approx \pm\left.\frac{\epsilon^2(l - m)}{2l}\right|_{l\approx m} \tag{6.34}$$

6.1.2 Lossy resonators

A dielectric sphere is an open resonator, with its modes mostly confined inside the sphere, but with an extending evanescent tail. This tail allows for radiative tunneling of the confined light to the outside medium, limiting the amount of time radiation can be confined in an ideal sphere. Besides this radiation limitation, material limitations such as absorption, surface roughness and adsorption of impurities can also affect the decay time of the modes.

A very convenient way to quantify the losses of a resonator is by means of the quality factor, also referred to as Q factor. The Q factor is defined as the energy loss per unit energy in the resonator, and is inversely related to the linewidth,

$$Q = \frac{\Delta E}{E} = \frac{\Delta \omega}{\omega} = \frac{\Delta \nu}{\nu}. \tag{6.35}$$

The Q factor is also inversely related to the decay time of the mode in the cavity, $Q = \tau_c \omega$.

All the present loss mechanisms determine the Q factor of a given sphere. In a very general way, we can relate the total Q factor to the Q factors that would result if only a given mechanism were present[67]:

$$\frac{1}{Q} = \sum_i \frac{1}{Q_i}. \tag{6.36}$$

Depending on the sphere size and conditions, different mechanisms will dominate the losses. For very small diameters, the leading term is given by radiation losses. For spheres with diameters larger than 15 wavelengths, radiation loses become small and other mechanisms become more important, such as material absorption[67], Rayleigh scattering due to internal or surface inhomogeneities[68], absorption due to adsorbed water[160], or just scattering/absorption due to adsorbed macroscopic impurities.

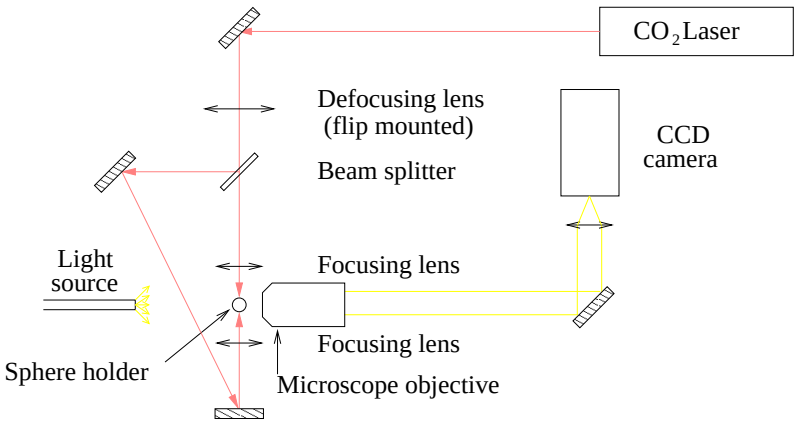

Figure 6.3: Schematic of the sphere making setup.

A different kind of loss is that intrinsic to the coupling. Since the coupling to a resonator has to be symmetric in time, the ability to couple light into it is inseparable from the ability of extracting light out of it (at least for single-mode coupling). This means that increasing the coupling will increase the total resonator losses, lowering the Q factor. This phenomenon is usually known as "resonator loading", and the Q factor of a cavity can be decomposed into an intrinsic Q and a loaded Q factor, $Q^{-1} = Q_{\text{int}}^{-1} + Q_{\text{load}}^{-1}$.

6.2 Fabrication

The fabrication of silica microspheres is a relatively simple process which does not require a very big infrastructure. It was introduced by Braginsky and Ilchenko in 1989[36] and adopted by many groups since then[70, 162, 38, 97]. The main sequence involves stretching an optical fiber, to reduce its diameter, and then melt the small diameter tip. Surface tension will ensure an almost spherical shape, while the reflow of the melted material will result in a smooth surface and high Q factors.

In our setup, we melted the fiber using a Synrad 48-1 10W CO_2 laser, emitting at a wavelength of 10.6 μm. All our spheres are made of regular single-mode

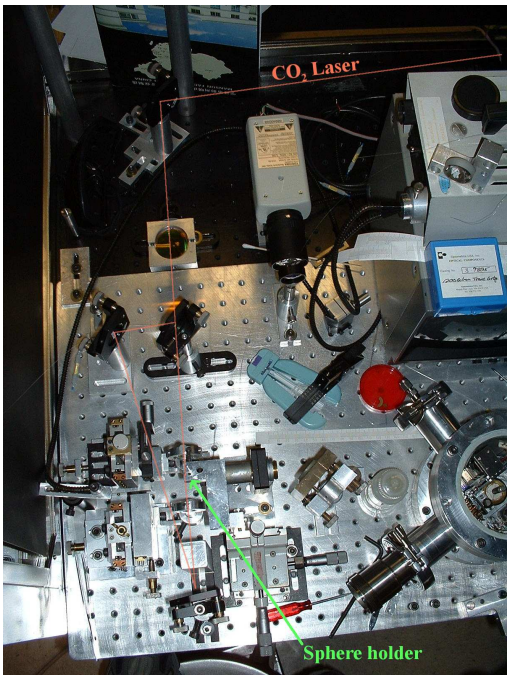

Figure 6.4: Overview of the sphere making station.

optical fiber, Nufern SM800 (bought at F-SF from Newport Corporation). At all times, the fabrication is monitored using a microscope objective and a CCD camera (as can be seen in the schematic in Fig. 6.3 and the photograph in 6.4).

Making a small diameter fiber tip

We could, in principle, just melt the tip of a fiber and make it round. However, since the diameter of an optical fiber is 125 μm, the sphere diameter would not be any smaller. Since we want to work with smaller spheres, we need to slim down the diameter of the fiber tip. We achieve that by fixing a weight at the tip with adhesive tape (the weight is a small piece of a brass washer in our case, but its nature is not really all that important) and then slowly turn up the laser until the silica starts melting and flows downward. There are some important details that should be taken into account:

- The fiber protective jacket has to be stripped first. If this is not done, the jacket will be burned by the laser and might result in a dirtier sphere.
- It is always a good idea to clean the bare fiber with isopropyl alcohol and a lint-free wipe.
- The laser power has to be ramped up slowly, as too much power will immediately break the fiber without stretching it. If this happens, the process has to be restarted.
- The laser must not be too tightly focused on the fiber, or the fiber will break not matter how slowly the power is ramped up.

Once the fiber has been stretched to the desired diameter (which will change depending on the desired sphere diameter and mechanical properties), a short, intense burst of the laser will easily break the fiber, leaving a clean tip on the top part, as show in Fig 6.5.

Making the sphere

Once the a clean tip with a proper diameter is available, another short burst of the laser should be enough to melt it and form the sphere, a shown in Fig. 6.6. When making small spheres, it is best to focus the laser tightly as it will make the process faster and improve the sphere symmetry.

Advanced techniques

At times it is desirable to fabricate a large sphere with a thin stem. The technique described above won't allow that, as the diameter of the sphere will be dictated mostly by the diameter of the stem. It is possible to work around this by not making a fiber tip, but rather leaving a lump of fiber after the stretched section. As

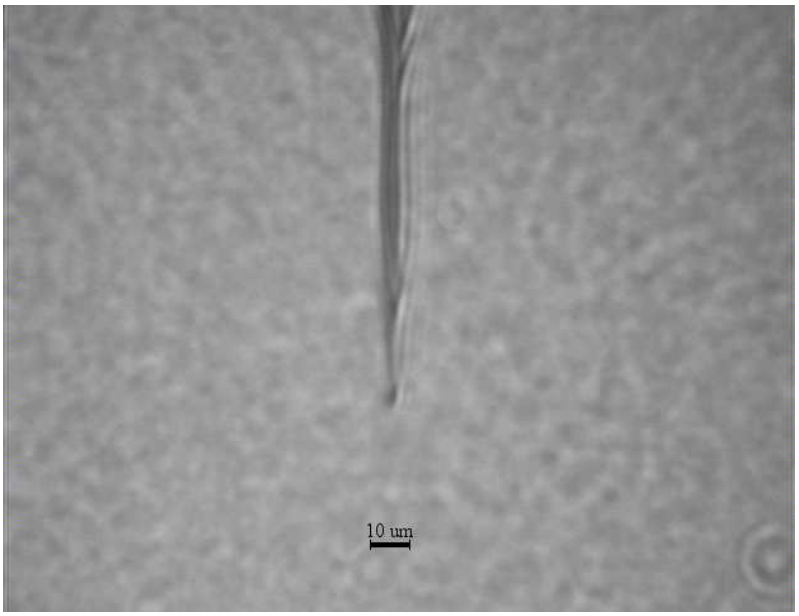

Figure 6.5: Fiber tip right after breaking the fiber.

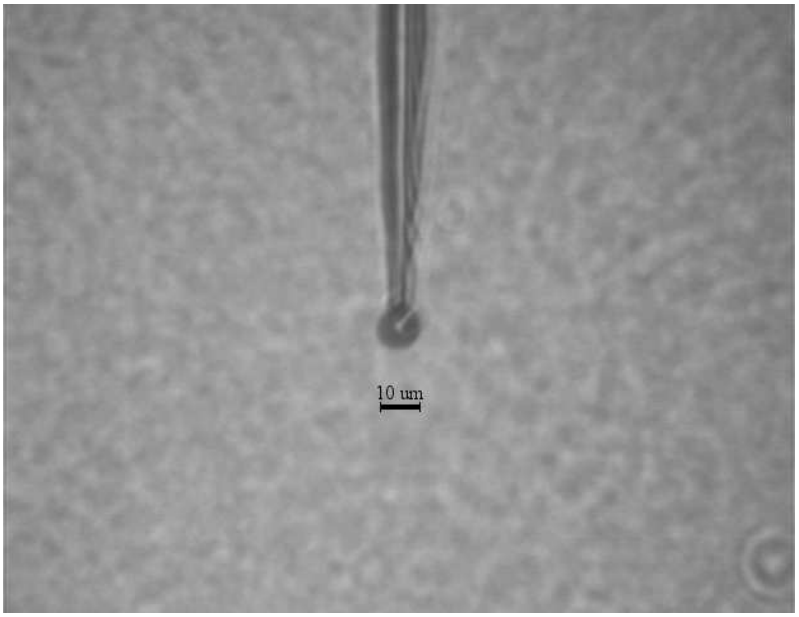

Figure 6.6: Sphere made from the fiber tip in Fig. 6.5.

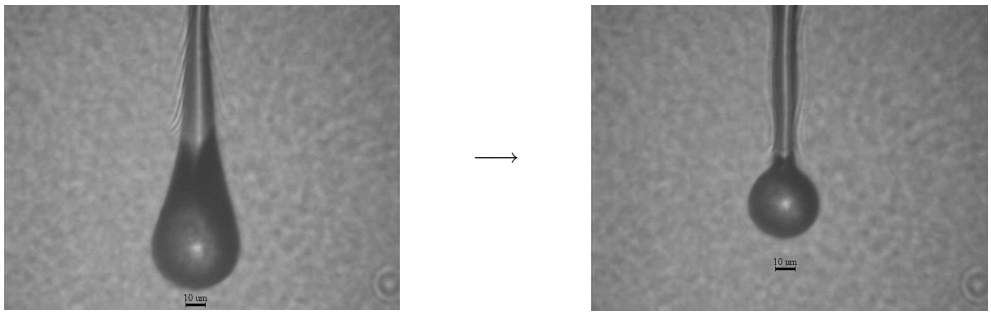

Figure 6.7: Modified technique to make large spheres on a thin stem.

Fig. 6.7 shows, this allow making spheres much larger than their stems (this will result in a much more fragile stem, though).

It is also possible to bend the fiber stem, obtaining geometries as the one depicted in Fig. 6.8. The process is simple: Once the sphere is formed, the laser has to be focused (but not tightly) on the section of the stem to be bent and then ramped up slowly until the fiber begins to bend. The fiber will bend towards the direction of the incoming laser beam, and the laser has to be turned off when the desired angle has been reached.

6.3 Coupling light into/out of a spherical resonator

The low losses (high Q factors) of spherical resonators imply that their coupling to the outside is weak. At first sight, this seems to suggest that coupling light into the resonator will be difficult but this turns out not to be the case using the proper coupling technique.

For simple characterization, coupling light into the resonator might be enough, but for applications it is desirable to be able to extract light efficiently too. We can define an "ideality" of the coupling as the ratio between the light coupled in and the light coupled out[38]. Since electromagnetic phenomena are time-reversible, we would expect that any scheme able to couple light into the resonator would be able

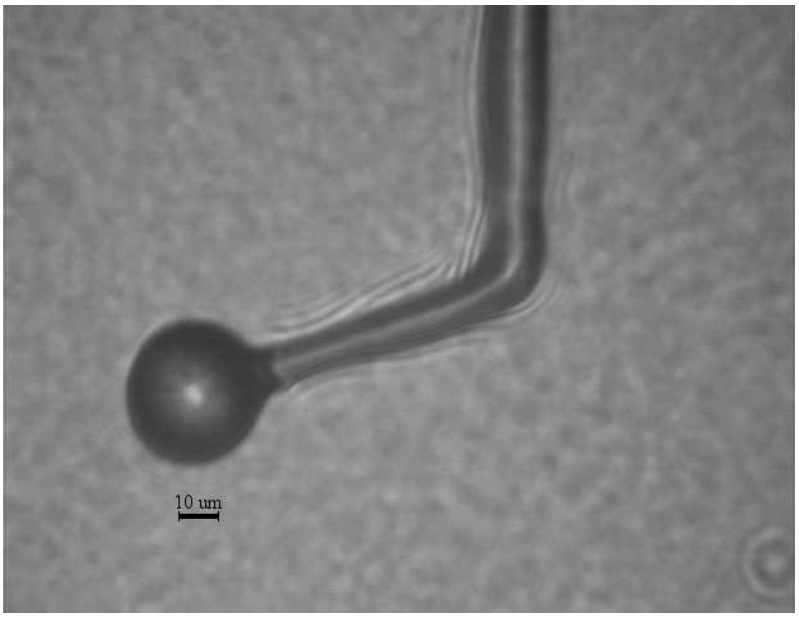

Figure 6.8: Sphere on a bent stem.

to couple light out of it and thus have an ideality equal to 1. However, real couplers usually present some asymmetry that results in lower (sometimes much lower) idealities.

6.3.1 Free space coupling

At first, it seems that since microspheres are open resonators it would be possible to couple light into a WGM by just focusing a gaussian beam near the sphere equator. This turns out to have a negligible efficiency, because for spheres that are larger than a few wavelengths in diameter the radiation losses are incredibly small. A concise discussion of this can be found in Ref. [112]. By deforming the spheres in a controlled fashion it becomes possible to improve the free space coupling due to chaos-assisted tunneling in asymmetrical resonators[124, 102]. This technique has been used to explore the strong coupling of microspheres to nitrogen vacancies in diamond nanocrystals[126].

6.3.2 Evanescent coupling

While free space coupling is quite inefficient, it is possible to couple more efficiently to the WGMs in the sphere by means of evanescent coupling. This involves overlapping of the evanescent field of the sphere mode and the evanescent field of a coupler.

Prism couplers

One possible evanescent coupler to use is a prism[154]. Fig. 6.9 describes the geometry. A laser beam is focused into a prism (made of a material with higher refractive index than the resonator) at an angle such that it undergoes total internal reflection. The evanescent field at the prism surface can then couple into the resonator as it is brought closer. The dimension of the gap between the prism and the sphere determines the field overlap and the amount of light coupled. Prism couplers can be effective (injecting into the resonator about 80% of the incident radiation[69]). On the other hand, it is difficult to achieve high ideality with prisms because they are multi-mode couplers[112] (the beam focused on the prism is actually composed of many different modes which couple differently to the WGM). Prism couplers are the best choice when the refractive index of the resonator is high[85], as it is possible to manufacture prisms from high-index materials. There are variations on this type of coupler, such as the angle-polished fiber coupler[86], which combines the advantages of prism couplers those of fiber couplers.

Tapered fiber couplers

Tapered fiber couplers are just waveguide couplers appropriate for the geometry of the resonator. In a regular single-mode optical fiber there is a micron-scale core surrounded by a glass cladding with a slightly lower refractive index. By tapering the fiber to a sub-micron diameter, it is possible to adiabatically transfer the light from

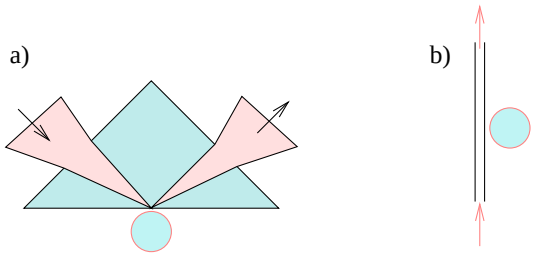

Figure 6.9: Evanescent couplers. a) Prism coupler. b) Fiber coupler.

the fiber fundamental mode into the fundamental mode of the now air-clad stretched fiber. The evanescent field from the stretched section is very strong (due to the fact that its diameter is close to the wavelength of the light) and can overlap significantly with the evanescent field from the WGM. Judicious selection of the taper diameter allows for good phase matching between the waveguide and the resonator[97] and very effective coupling (coupling efficiencies of 99.99% have been reported[141]). The high efficiency of tapered fiber couplers has made them a popular choice to couple to WGM resonators[70, 38, 121, 99].

6.4 Fabrication of tapered fiber couplers

The essence of all fiber tapering techniques is to soften the section of fiber to be tapered while it is mechanically pulled[29]. Conservation of mass will cause the diameter of the fiber to gradually decrease. Diversity appears in the mechanism to soften the fiber: it is most commonly a butane or oxy-hydrogen flame scanned across the fiber section, but it can also be a CO_2 laser[48, 166] or even a ceramic microfurnace[150].

Our fiber stretching setup (which can be seen in Fig. 6.10, together with a schematic in Fig. 6.11) consists of a Mansun MS-2008 water torch, a mechanical stage with two stepper motors to pull the fiber, and another one to hold the torch tip with two stepper motors: one to control the distance between the fiber and the flame

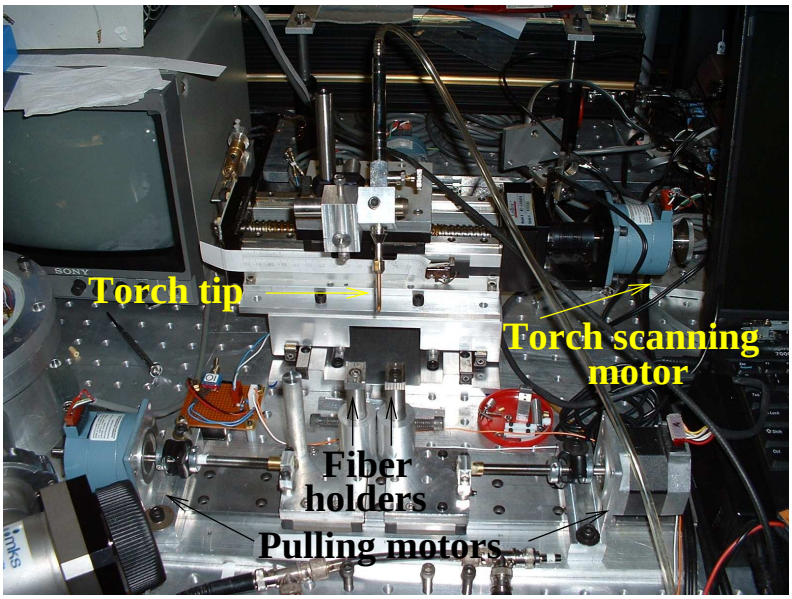

Figure 6.10: Fiber pulling setup.

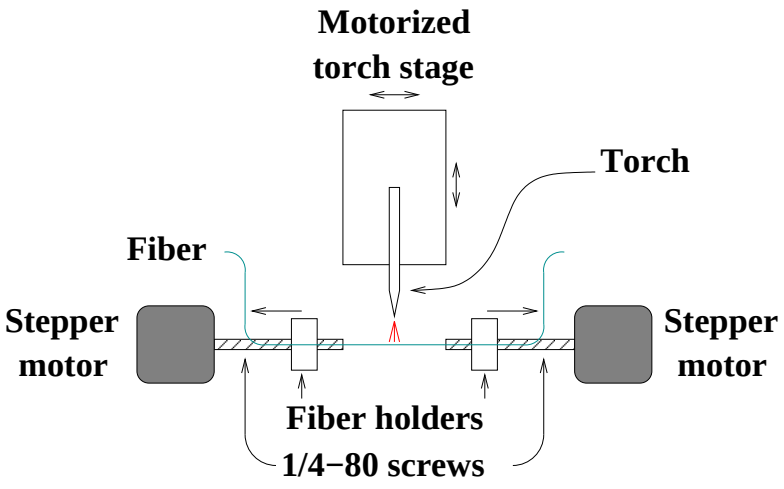

Figure 6.11: Schematic of the fiber pulling setup in Fig. 6.10.

and other to scan the flame along a section of the fiber. A laptop computer running a custom program controls the process, which is monitored by looking at the real time transmission of a laser beam coupled into the fiber. When the stretched region becomes a single mode waveguide, the absence of modal interference will eliminate fluctuations in the transmitted signal, signaling the end of the process. A typical tapering process runs the following sequence:

1. Strip and clean the section of fiber to be tapered (our standard length is close to 15 mm).

2. Hold the fiber in the stage using magnetic clamps, making sure it is straight.

3. Set the software parameters (see table 6.1 for our standard parameters).

4. Ignite the torch flame and start the process with the software. The transmission will start to fluctuate when the fiber diameter starts to decrease.

5. Monitor the process: if the fiber arcs too much or the transmission amplitude fluctuations become too big, retract the torch 1 mm (usually a successful tapering requires 3 or 4 pullbacks).

6. When the amplitude fluctuations come back to their original pre-pull levels, the tapering is done so the software needs to be stopped if it did not do it on its own (and the torch flame put out).

7. Depending on the conditions, it might be necessary to manually pull the fiber a little bit more in order to make the taper taut.

8. Dismount the fiber from the pulling stage and mount it into the appropriate holder for the experiment.

Sometimes the fiber breaks before the process is finished. In that case, the only alternative is to stop and start again with a new section of fiber. The stretched

Pulling speed: 0.030 mm/s	Pulling time: 590 s
Torch initial position: 43 mm	Torch final position: 38 mm
Torch traversal speed: 5 mm/s	Torch traversal length: 6 mm
Minimum traversal length: 1 mm	α: 0.5

Table 6.1: Standard fiber stretching parameters. These are a general guide, and usually require fine-tuning.

fibers are very fragile, so they must be handled with the utmost care. Holding the fiber taut increases its resilience, but the slightest touch can still break it (or leave impurities that will scatter light and decrease the fiber transmission, sometimes to the point of making it unusable). Losses in the tapered fiber can be estimated by comparing the transmission before stretching to the one after; we have been able to obtain up to 80% transmission, but transmissions higher than 50% tend to be enough for all experiments.

6.5 Characterization of microspheres coupled to tapered fibers

6.5.1 Experimental setup

Coupling light in and out of the microsphere through a tapered fiber requires a fine control of the separation between the sphere and the fiber. We constructed a chamber with micropositioning devices where we could install the microsphere and the tapered fiber. A photograph of the chamber is in Fig. 6.12, while Fig. 6.13 shows a schematic view.

The microsphere is mounted on a 1/4" fiber chuck, which is magnetically affixed to a homemade Piezoelectric Disk Scanner (PDS)[1] which permits fine adjustments of its position up to range of a few micrometers using a homemade 12V driver. The tapered fiber is mounted on top of a homemade stick-slip piezoelectric

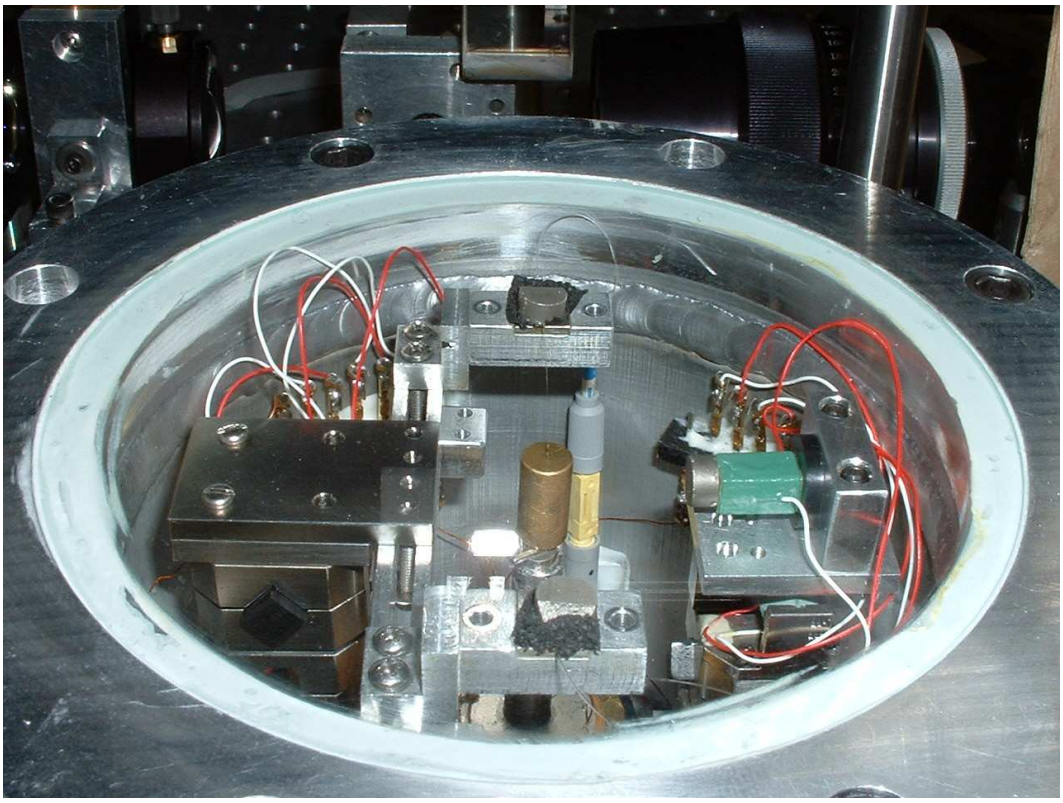

Figure 6.12: Photograph of the chamber constructed to perform the experiments.

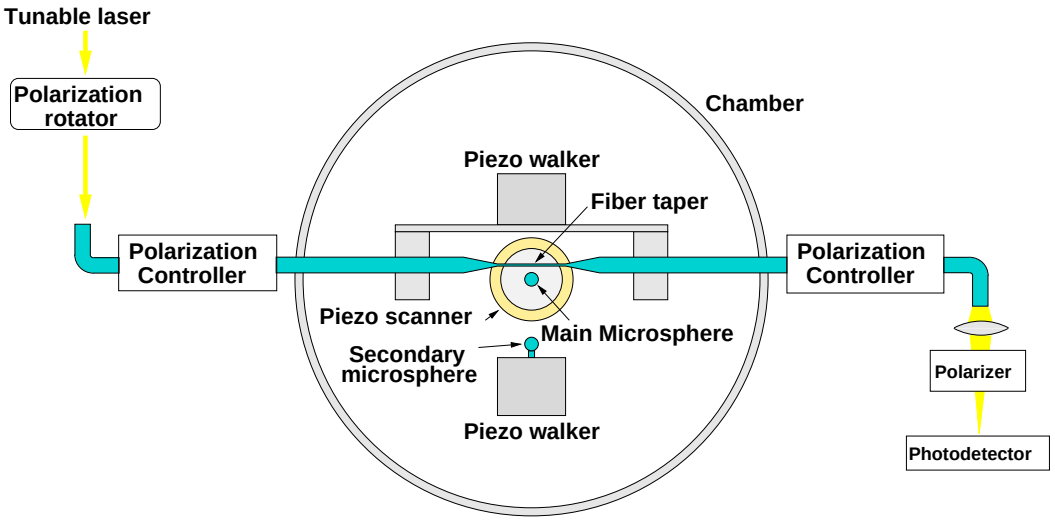

Figure 6.13: Schematic of the chamber from Fig. 6.12 and external elements.

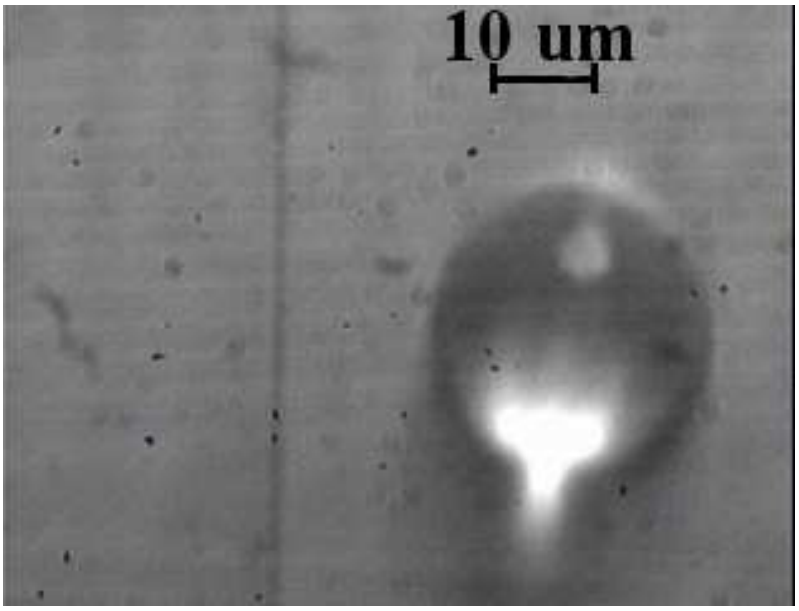

Figure 6.14: Sphere next to a tapered optical fiber.

walker[2]. The stick-slip design gives us a large range of coarse motion, and also a small range of fine position adjustment. Another walker, positioned opposite to the first one, lets us locate probes next to the sphere. The walkers were connected to a switch box and driven by a single Attocube ANC-150 controller. Vacuum electrical and fiber feedthroughs allow for evacuated operation of the chamber. Figure 6.14 shows a microscope image of a sphere next to a tapered fiber.

6.5.2 Transmission spectrum measurements

The most basic measurement of a waveguide coupled WGM resonator is a measurement of its transmission spectrum, where the transmission is recorded as a function of the incident laser frequency/wavelength. Our excitation laser is an external cavity New Focus Velocity 6320 diode laser with a coarse wavelength tunability range

[2]The design is based on the commercial Attocube walkers (http://www.attocube.com), but constructed in house

between 920 nm and 935 nm[3]. The fine tuning range of the laser frequency is 60 GHz. The setup is simple, and is depicted schematically in Fig. 6.13. The laser, whose polarization is set using a Newport PR-950 broadband polarization rotator, is coupled into the optical fiber using a New Focus 9091 single-mode fiber coupler. A General Photonics PLC-003-S-25 polarization controller compensates for stress-induced fiber birefringence[158] to keep the polarization of the light linear at the microsphere-fiber interface. The fiber is fed into the chamber, where the stretched section is held by the piezo walker so that it is close to the microsphere. The fiber then comes out of the chamber and its output is measured by a photodiode (Thorlabs PDA-10A). A function generator (Tektronix FG 501) generated a triangle wave to scan the laser frequency along the 60 GHz fine scanning range, while a computer captured the photodiode signal using a NI PCI-6229 data acquisition card (running xoscope 1.12[168] with custom patches and control scripts).

Measuring spectra is a straightforward process. It involves first taking a reference uncoupled spectrum (with the sphere and the fiber well separated) in order to compensate for changes in the laser intensity as the frequency is scanned, and then changing the sphere and fiber distance acquiring spectra for each desired configuration. The sphere-fiber distance needs to be very precisely controlled to avoid sticking one to the other. For that purpuose we could use the fine control on either the fiber walker or the resonator PDS. Most of the time we used the PDS to fine tune the sphere position relative to the fiber.

A typical transmission spectrum of a 73 μm diameter sphere is shown in Fig. 6.15, where the frequency shift is given respect to a center laser wavelength which in this case is 927.85 nm. A lot of sharp lines can be seen, corresponding to many different modes. The free spectral range of the sphere should be around 903 GHz, larger than the 60 GHz scanning range, implying that the modes must have different

[3]We chose this range with the idea of coupling to our InGaAs QDs. In retrospective, a laser near 1550 nm might had been a better choice.

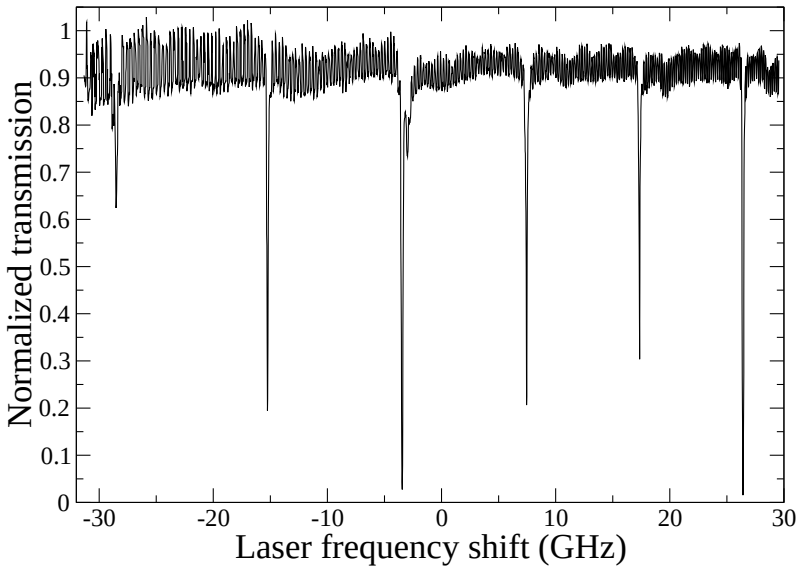

Figure 6.15: Transmission spectrum of a 73 μm diameter sphere.

combinations of l and m. The estimated value of l for these modes is $l \approx 346$. The narrowest lines agree with Q factors of about 6.1×10^6. In contraposition to the crowded spectrum of Fig. 6.15, the spectrum in Fig. 6.16 corresponding to a 22.5μm diameter sphere is much cleaner (the center wavelength is now 931.22nm). The free spectral range is now larger (2.9 THz), and we only see one mode. This mode has an estimated $l \approx 186$. The linewidth is now somewhat larger than those from the bigger sphere, but the Q factor of 4.4×10^6 is still very high. Given the cleaner spectra of smaller spheres, they will be preferable to larger ones if a small decrease in Q-factor is acceptable. For even smaller spheres it starts to become problematic to find the proper excitation frequency of the modes in the experiment, so diameters between 20 and 30 μm are optimal.

6.5.3 Coupling analysis

The distance between the fiber and the sphere will change the coupling between them. This coupling will be discussed in more detail in chapter 8, but for now

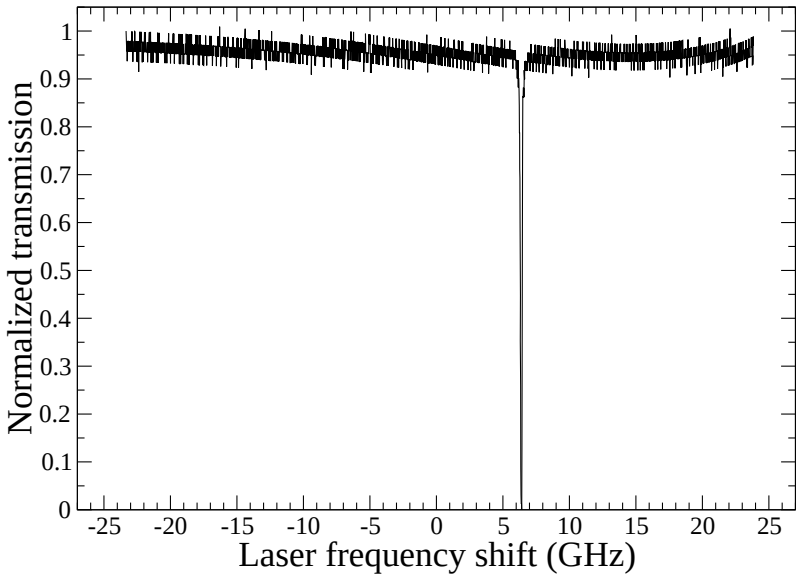

Figure 6.16: Transmission spectrum of a 22.5 μm diameter sphere.

it is enough to note that there are three distinct coupling regimes, for decreasing sphere-fiber distances:

- **Undercoupling**: Less that 100% of the incident fiber light is coupled into the sphere (non-zero transmission at resonance);
- **Critical coupling**: 100% of the incident light is coupled into the sphere and lost there (zero transmission at resonance);
- **Overcoupling**: 100% of the incident light is coupled into the sphere, but part of it can couple back into the fiber (non-zero transmission at resonance).

The linewidth of the resonance becomes progressively broader with decreasing sphere-fiber distance. It is dominated by the intrinsic resonator loss when undercoupled ($Q \approx Q_I$), but the loading of the cavity by the fiber becomes important as the coupling increases and eventually takes over the linewidth ($Q \approx Q_L$).

The progression of the spectrum change for the 22.5 μm diameter sphere can be appreciated in Fig. 6.17, where both the broadening of the line and the changes

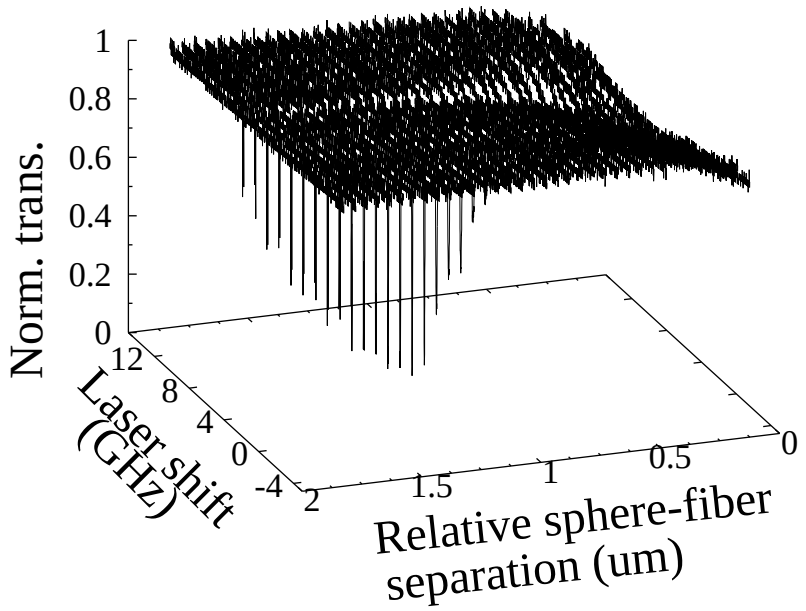

Figure 6.17: Evolution of the transmission spectrum for different sphere-fiber separations for the 22.5 μm diameter sphere.

in resonance transmission are very noticeable.

Chapter 7

Microsphere resonator sensors

The theoretical discussion of modes in spheres from section 6.1.1 reveals that the resonance frequency of the modes will depend on the refraction index of both the sphere and the surrounding material. The high Q factors of silica microspheres result in very narrow spectral lines which make measuring very small frequency shifts possible and thus provide an extremely sensitive indicator of refraction index changes (of either the sphere itself or its environment). This has already been used to measure the concentration of solutions[74], isotopes[9] and temperature changes[72] among others. With proper functionalization of the microsphere surface, biological molecules can be detected with very high resolution[10, 162, 163, 35].

7.1 Dielectric perturbations of the environment of a sphere: Theory

A simple theory to describe the resonance shift caused by a dielectric perturbation has been presented by Arnold *et al.*[10], and this section will briefly review it. More sophisticated and rigorous theories have also been put forward[151], but are not necessary for our purposes.

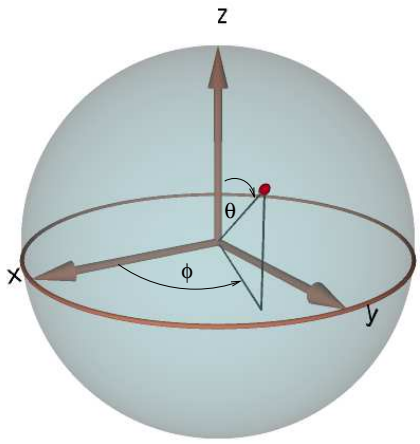

Figure 7.1: Schematic of a particle on the surface of a sphere.

The situation is described in Fig. 7.1, where a small particle (a molecule, a nanocrystal, etc.) is adsorbed in the sphere surface at a position $\vec{r}_i$. The basic physical idea is that the electric field in the resonator will induce a dipole in the particle which will in turn alter the energy of the resonant mode (and thus the resonant frequency).

It is possible to evaluate this in a quantitative way by looking at first order effects. The intra-cavity field distribution (assuming a single mode is excited) is $\vec{E}(\vec{r})e^{-i\omega t}$. This field has an evanescent tail that induces a dipole moment in the particle,

$$\delta\vec{p} = \alpha\vec{E}(\vec{r}_i), \tag{7.1}$$

where α is its polarizability[1]. The energy of this induced dipole is

$$\hbar(\delta\omega)_i = -\frac{\delta\vec{p}\cdot\vec{E}^*(\vec{r}_i)}{2}. \tag{7.2}$$

The proportional change in resonance frequency will be given by the ratio between this perturbation energy and the total mode energy,

$$\frac{(\delta\omega)_i}{\omega} \approx \frac{-\alpha|\vec{E}(\vec{r}_i)|^2}{2\int \varepsilon_s|\vec{E}(\vec{r})|^2\,\mathrm{d}V}. \tag{7.3}$$

We can further simplify the expression by restricting the integral in the denominator to the volume of the sphere (most of the field is confined there in any case), and then take the dielectric constant out of the integral (since the sphere is homogeneous):

$$\frac{(\delta\omega)_i}{\omega} \approx \frac{-\alpha|\vec{E}(\vec{r}_i)|^2}{2\varepsilon_s\int_{V_s}|\vec{E}(\vec{r})|^2\,\mathrm{d}V}. \tag{7.4}$$

If there are N identical particles, at positions $\{\vec{r}_i,\ldots,\vec{r}_N\}$, the total change will be just the sum of the individual changes:

$$\begin{aligned}\frac{\delta\omega}{\omega} &\approx \sum_{i=1}^{N}\frac{-\alpha|\vec{E}(\vec{r}_i)|^2}{2\varepsilon_s\int_{V_s}|\vec{E}(\vec{r})|^2\,\mathrm{d}V}\\ &\approx -\frac{\alpha}{2\varepsilon_s\int_{V_s}|\vec{E}(\vec{r})|^2\,\mathrm{d}V}\sum_{i=1}^{N}|\vec{E}(\vec{r}_i)|^2.\end{aligned} \tag{7.5}$$

If the particles' locations are confined to a small area, such that the field does not vary too much, the net result will be that the total perturbation will be proportional

[1] More specifically, it is the change in polarizability respect to the original medium, and is referred to as "excess polarizability" in Ref. [10].

to the number of particles interacting with the mode,

$$\frac{\delta\omega}{\omega} \approx N\left[\frac{-\alpha|\vec{E}(\vec{r}_i)|^2}{2\int \varepsilon_s|\vec{E}(\vec{r})|^2\,\mathrm{d}V}\right] \approx N\frac{(\delta\omega)_i}{w}. \tag{7.6}$$

7.2 An uninteresting perturbation: A fiber tip

One of the easiest perturbations to try is to bring a small fiber tip (with a diameter of the order of 1 μm) close to the sphere (in a geometry like that of Fig. 7.2). The results from Fig. 7.3 are as expected: a red shift in the resonance frequency, while the extra scattering induced by the tip decreases the Q factor. These changes were completely reversible: the resonance frequency and width would go back to their original levels after the tip was retracted.

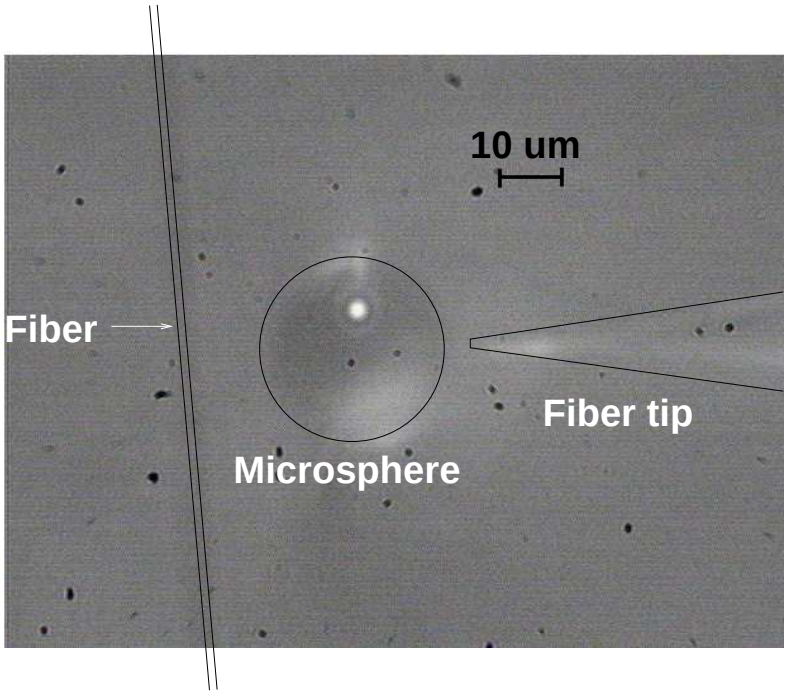

Figure 7.2: Fiber, sphere and tip geometry for the experiments.

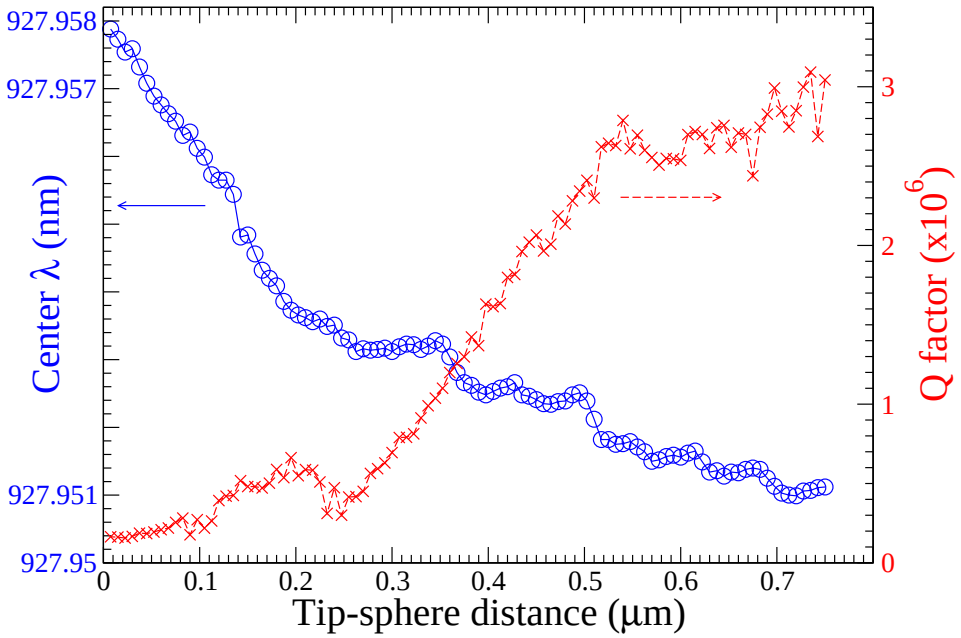

Figure 7.3: Resonance center and Q factor as a function of the distance between a bare tip and the sphere.

7.3 An interesting perturbation: Semiconductor nanocrystals

7.3.1 Experimental results

As a way to increase the change in the resonance frequency, we can dip the fiber tip in CdTe nanocrystals (the shift should be much larger due to the larger polarizability of the nanocrystals) solution[2]. The results are somewhat unexpected: While there is a resonance shift as the tip moves closer to the sphere, after a certain threshold distance the center of the resonance starts to shift with time even though the tip stays stationary. This time-dependent shift continues until the tip is retracted,

[2]The nanocrystals were an old sample provided by the Korgel group in Chemical Engineering. They showed no significant absorption or emission in the wavelength involved in the experiment.

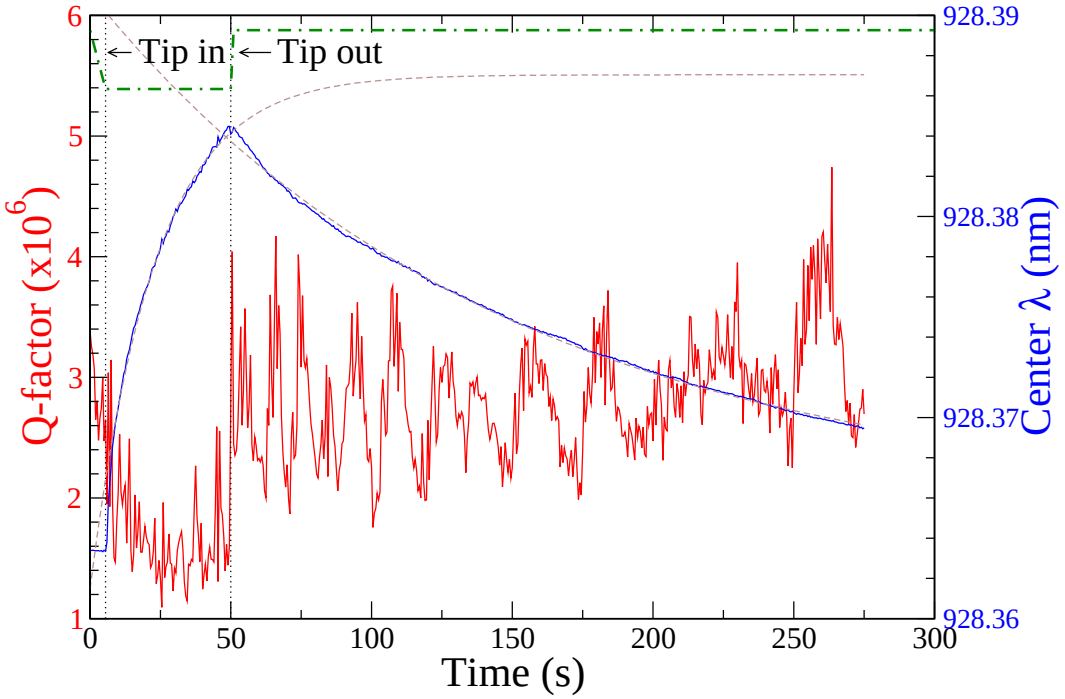

Figure 7.4: Resonance center shift and Q factor as a function of time for a nanocrystal coated tip.

when it reverses and drifts back towards the original resonance. The time-dependent resonance frequency center and the measured Q factor are plotted in Fig. 7.4, where vertical lines mark when the tip reached the threshold and when it was retracted.

7.3.2 A simple random hopping model

The behavior is quite intriguing, but a simple model can give some insight. This model is based on a few (reasonable) assumptions:

1. Each individual nanocrystal near the sphere causes the same amount of shift.

2. Nanocrystals can randomly "hop" into the sphere with a rate γ when the tip is closer than a certain threshold.

3. There is a limited number of spaces for nanocrystals (N_s) to hop into places

that will affect the WGM when the tip is there.

4. When the tip goes away, nanocrystals diffuse away from the mode until an equilibrium with N_R nanocrystals interacting with the WGM is reached.

The first assumption just tells us that the effect will be proportional on the number of nanocrystals interacting with the WGM, which we'll call $n_s(t)$.

The second and third assumptions (random hopping into a limited number of spaces) let us model the change in n_s as

$$\dot{n}_s(t) = \gamma(N_s - n_s). \tag{7.7}$$

Solving with $n_s(0) = 0$, we have that for times before the tip is retracted

$$n_s(t) = N_s(1 - e^{-\gamma t}). \tag{7.8}$$

After the tip is retracted at time $t = t_0$, nanocrystals start to diffuse away from the mode at a rate δ (which need not be equal to γ) until N_R are left, so we have

$$\dot{n}_s(t) = -\delta(n_s - N_R) \quad (t \geq t_0). \tag{7.9}$$

Combining equations (7.8) and (7.9) we find the full expression for the number of nanocrystals affecting the mode, proportional to the expected resonance shift:

$$n_s(t) = \begin{cases} N_s(1 - e^{-\gamma t}) & , t \leq t_0 \\ N_R(t_0) + [N_s(1 - exp^{-\gamma t_0}) - N_R(t_0)]e^{-\delta(t-t_0)} & , t \geq t_0. \end{cases} \tag{7.10}$$

The exponential shifts correspond very well with the data from Fig. 7.4, and using equation (7.10) to fit it, we obtain the values for the constants depicted in table 7.1.

Constant	Extracted value
γ	$0.044\,s^{-1}$
δ	$0.0069\,s^{-1}$

Table 7.1: Model constants extracted from the data in Fig. 7.4 using equation (7.10)

Chapter 8

Microsphere photonic devices

The field of photonics can be described as that encompassing the efforts to generate, manipulate and detect light. Its biggest application is in the area of telecommunications, where optical fiber links have made possible the huge increases in communication speeds in the recent years[76, 52]. Resonators play a very important role in photonics, especially in the generation and control of light. WGM resonators have been shown to have a myriad of applications in controlling light, for instance as add-drop filters[39, 107, 108], optical buffers[171, 170] and polarization-sensitive devices[26]. They become particularly interesting as components of integrated photonic circuits[6]. Microspheres, while not particularly convenient for integration, provide an excellent platform for studying phenomena in WGMs and prospective WGM-based devices.

8.1 Resonator modeling

8.1.1 Scalar formulation

We are interested in the general behavior of WGM resonators, so instead of using the most general approach in section 6.1.1 we'll use a "lumped model" instead[146, 140].

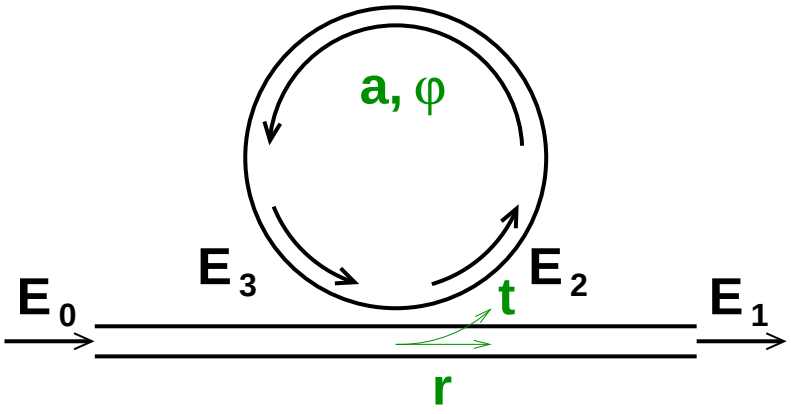

Figure 8.1: Lumped model of a ring resonator.

This model, summarized in Fig. 8.1, treats the resonator as a ring coupled to a waveguide and lumps the losses and the coupling into constants (the constants can be evaluated from the detailed expressions for the fields of the waveguide and the resonator, but that is not necessary to understand the basic phenomena). The losses in the resonator are represented by the single-pass attenuation constant a, while the fraction of the field coupled from the waveguide into the resonator (and viceversa) is t (both a and t are real numbers between 0 and 1). The single-pass phase the field acquires after one transit through the ring is $\varphi = 2\pi nR/\lambda = 2\pi nR\nu/c$ for a ring with radius R and refractive index n. With this in mind and inspection of Fig. 8.1 we can write down the equations that describe the system (where $r = \sqrt{1-t^2}$):

$$E_1 = rE_0 + itE_3, \tag{8.1}$$

$$E_2 = itE_0 + rE_3, \tag{8.2}$$

$$E_3 = ae^{i\varphi}E_2. \tag{8.3}$$

Straightforward algebra lets us find out the transmission through the coupled waveguide,

$$\frac{E_1}{E_0} = \tau = |\tau|e^{i\phi} = \frac{r - ae^{i\varphi}}{1 - rae^{i\varphi}}. \tag{8.4}$$

In our experiments, we measure the intensity of the transmitted field, so the relevant quantity is the normalized intensity transmission,

$$\left|\frac{E_1}{E_0}\right|^2 = |\tau|^2 = \left|\frac{r - ae^{i\varphi}}{1 - rae^{i\varphi}}\right|^2 . \tag{8.5}$$

An analysis of Eq. (8.4) shows that the transmission will have a minimum whenever φ is an integer multiple of 2π. Since the phase is identical to the single-pass optical path, for a ring of radius R and refraction index n we will have a resonance condition (where m is an integer)

$$\varphi_0 = \frac{2\pi n}{\lambda_0} 2\pi R = 2\pi m \rightarrow m\lambda_0 = 2\pi nR. \tag{8.6}$$

That is, there will be a resonance whenever the optical path in the ring is equal to an integer number of wavelengths.

Armed with Eq. (8.4), we can take a more detailed look at the waveguide-resonator coupling discussed in Sec. 6.5.3. The type of regime (under, over or critical coupling) can be determined by the relationship between r and a (with illustrative graphs in Fig. 8.2):

- $r > a$: The intrinsic resonator losses are smaller than the waveguide induced losses, and the resonator is **undercoupled**. The transmission shows a small, sharp feature at resonance.

- $r = a$: The intrinsic resonator loss is exactly equal to the waveguide induced loss, and the resonator is **critically coupled**. The transmission goes to zero at resonance, as all the light couples in and is dissipated inside the resonator.

- $r < a$: The waveguide induced loss now dominates, and light can couple out before being lost in the resonator. The resonator is **overcoupled**. The transmission at resonance increases, together with the width of the feature.

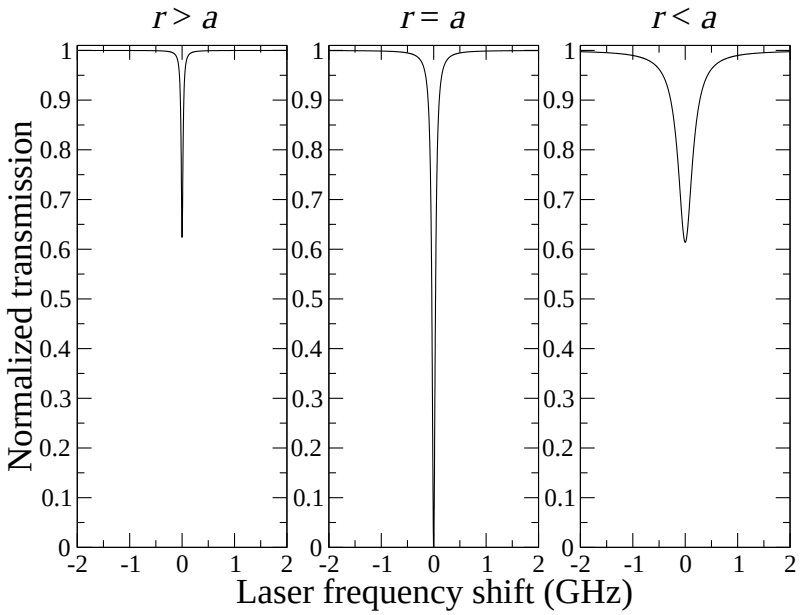

Figure 8.2: Different coupling regimes obtained from Eq. (8.4) with varying values of r for fixed a.

8.1.2 Vector formulation

The model used in the previous section is scalar, in the sense that it does not take into account the polarization of the fields. We can extend it in a simple way to take into account the polarization of the resonant and waveguide modes using Jones matrices[92]. Using the polarization eigenmodes ($\hat{x}$ and $\hat{y}$) of the resonator as a natural basis, the Jones matrix of the resonator (assuming a single $\hat{y}$-polarized resonance) is:

$$\mathbf{R} = \begin{bmatrix} 1 & 0 \\ 0 & |\tau| e^{i\phi} \end{bmatrix}. \tag{8.7}$$

If we furthermore add a polarizer (see Figure 8.3 for a graphical representation) after the waveguide has interacted with the resonator, the final field will be $\vec{E}_f =$

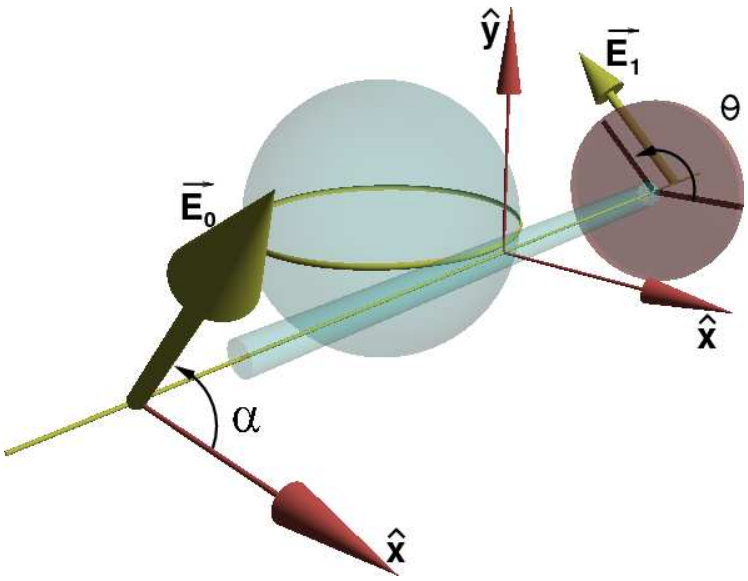

Figure 8.3: Graphical representation of the vector model. The reference axes are given by the natural polarizations of the resonator. The input field makes an angle α with the $\hat{x}$ axis, while the analyzer axis is at an angle θ.

$\mathbf{P}(\theta)\mathbf{R}\vec{E}_0$, where

$$\mathbf{P}(\theta) = \begin{bmatrix} \cos^2\theta & \cos\theta\sin\theta \\ \sin\theta\cos\theta & \sin^2\theta \end{bmatrix} \tag{8.8}$$

is the Jones matrix corresponding to a polarizer whose axis makes an angle θ with the previously defined $\hat{x}$-axis. The measured intensity after the polarizer will be

$$\begin{aligned} I(\theta) &= \vec{E}_f^{\dagger} \cdot \vec{E}_f \\ &= \vec{E}_0^{\dagger} \cdot \mathbf{R}^{\dagger}\mathbf{P}^{\dagger}(\theta)\mathbf{P}(\theta)\mathbf{R}\vec{E}_0 \\ &= E_0^2 \left[\cos^2\alpha\cos^2\theta + |\tau|^2\sin^2\alpha\sin^2\theta + \frac{\sin(2\alpha)\sin(2\theta)}{2}|\tau|\cos(\phi_0+\phi)\right] \end{aligned} \tag{8.9}$$

for a general input field $\vec{E}_0 = E_0 \begin{bmatrix} \cos\alpha \\ e^{i\phi_0}\sin\alpha \end{bmatrix}$.

8.2 Polarization conversion

8.2.1 Modelling

To study polarization conversion, we are interested in the case where the initial polarization is linear and makes a 45° angle with the $\hat{x}$-axis ($\alpha = \pi/4; \phi_0 = 0$). In that case, Eq. (8.9) becomes

$$I(\theta) = \frac{E_0^2}{2}\left(\cos^2\theta + |\tau|^2 \sin^2\theta + \sin(2\theta)|\tau|\cos\phi\right) \tag{8.10}$$

Eq. (8.10) expresses the standard result for the transmission coefficient through a birefringent plate with attenuation $|\tau|$ and phase difference between the fast and slow axis ϕ. Depending on the value of ϕ, the transmitted intensity can be maximized for different detection angles θ, as the polarization of the light after the waveplate changes. A phase shift of π (corresponding to a half-waveplate) results in a 90-degree rotation of the polarization, observed as a maximum transmitted intensity at $\theta = -\pi/4$. In contrast with the original proposal by Little and Chu[109] to tilt the resonator modes, our idea is to tilt the waveguide modes.

The polarization behavior is more interesting than that of a simple waveplate when we take into account the transmission function of the ring resonator (8.4). At resonance, the transmission becomes simply

$$\tau = \frac{r-a}{1-ra}. \tag{8.11}$$

Depending on the relative magnitude of the resonator losses and the coupling, we can find two different regimes. The undercoupled regime, for $r > a$, occurs when the losses are larger than the coupling and the phase shift at resonance is just zero. When the coupling overcomes the losses ($r < a$), the phase shift now becomes $\phi = \pi$, giving us a behavior similar to that of a half-waveplate, capable of significantly altering

the polarization of the incident light.

We can combine Eq. (8.10) and Eq. (8.11) to obtain the expected transmitted intensities at polarizations both parallel ($\theta = \pi/4$) and perpendicular ($\theta = -\pi/4$) to the input one:

$$I\left(\pm\pi/4\right) = \frac{E_0^2}{4}\left[\frac{(r \pm 1)(1 \mp a)}{1 - ra}\right]^2 \tag{8.12}$$

We can study this expression to obtain some quantitative information on the polarization conversion. For instance, we would expect no conversion when there is no coupling ($r = 1$) and a complete conversion for full coupling ($r = 0$), where no power is detected on the original polarization and all the power (minus resonator losses) is detected on the orthogonal one. Also, the total loss depends strongly on the coupling. In the undercoupled regime the loss increases sharply with the coupling, as more light becomes coupled into the resonator and lost there. At the point of critical coupling ($r = a$) there is a maximum loss of half the input field. Once in the overcoupled regime, the loss starts decreasing (although more slowly) until it reaches its minimum at full coupling. Since reaching the overcoupled regime becomes easier for lower resonator losses, it is also clear that this phenomenon will be easier to observe in resonators with large quality factors. In the fully coupled case ($r = 0$), the conversion would be almost complete, with just a fraction lost of the input, which is equal to the single-pass resonator loss ($1 - a$). Given that resonances for low-loss resonators are sharp, they are very appropriate for wavelength-dependent devices such as polarization-sensitive add-drop filters. However, as the resonances become broader when the coupling increases, the conversion also becomes less wavelength sensitive. However, it remains to be seen if this broadening can be made large enough so that it can be used for practical broadband devices.

8.2.2 Experimental results

We used the experimental setup described in Chapter 6 (see Fig. 6.13 for details), making use now of the polarization control elements. The polarization rotator set the polarization of the laser which was then coupled into the optical fiber using a free-space coupler. A polarizer and an amplified photodiode at the fiber output were used to analyze the transmitted light.

Space constraints in the chamber and limitations on the arrangement of the optical fiber caused bending of the fiber in different locations and subsequent scrambling of the input polarization. As a way to compensate for these changes in the polarization, we used two polarization controllers. The first one preceded the fiber taper, compensating for polarization changes up to the position of the microsphere. The second controller was placed after the fiber taper to ensure the linearity of the output polarization.

We used the following procedure to measure the degree of polarization conversion. First, the incoming polarization was selected by using the polarization rotator. Then we adjusted the first polarization controller to ensure the polarization at the fiber taper was linear and matched to one set of modes (which we define to be the polarization with $\alpha = 0$). The next step was to uncouple the taper from the sphere and make sure the output polarization was linear (we achieved this by turning the detection polarizer to its position for minimum transmission, $\theta = \pi/2$, and then minimizing this transmission further with the second polarization controller). Rotating the polarizer 90 degrees ($\theta = 0$) resulted in maximum transmission, with a contrast of about 95%, confirming the linear polarization of the output light. Finally, we measured transmission spectra for different conditions.

Figure 8.4 shows the spectra of a 73 μm sphere under different excitation and detection polarizations. The conversion can be seen clearly for several different modes for $\alpha = \pi/4$ and $\theta = -\pi/4$.

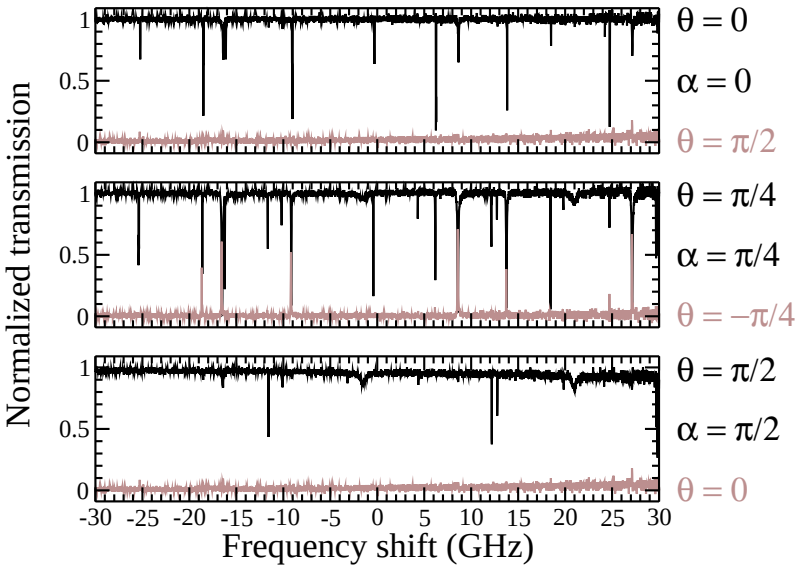

Figure 8.4: Demonstration of polarization conversion on a 73 μm diameter sphere.

For a more quantitative comparison between the model and experiment, we used another sphere with a diameter of 22 μm, as measured under an optical microscope, so the mode spectrum would be cleaner.

In order to ensure the validity of the model's assumptions (a single resonant mode, possessing a well defined polarization) we measured transmission spectra using different combinations of input and detection polarizations, shown in Fig. 8.5. The top and bottom panels in Fig. 8.5 clearly show that only the vertical ($\alpha = \pi/2$) polarization exhibits resonant coupling to the microsphere. Since no polarization mixing is observed, we can be certain that the resonance is a true eigenmode of the waveguide-microsphere system. Also, the shallowness of the transmission dip in the bottom panel indicates the system is in the overcoupled regime. In the middle panel, we can see strong polarization conversion as predicted for an input polarization with $\alpha = \pi/4$.

We also measured spectra at different fiber-sphere separations to study the conversion as the coupling to the resonator changed, as shown in Fig. 8.6. After

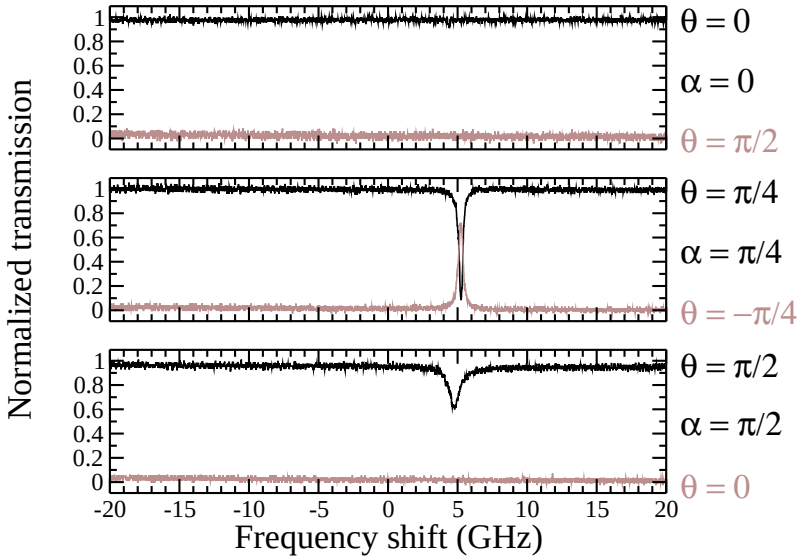

Figure 8.5: Transmission spectra for different input polarizations, verifying the model assumptions (see text). The dark (light) traces correspond to the detection polarizer parallel (perpendicular) to the input polarization.

taking each spectra, we extracted (using a numerical fit) the coupling coefficient r and the maximum (if the input and detected polarizations were orthogonal) or minimum (for parallel polarizations) transmitted intensity. Fig. 8.7 shows a summary of the extracted data, together with fits to Eq. (8.12). The agreement is reasonable within the experimental error, and we were able to measure conversion efficiencies near 100% for the strongest couplings between the fiber and the sphere. The flatness of the curves as r goes closer to zero implies that, provided the interaction between the waveguide and the resonator is strong enough, the polarization conversion is a robust phenomenon, only weakly affected by small changes in the coupling coefficient. This robustness suggests the phenomenon could be useful for photonic devices. On the contrary, if the coupling is weak (r close to 1) then the conversion is highly dependent on it and thus it could be more appropriate for sensing purposes.

Summarizing, we were able to show close to 100% efficient polarization conversion in a silica microsphere coupled to a tapered optical fiber and studied the

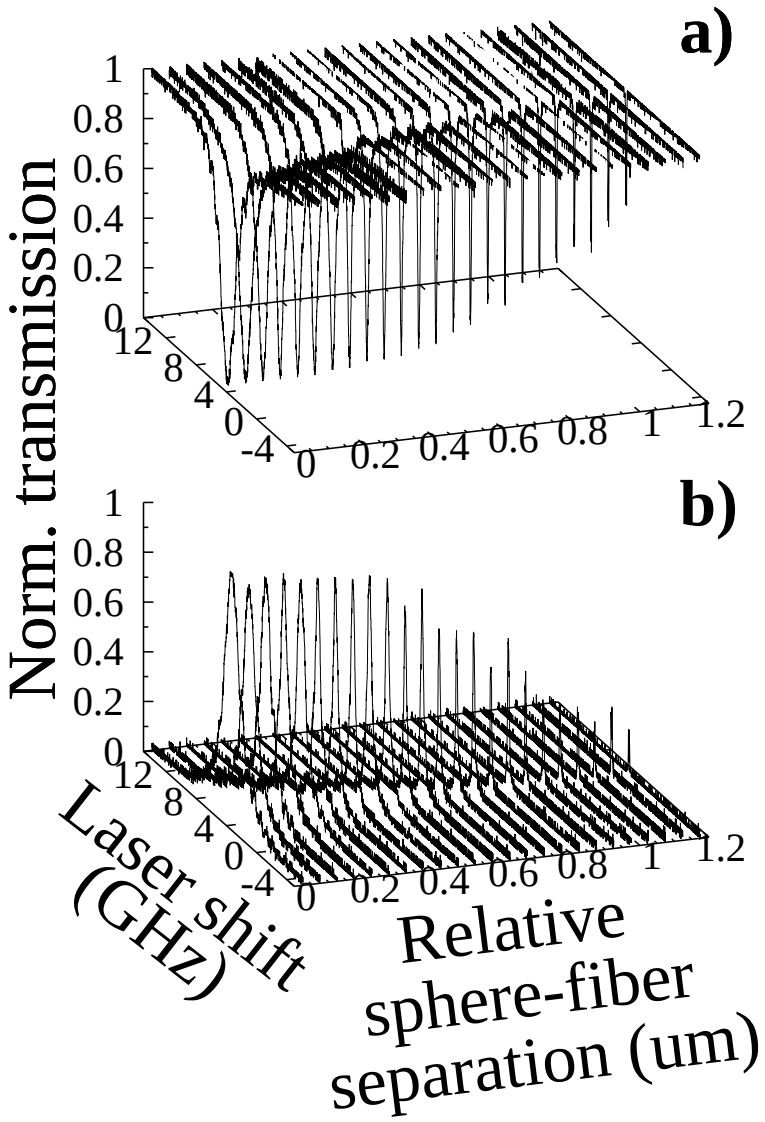

Figure 8.6: **a)** Transmission spectra for different separations between the optical fiber and the sphere (more negative voltage corresponds to a smaller separation. Both the input polarization (α) and detection (θ) angles are equal to $\pi/4$.
b) Polarization converted spectra, with the input polarization angle $\alpha = \pi/4$ and detection angle $\theta = -\pi/4$.

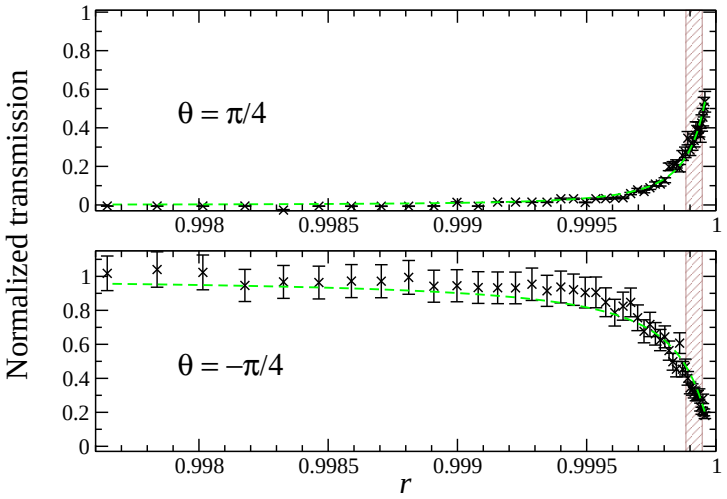

Figure 8.7: Transmission as a function of coupling strength (the smaller r is, the stronger the coupling is) for an input polarization angle $\alpha = \pi/4$. Transmission for the parallel polarization (top graph) decreases quickly as the coupling increases. The polarization conversion (bottom graphs) increases with the coupling. The dashed lines are fits to equation 8.12. The grayed area indicates the a coefficient of the microsphere, $a = 0.99991 \pm 0.00003$.

efficiency of the conversion as a function of the coupling between the resonator and the waveguide. A simple ring resonator model quantitatively describes the phenomenon. This effect is most likely universal for whispering gallery mode resonators, and could have useful applications in polarization-sensitive photonic devices.

Chapter 9

Conclusions and outlook

This excursion on confined electrons and confined light has touched three main fields, and several areas on each. In closing, let's take a broader perspective and ponder what has been done and could be done in the future.

Quantum Information is a very exciting field, that has experienced tremendous growth recently. Based on our understanding of the quantum mechanical properties of semiconductor quantum dots, they don't seem to provide a good scalable system for doing quantum computation (although future advances might change that), and there are better alternatives right now. However, even if you can't use them to build a "practical" quantum computer, they can still contribute to the study of basic ideas. In particular, the development of a resonance fluorescence technique already allows quantum manipulations of the dots more sophisticated than what was described in this work. Advances in techniques such as quantum process tomography might shed more light into both the quantum dots themselves and quantum information ideas in the near future.

For Quantum Optics, it has already been established that the combination of quantum dots and microresonators is a very attractive avenue for the study of basic phenomena in Cavity Quantum Electrodynamics. Microsphere resonators have

shown potential in this area, but the technical hurdles involved in coupling them to semiconductor quantum dots (especially epitaxially grown ones) are large. So far, photonic crystal microcavities have demonstrated the best technical capabilities and the largest versatility for basic studies. This is still an area of ongoing basic research, but there is hope that in the medium term this area will be mature enough to support real applications to techology.

Microsphere resonators really shine as ultra-sensitive sensors. Due to their very sharp spectral features, their sensitivity to dielectric perturbations, and the possibility of functionalizing their surface, they could result in very compact, ultra-sensitive biologic and chemical sensors.

The field of Photonics is another area where microsphere resonators are useful, not so much as devices themselves (although that can not be discounted) but rather as a playground for looking into new and useful phenomena in WGM resonators. While integrated resonators in photonic devices are more prone to become commercial devices, the low losses of microspheres, their ease of fabrication and characterization and the ability to easily change their parameters make them excellent for prototyping new uses of WGM resonators.

In this work, we explored all the areas mentioned above. We implemented a quantum algorithm in a single quantum dot. We then tried (unsuccessfully) to couple self-assembled semiconductor quantum dots to microsphere resonators. The efforts then turned into investigating the resonators, showing their sensing properties as well as uncovering a new way to use them as a polarization-sensitive photonic device. So, finally, it all ends in light.

Appendix A

Quantization of the electromagnetic field

This appendix details a semi-formal procedure to quantize the electromagnetic field in a cavity.

A.1 Quantization of a field in a cavity

In a isotropic, homogeneous and medium the electromagnetic field obeys the following Maxwell's equation:

$$\nabla \times \vec{E} = -\frac{\partial \vec{B}}{\partial t}, \quad \nabla \times \vec{B} = \mu\varepsilon \frac{\partial \vec{E}}{\partial t} \tag{A.1}$$

$$\nabla \cdot \vec{E} = 0, \quad \nabla \cdot \vec{B} = 0. \tag{A.2}$$

Instead of working with the fields, we will work with the vector potential $\vec{A}$ in the Coulomb gauge. In this gauge, the potential is divergenceless and satisfies a

homogeneous differential equation,

$$\nabla \cdot \vec{A} = 0, \quad \nabla^2 \vec{A} - \mu\varepsilon \frac{\partial^2 \vec{A}}{\partial t^2} = 0; \tag{A.3}$$

and the fields are given as

$$\vec{E} = -\frac{\partial A}{\partial t}, \tag{A.4}$$

$$\vec{B} = \nabla \times \vec{A}. \tag{A.5}$$

Looking at Eq. (A.3) and assuming a harmonic time dependence for $\vec{A}$, we find that is must satisfy a vector Helmholtz equation:

$$\nabla^2 \vec{A} + k^2 \vec{A}_{\vec{k}} = 0, \tag{A.6}$$

with $k^2 = \omega\varepsilon\mu$.

Following the procedure outlined in section 6.1.1, we can find a generating function ϕ and two complete orthonormal sets of divergenceless functions $\left\{\vec{M}_{\vec{k}}\right\}$ and $\left\{\vec{N}_{\vec{k}}\right\}$ which satisfy the Helmholtz equation and are compatible with the system symmetry. A general solution for $\vec{A}$ can be written as

$$\vec{A} = \frac{1}{\sqrt{\varepsilon}} \sum_{\vec{k}} a_{\vec{k}} \vec{M}_{\vec{k}} e^{i\omega_{\vec{k}} t + c.c.}. \tag{A.7}$$

Note that in Eq. (A.7) we could have used $N_{\vec{k}}$ instead of $\vec{M}_{\vec{k}}$, corresponding to a different solution (TM vs. TE for the spherical case). The set of permitted frequencies $\left\{\omega_{\vec{k}}\right\}$ can be determined later by using the corresponding boundary conditions as done in Sec. 6.1.1. Also note that, by construction, it holds that ($V_{\vec{k}}$

is a normalization constant)

$$\int_V \vec{M}^*_{\vec{k}'}(\vec{r}) \cdot \vec{M}_{\vec{k}}(\vec{r}) \mathrm{d}^3 r = \int_V \vec{N}^*_{\vec{k}'}(\vec{r}) \cdot \vec{N}_{\vec{k}}(\vec{r}) \mathrm{d}^3 r = V_{\vec{k}} \delta_{\vec{k}',\vec{k}}. \tag{A.8}$$

Using Eqs. (A.4) and (A.5) we can write the fields in terms of these functions

$$\vec{E} = i \sum_{\vec{k}} \frac{1}{\sqrt{\varepsilon V_{\vec{k}}}} \omega_{\vec{k}} a_{\vec{k}} \vec{M}_{\vec{k}} e^{i\omega_{\vec{k}} t} + c.c., \tag{A.9}$$

$$\vec{B} = \sum_{\vec{k}} \frac{-k}{\sqrt{\varepsilon V_{\vec{k}}}} \omega_{\vec{k}} a_{\vec{k}} \vec{N}_{\vec{k}} e^{i\omega_{\vec{k}} t} + c.c.. \tag{A.10}$$

$$\tag{A.11}$$

The field Hamiltonian is equal to its time averaged energy,

$$H = \frac{1}{2} \int_V \left(\varepsilon |\vec{E}|^2 + \frac{1}{\mu} |\vec{B}|^2 \right) \mathrm{d}^3 r. \tag{A.12}$$

But

$$\int_V |\vec{E}|^2 \mathrm{d}^3 r = \sum_{\vec{k},\vec{k}'} \frac{1}{\varepsilon V_{\vec{k}}} \omega^*_{\vec{k}'} \omega_{\vec{k}} a^*_{\vec{k}'} e^{-i\omega_{\vec{k}'}} a_{\vec{k}} e^{i\omega_{\vec{k}}} \int_V \vec{M}^*_{\vec{k}'}(\vec{r}) \cdot \vec{M}_{\vec{k}}(\vec{r}) \mathrm{d}^3 r \tag{A.13}$$

$$= \frac{1}{\varepsilon} \sum_{\vec{k}} \omega^2_{\vec{k}} |u_{\vec{k}}(t)|^2, \tag{A.14}$$

where $u_{\vec{k}}(t) = e^{i\omega_{\vec{k}}}$, and similarly

$$\int_V |\vec{B}|^2 \mathrm{d}^3 r = \mu \omega^2_{\vec{k}} |u_{\vec{k}}(t)|^2. \tag{A.15}$$

Replacing Eqs. (A.14) and (A.15) into Eq. (A.12) we find

$$H = \sum_{\vec{k}} \omega^2_{\vec{k}} |u_{\vec{k}}(t)|^2. \tag{A.16}$$

We can do a canonical transformation,

$$q_{\vec{k}} = u_{\vec{k}} + u^*_{\vec{k}}, \quad p_{\vec{k}} = -i\omega_{\vec{k}}(u_{\vec{k}} - u^*_{\vec{k}}), \tag{A.17}$$

and the Hamiltonian will become equivalent to that of a collection of harmonic oscillators:

$$H = \frac{1}{2}\sum_{\vec{k}} \left(p^2_{\vec{k}} + \omega^2_{\vec{k}} q^2_{\vec{k}}\right). \tag{A.18}$$

We can do a canonical transformation,

$$q_{\vec{k}} = u_{\vec{k}} + u^*_{\vec{k}}, \quad p_{\vec{k}} = -i\omega_{\vec{k}}(u_{\vec{k}} - u^*_{\vec{k}}), \tag{A.19}$$

and the Hamiltonian will become equivalent to that of a collection of harmonic oscillators:

$$H = \frac{1}{2}\sum_{\vec{k}} \left(p^2_{\vec{k}} + \omega^2_{\vec{k}} q^2_{\vec{k}}\right), \tag{A.20}$$

where $q_{\vec{k}}$ and p_{vk} are classical canonical variables called "quadratures" satisfying

$$\dot{q}_{\vec{k}} = \frac{\partial H}{\partial p_{\vec{k}}}, \quad \dot{p}_{\vec{k}} = -\frac{\partial H}{\partial q_{\vec{k}}}. \tag{A.21}$$

We have a classical Hamiltonian for the field, so we can obtain a quantized version by just replacing the dynamical variables by operators:

$$\hat{H} = \frac{1}{2}\sum_{\vec{k}} \left(\hat{p}^2_{\vec{k}} + \omega^2_{\vec{k}} \hat{q}^2_{\vec{k}}\right), \tag{A.22}$$

Since the Hamiltonian is just a collection of harmonic oscillators, we can introduce the corresponding creation and annihilation operators,

$$\hat{a}_{\vec{k}}(t) = \frac{1}{\sqrt{2\hbar\omega_{\vec{k}}}}\left[\omega_{\vec{k}}\hat{q}(t)_{\vec{k}} + i\hat{p}(t)_{\vec{k}}\right], \quad \hat{a}^\dagger_{\vec{k}}(t) = \frac{1}{\sqrt{2\hbar\omega_{\vec{k}}}}\left[\omega_{\vec{k}}\hat{q}(t)_{\vec{k}} - i\hat{p}(t)_{\vec{k}}\right]; \tag{A.23}$$

and a rewritten Hamiltonian of the form

$$\hat{H} = \sum_{\vec{k}} \hbar\omega_{\vec{k}} \left[\hat{a}^{\dagger}_{\vec{k}}(t)\hat{a}_{\vec{k}}(t) + \frac{1}{2} \right]. \tag{A.24}$$

Finally, we can retrace our steps to Eqs. (A.10) and (A.11) to obtain the quantum mechanical expression for the fields in term of the creation and annihilation operators

$$\vec{E} = i \sum_{\vec{k}} \sqrt{\frac{\hbar\omega_{\vec{k}}}{2\varepsilon V_{\vec{k}}}} \left[\hat{a}^{\dagger}_{\vec{k}}(t)\vec{M}_{\vec{k}}(\vec{r}) + \hat{a}_{\vec{k}}(t)\vec{M}^{*}_{\vec{k}}(\vec{r}) \right], \tag{A.25}$$

$$\vec{B} = \sum_{\vec{k}} -k \sqrt{\frac{\hbar\omega_{\vec{k}}}{2\varepsilon V_{\vec{k}}}} \left[\hat{a}^{\dagger}_{\vec{k}}(t)\vec{N}_{\vec{k}}(\vec{r}) + \hat{a}_{\vec{k}}(t)\vec{N}^{*}_{\vec{k}}(\vec{r}) \right]. \tag{A.26}$$

A.2 Fully quantized interaction Hamiltonian

We can use the fully quantized field in Eq. (2.7) so that the fully quantized interaction Hamiltonian in the dipole approximation is

$$\hat{H}_{\text{int}} = -\hat{\vec{d}} \cdot \hat{\vec{E}} = -i \sum_{\vec{k}} \sqrt{\frac{\hbar\omega_{\vec{k}}}{2\varepsilon V_{\vec{k}}}} \vec{d} \cdot \vec{M}_{\vec{k}}(\vec{r}_0)(\hat{\sigma}_{+} + \hat{\sigma}_{-})(\hat{a}_{\vec{k}} + \hat{a}^{\dagger}_{\vec{k}}). \tag{A.27}$$

Rotating wave approximation

Just for illustration purposes, we will take a somewhat different approach to the Rotating Wave Approximation for the quantum Hamiltonian, which is equivalent to the one used for the semiclassical case used in Chapter 2. If we consider the system and the field without interactions in the Heisenberg picture, the system and field operator will have simple expressions,

$$\hat{\sigma}_{+}(t) = \hat{\sigma}_{+}(0)e^{-i\omega_0 t}, \quad \hat{a}_{\vec{k}}(t) = \hat{a}_{\vec{k}}(0)e^{-i\omega_{\vec{k}} t}. \tag{A.28}$$

The interaction Hamiltonian A.27 has all four combination of the atomic and field operators ($\hat{\sigma}_+\hat{a}^\dagger$, $\hat{\sigma}_+\hat{a}$, $\hat{\sigma}_-\hat{a}^\dagger$ and $\hat{\sigma}_-\hat{a}$). Using the free evolution expressions for two of these combinations we get

$$\hat{\sigma}_+(t)\hat{a}^\dagger(t) = \hat{\sigma}_+(0)\hat{a}^\dagger(0)e^{i(\omega_0+\omega_{\vec{k}})t} \quad (A.29)$$

$$\hat{\sigma}_-(t)\hat{a}(t) = \hat{\sigma}_+(0)\hat{a}^\dagger(0)e^{-i(\omega_0+\omega_{\vec{k}})t}. \quad (A.30)$$

These two pairs always evolve at optical frequencies. On the other hand, the other two pairs have a time dependence that varies slowly near a resonance:

$$\hat{\sigma}_+(t)\hat{a}(t) = \hat{\sigma}_+(0)\hat{a}^\dagger(0)e^{i(\omega_0-\omega_{\vec{k}})t}, \quad (A.31)$$

$$\hat{\sigma}_-(t)\hat{a}^\dagger(t) = \hat{\sigma}_+(0)\hat{a}^\dagger(0)e^{-i(\omega_0-\omega_{\vec{k}})t}. \quad (A.32)$$

The contribution of the operator pairs that oscillate at optical frequencies will average to zero after a few optical oscillation cycles have passed, while the others will have a significant effect. Thus, we can discard the terms with high-frequency oscillations (A.29,A.30), and obtain the RWA Hamiltonian,

$$\hat{H}^{\mathrm{RWA}} = \frac{\hbar\omega_0}{2}\hat{\sigma_z} + \sum_{\vec{k}} \hbar\omega_{\vec{k}} \left[\hat{a}^\dagger_{\vec{k}}\hat{a}_{\vec{k}} + \frac{1}{2}\right] - i\sum_{\vec{k}} \sqrt{\frac{\hbar\omega_{\vec{k}}}{2\varepsilon V_{\vec{k}}}}\vec{d}\cdot\vec{M}_{\vec{k}}(\vec{r}_0)(\hat{\sigma}_+\hat{a}_{\vec{k}} + \hat{\sigma}_-\hat{a}^\dagger_{\vec{k}}). \quad (A.33)$$

This fully quantized Hamiltonian can be used as a base for the theoretical understanding of many quantum optical effects.

Appendix B

Calculating WGM resonances

At times it is convenient to be able to find there resonant frequency of a given whispering gallery mode by solving the transcendental resonance equations (6.30) (for TE modes) or (6.33) (for TM modes). This solution is not difficult to implement using a standard root solver. But depending on the available numerical libraries, it is convenient to rewrite those equations in a simpler way. We can start by writing (for a given l number)

$$[xh_l^{(1)}(x)]'\mu_0 b^2 j_l(bx) - h_l^{(1)}(x)\mu_s[bxj_l(bx)]' = 0 \quad \text{for TM modes } (a_l), \tag{B.1}$$

$$[xh_l^{(1)}(x)]'\mu_s j_l(bx) - h_l^{(1)}(x)\mu_0[bxj_l(bx)]' = 0 \quad \text{for TE modes } (b_l); \tag{B.2}$$

where $b = \frac{n_s}{n_0}$ n_s, μ_s are the refraction index and magnetic permeability of the sphere, n_0 and μ_0 are the refraction index and magnetic permeability of the medium surrounding the sphere and $x = \frac{2\pi n_0 a}{\lambda_0}$. a is the radius of the sphere and λ_0 is the wavelength in the outside medium. j_l is the spherical Bessel function of the first kind and l-th order and $h_l^{(1)}$ is the spherical Hankel function of the first kind and l-th order. The prime indicates differentiating with respect to the argument of the spherical Bessel function.

We can rearrange the constants a little,

$$\mu_s \left\{ [x h_l^{(1)}(x)]' \frac{\mu_0 b^2}{\mu_s} j_l(bx) - h_l^{(1)}(x)[bx j_l(bx)]' \right\} = 0 \quad \text{for TM modes,} \tag{B.3}$$

$$\mu_0 \left\{ [x h_l^{(1)}(x)]' \frac{\mu_s}{\mu_0} j_l(bx) - h_l^{(1)}(x)[bx j_l(bx)]' \right\} = 0 \quad \text{for TE modes.} \tag{B.4}$$

And finally, combine both expressions into,

$$\beta \left\{ [x h_l^{(1)}(x)]' \eta^2 j_l(bx) - h_l^{(1)}(x)[bx j_l(bx)]' \right\} = 0, \tag{B.5}$$

where

$$\text{for TM modes} \begin{cases} \eta^2 = \dfrac{\mu_0 b^2}{\mu_s} \\ \beta = \mu_s \end{cases}, \quad \text{for TE modes} \begin{cases} \eta^2 = \dfrac{\mu_s}{\mu_0} \\ \beta = \mu_0 \end{cases}. \tag{B.6}$$

Let's first split the derivatives, converting expression (B.5) into

$$\beta \left\{ [h_l^{(1)}(x) + x h_l'^{(1)}(x)] \eta^2 j_l(bx) - h_l^{(1)}(x)[j_l(bx) + bx j_l'(bx)] \right\} = 0. \tag{B.7}$$

We can eliminate the derivatives by using a spherical Bessel function identity (z is any Bessel or Hankel spherical function),

$$z_l'(x) = z_{l-1}(x) - \frac{l+1}{x} z_l(x), \tag{B.8}$$

obtaining

$$\begin{aligned} \beta \Bigg\{ & \left[h_l^{(1)}(x) + x \left(h_{l-1}^{(1)}(x) - \frac{l+1}{x} h_l^{(1)}(x) \right) \right] \eta^2 j_l(bx) \\ & - h_l^{(1)}(x) \left[j_l(bx) + bx \left(j_{l-1}(bx) - \frac{l+1}{bx} j_l(bx) \right) \right] \Bigg\} = 0. \end{aligned} \tag{B.9}$$

We can simplify this a little bit by taking out some common factors:

$$\beta\left\{\left[xh_{l-1}^{(1)}(x)-lh_{l}^{(1)}(x)\right]\eta^{2}j_{l}(bx)-\left[bxj_{l-1}(bx)-lj_{l}(bx)\right]h_{l}^{(1)}(x)\right\}=0. \quad \text{(B.10)}$$

Now, the Hankel function can be written as a linear combination of Bessel functions of the first and second kind,

$$h_{l}^{(1)}(x)=j_{l}(x)+iy_{l}(x). \quad \text{(B.11)}$$

Consequently, equation B.10 now becomes

$$\begin{aligned}\beta\left\{\left[x(j_{l-1}(x)+iy_{l-1}(x))-l(j_{l}(x)+iy_{l}(x))\right]\eta^{2}j_{l}(bx)\right.\\ \left.-\left[bxj_{l-1}(bx)-lj_{l}(bx)\right](j_{l}(x)+iy_{l}(x))\right\}=0. \quad \text{(B.12)}\end{aligned}$$

The next step is to separate the real and imaginary parts, which we can do as long as m is a real number (that is, neglecting absorption in the sphere medium):

$$\begin{aligned}&\beta\left\{\left[xj_{l-1}(x)-lj_{l}(x)\right]\eta^{2}j_{l}(bx)-\left[bxj_{l-1}(bx)-lj_{l}(bx)\right]j_{l}(x)\right\}\\ &\quad+i\beta\left\{\left[xy_{l-1}(x)-ly_{l}(x)\right]\eta^{2}j_{l}(bx)-\left[bxj_{l-1}(bx)-lj_{l}(bx)\right]y_{l}(x)\right\}=0. \quad \text{(B.13)}\end{aligned}$$

Now, both real and imaginary parts must be zero, so we can take either one to solve for x. Let's try with the imaginary part

$$\begin{aligned}&\left[xy_{l-1}(x)-ly_{l}(x)\right]\eta^{2}j_{l}(bx)-\left[bxj_{l-1}(bx)-lj_{l}(bx)\right]y_{l}(x)=0, \quad \text{(B.14)}\\ &\eta^{2}xj_{l}(bx)y_{l-1}(x)-\eta^{2}lj_{l}(bx)y_{l}(x)-bxj_{l-1}(bx)y_{l}(x)+lj_{l}(bx)y_{l}(x)=0.\end{aligned}$$

We finally arrive to an equation to solve involving only real spherical Bessel func-

tions,

$$\eta^2 x j_l(bx) y_{l-1}(x) - l(\eta^2 - 1) j_l(bx) y_l(x) - bx j_{l-1}(bx) y_l(x) = 0. \tag{B.15}$$

The spherical Bessel functions are defined as

$$z_l(x) = \sqrt{\frac{\pi}{2x}} Z_{l+1/2}(x). \tag{B.16}$$

We can use this to write equation B.15 using regular Bessel functions, obtaining an equation that is straightforward to solve numerically:

$$\eta^2 J_{l+1/2}(bx) Y_{l-1/2}(x) - \frac{l(\eta^2 - 1)}{x} J_{l+1/2}(bx) Y_{l+1/2}(x) - b J_{l-1/2}(bx) Y_{l+1/2}(x) = 0. \tag{B.17}$$

See Ref. [103] for a calculation.

Bibliography

[1] STM Project: Disk scanner. http://www.geocities.com/spm_stm/Disk_Scanner_Exp.html.

[2] Milton Abramowitz and Irene A. Stegun, editors. *Handbook of Mathematical Functions*. Dover Publications, New York, 1965.

[3] Yoshihiro Akahane, Takashi Asano, Bong-Shik Song, and Susumu Noda. High-Q photonic nanocavity in a two-dimensional photonic crystal. *Nature*, 425:944–947, 2003.

[4] A. P. Alivisatos. Perspectives on the physical chemistry of semiconductor nanocrystals. *J. Phys. Chem*, 100(31):13226–13239, 1996.

[5] L. Allen and J. H. Eberly. *Optical resonance and two-level atoms*. Dover Publishing, Mineola, NY, 1987. Reprint from: NewYork, Wiley 1975.

[6] Vilson R. Almeida, Carlos A. Barrios, Roberto R. Panepucci, and Michal Lipson. All-optical control of light on a silicon chip. *Nature*, 431:1081–1084, October 2004.

[7] Lucio Claudio Andreani, Giovanna Panzarini, and Jean-Michel Gèrard. Strong-coupling regime for quantum boxes in pillar microcavities: Theory. *Physical Review B*, 60(19):13276–13279, November 1999.

[8] Takao Aok, Barak Dayan, E. Wilcut, W. P. Bowen, A. S. Parkins, T. J.

Kippenberg, K. J. Vahala, and H. J. Kimble. Observation of strong coupling between one atom and a monolithic microresonator. *Nature*, 443:671–674, 2006.

[9] Andrea M. Armani and Kerry J. Vahala. Heavy water detection using ultra-high-Q microcavities. *Optics Letters*, 31:1896–1898, June 2006.

[10] S. Arnold, M. Khoshsima, I. Teraoka, S. Holler, and F. Vollmer. Shift of whispering-gallery modes in microspheres by protein adsorption. *Optics Letters*, 28:272–274, February 2003.

[11] T. Asano, B. S. Song, Y. Akahane, and S. Noda. Ultrahigh-Q nanocavities in two-dimensional photonic crystal slabs. *IEEE Journal of Selected Topics In Quantum Electronics*, 12:1123–1134, 2006.

[12] Neil W. Ashcroft and N. David Mermin. *Solid State Physics*. Saunders College Publishing, Philadelphia, 1976.

[13] G. Bacher, R. Weigand, J. Seufert, V. D. Kulakovskii, N. A. Gippius, A. Forchel, K. Leonardi, and D. Hommel. Biexciton versus exciton lifetime in a single semiconductor quantum dot. *Physical Review Letters*, 83(21):4417–4420, Nov 1999.

[14] Antonio Badolato, Kevin Hennessy, Mete Atatüre, Jan Dreiser, Evelyn Hu, Pierre M. Petroff, and Atac Imamoglu. Deterministic coupling of single quantum dots to single nanocavity modes. *Science*, 308(5725):1158–1161, May 2005.

[15] O. Baklenov, H. Nie, J. Cambell, B. G. Streetman, and A. L. Holmes Jr. Long-wavelength luminescence from $In_{0.5}Ga_{0.5}As$/GaAs quantum dots grown by migration enhanced epitaxy. *Journal of Vacuum Science & Technology B*, 17(3):1124–1126, May 1999.

[16] E. T. Batteh, Jun Cheng, Gang Chen, D. G. Steel, D. G. Gammon, D. S. Katzer, and D. Park. Coherent nonlinear optical spectroscopy of fluctuation quantum dots: Evidence for coupling between quantum dots. *Physical Review B*, 71(15):155237, April 2005.

[17] M. Bayer and A. Forchel. Temperature dependence of the exciton homogeneous linewidth in $In_{0.60}Ga_{0.40}as/GaAs$ self-assembled quantum dots. *Physical Review B*, 65:041308, November 2002.

[18] M. Bayer, P. Hawrylak, K. Hinzer, S. Fafard, M. Korkusinski, Z. R. Wasilewski, O. Stern, and A. Forchel. Coupling and entangling of quantum states in quantum dot molecules. *Science*, 291(5503):451–463, January 2001.

[19] M. Bayer, A. Kuther, A. Forchel, A. Gorbunov, V. B. Timofeev, F. Schäfer, J. P. Reithmaier, T. L. Reinecke, and S. N. Walck. Electron and hole g factors and exchange interaction from studies of the exciton fine structure in $in_{0.60}ga_{0.40}as$ quantum dots. *Physical Review Letters*, 82(8):1748–1751, Feb 1999.

[20] M. Bayer, O. Stern, P. Hawrylak, S. Fafard, and A. Forchel. Hidden symmetries in the energy levels of excitonic 'artificial atoms'. *Nature*, 405:923–926, June 2000.

[21] G. J. Beirne, C. Hermannstädter, L. Wang, A. Rastelli, O. G. Schmidt, and P. Michler. Quantum light emission of two lateral tunnel-coupled (In,Ga)As/GaAs quantum dots controlled by a tunable static electric field. *Physical Review Letters*, 96(13):137401, April 2006.

[22] John S. Bell. On the Einstein Podolsky Rosen paradox. *Physics*, 1:195–200, 1964.

[23] Charles H. Bennett, Ethan Bernstein, Gilles Brassard, and Umesh Vazirani. Strengths and weaknesses of quantum computing. *SIAM J. Comput.*, 26(5):1510–1523, October 1997.

[24] André Berthiaume and Gilles Brassard. Oracle quantum computing. *Journal of Modern Optics*, 41(12):2521–2535, December 1994.

[25] P. Bianucci, A. Muller, C. K. Shih, Q. Q. Wang, Q. K. Xue, and C. Piermarocchi. Experimental realization of the one qubit Deutsch-Jozsa algorithm in a quantum dot. *Physical Review B*, 69(16):161303(R), April 2004.

[26] Pablo Bianucci, Chris Fietz, John W. Robertson, Gennady Shvets, and Chih-Kang Shih. Whispering gallery mode microresonators as polarization converters. *Optics Letters*, 2007. In press.

[27] E. Biolatti, I. D'Amico, P. Zanardi, and F. Rossi. Electro-optical properties of semiconductor quantum dots: Application to quantum information processing. *Phys. Rev. B*, 65:075306, January 2002.

[28] D. Birkedal, K. Leosson, and J. M. Hvam. Long lived coherence in self-assembled quantum dots. *Phys. Rev. Lett.*, 87(22):227401, November 2001.

[29] Timothy A. Birks and Youwei W. Li. The shape of fiber tapers. *J. Lightwave Technol.*, 10:432–438, April 1992.

[30] R. Blatt, H. Häffner, C. F. Roos, C. Becher, and F. Schmidt-Kaler. Ion trap quantum computing with Ca^+ ions. *Quantum Information Processing*, 3(1-5):61–73, October 2004.

[31] Craig F. Bohren and Donald R. Huffman. *Absorption and Scattering of Light by Small Particles*. John Wiley & Sons, New York, 1983.

[32] N. H. Bonadeo, J. Erland, D. Gammon, D. Park, D. S. Katzer, and D. G. Steel. Coherent optical control of the quantum state of a single quantum dot. *Science*, 282:1473, November 1998.

[33] P. Borri, W. Langbein, S. Scheider, U. Woggon, R. L. Selin, D. Ouyang, and D. Bimberg. Ultralong dephasing time in InGaAs quantum dots. *Physics Review Letters*, 87(15):157401, October 2001.

[34] P. Borri, W. Langbein, S. Schneider, U. Woggon, R. L. Sellin, D. Ouyang, and D. Bimberg. Rabi oscillations in the excitonic ground-state transition of InGaAs quantum dots. *Physical Review B*, 66(8):081306, Aug 2002.

[35] Robert W. Boyd and John E. Heebner. Sensitive disk resonator photonic biosensor. *Applied Optics*, 40(31):5742–5747, 2001.

[36] V. B. Braginsky, M. L. Gorodetsky, and V. S. Ilchenko. Quality-factor and nonlinear properties of optical whispering-gallery modes. *Physics Letters A*, 137(7-8):393–397, May 1989.

[37] R. Hanbury Brown and R. Q. Twiss. Correlation between photons in two coherent beams of light. *Nature*, 177:27–29, January 1956.

[38] Ming Cai, Oskar Painter, and Kerry J. Vahala. Observation of critical coupling in a fiber taper to a silica-microsphere whispering-gallery mode system. *Physical Review Letters*, 85:74–77, July 2000.

[39] Ming Cai and Kerry Vahala. Highly efficient optical power transfer to whispering-gallery modes by use of a symmetrical dual-coupling configuration. *Optics Letters*, 25(4):260–262, 2000.

[40] T. Calarco, A. Datta, P. Fedichev, E. Pazy, and P. Zoller. Spin-based all-optical quantum computation with quantum dots: Understanding and suppressing decoherence. *Physical Review A*, 68(1):012310, July 2003.

[41] I. L. Chuang and Y. Yamamoto. Simple quantum computer. *Phys. Rev. A*, 52(5):3489, November 1995.

[42] John F. Clauser and Michael A. Horne. Experimental consequences of objective local theories. *Physical Review D*, 10(2):526–535, July 1974.

[43] R. Cleve, A. Ekert, C. Macchiavello, and M. Mosca. Quantum algorithms revisited. *Proc. R. Soc. Lond. A*, 454(1969):339, January 1998.

[44] D. Collins, K. W. Kim, and W. C. Holton. Deutsch-Josza algorithm as a test of quantum computation. *Phys. Rev. A*, 58(3):R1633–R1636, September 1998.

[45] D. G. Cory, R. Laflamme, E. Knill, L. Viola, T. F. Havel, N. Boulan, G. Boutis, E. Fortunato, S. Lloyd, and R. Martinez. Nmr based quantum information processing: Achievements and prospects. *Fortschritte der Physik*, 48(9-11):875–907, October 2000.

[46] D. Deutsch and R. Jozsa. Rapid solutions of problems by quantum computation. *Proc. R. Soc. Lond. A*, 439(1907):553–558, December 1992.

[47] M. H. Devoret, A. Wallraff, and J. M. Martinis. Superconducting qubits: A short review. 2004.

[48] Timothy E. Dimmick, George Kakarantzas, Timothy A. Birks, and Philip St. J. Russell. Carbon dioxide laser fabrication of fused-fiber couplers and tapers. *Applied Optics*, 38(33):6845–6848, 1999.

[49] David P. DiVincenzo. The physical implementation of quantum computation. *Fortschritte der Physik*, 48(9-11):771–783, 2000.

[50] M. V. Gudurev Dutt, Jun Cheng, Bo Li, Xiaodong Xu, Xiaoqin Li, P. R. Berman, D. G. Steel, A. S. Bracker, D. Gammon, Sophia E. Economou, Ren-Bao Li, and L. J. Sham. Stimulated and spontaneous optical generation of

electron spin coherence in charged GaAs quantum dots. *Physical Review Letters*, 94(22):227403, June 2005.

[51] Dirk Englund, David Fattal, Edo Waks, Glenn Solomon, Bingyang Zhang, Toshihiro Nakaoka, Yasuhiko Arakawa, Yoshihisa Yamamoto, and Jelena Vuckovic. Controlling the spontaneous emission rate of single quantum dots in a two-dimensional photonic crystal. *Physical Review Letters*, 95(1):013904, July 2005.

[52] Peter Fairley. The microphotonics revolution. *Technol. Rev.*, 103(4):38–44, 2000.

[53] W. Fang, J. Y. Xu, A. Yamilov, H. Cao, Y. Ma, S. T. Ho, and G. S. Solomon. Large enhancement of spontaneous emission rates of InAs quantum dots in GaAs microdisks. *Optics Letters*, 27:948–950, 2002.

[54] D. Fattal, C. Santori, J. Vuckovic, G. S. Solomon, and Y. Yamamoto. Indistinguishable single photons from a quantum dot. *Physica Status Solidi(b)*, 238(2):305–308, 2003.

[55] Richard P. Feynman. There's plenty of room at the bottom. *Engineerring and Science*, 23(5):22–36, February 1960. http://www.zyvex.com/nanotech/feynman.html.

[56] J. J. Finley, A. D. Ashmore, A. Lemaître, D. J. Mowbray, M. S. Skolnick, I. E. Itskevich, P. A. Maksym, M. Hopkinson, and T. F. Krauss. Charged and neutral exciton complexes in individual self-assembled In(Ga)As quantum dots. *Physical Review B*, 63(7):073307, Jan 2001.

[57] J. Förstner, C. Weber, J. Danckwerts, and A. Knorr. Phonon-assisted damping of rabi oscillations in semiconductor quantum dots. *Physical Review Letters*, 91(12):127401, September 2003.

[58] Toshimasa Fujisawa, Tjerk H. Oosterkamp, Wilfred G. van der Wiel, Benno W. Broer, Ramón Aguado, Seigo Tarucha, and Leo P. Kouwenhoven. Spontaneous emission spectrum in double quantum dot devices. *Science*, 282(5390):932–935, October 1998.

[59] D. Gammon, E. S. Snow, B. V. Shanabrook, D. S. Katser, and D. Park. Fine structure splitting in the optical spectra of single GaAs quantum dots. *Physical Review Letters*, 76(16):3005–3008, April 1996.

[60] D. Gammon, E. S. Snow, B. V. Shanabrook, D. s. Katzer, and D. Park. Homogeneous linewidths in the optical spectrum of a single gallium arsenide quantum dot. *Science*, 273(5271):87–90, July 1996.

[61] B. Gayral and J. M. Gérard. Strong purcell effect for InAs quantum boxes in high-Q wet-etched microdisks. *Physica E: Low-dimensional Systems and Nanostructures*, 7(3-4):641–645, 2000.

[62] J. M. Gérard, B. Sermage, B. Gayral, B. Legrand, E. Costard, and V. Thierry-Mieg. Enhanced spontaneous emission by quantum boxes in a monolithic optical microcavity. *Physical Review Letters*, 81(5):1110–1113, August 1998.

[63] Jean-Michel Gérard. *Single Quantum Dots: Fundamentals, Applications and New Concepts*, chapter 7, pages 269–314. Topics in Applied Physics. Springer-Verlag, Berlin, Germany, 2003.

[64] J.M. Gérard, D. Barrier, J.Y. Marzin, R. Kuszelewicz, L. Manin, E. Costard, V. Thierry-Mieg, and T. Rivera. Quantum boxes as active probes for photonic microstructures: The pillar microcavity case. *Applied Physics Letters*, 69:449, 1996.

[65] J.M. Gérard and B. Gayral. Strong purcell effect for InAs quantum boxes in

three-dimensional solid-state microcavities. *Journal of Lightwave Technology*, 17(11):2089–2095, 1999.

[66] M. L. Gorodetsky and V. S. Ilchenko. High-Q optical whispering-gallery microresonators: precession approach for spherical mode analysis and emission patterns with prism couplers. *Optics Communications*, 113(1-3):133–143, 1994.

[67] M. L. Gorodetsky, A. A. Savchenkov, and V. S. Ilchenko. Ultimate Q of optical microsphere resonators. *Optics Letters*, 21:453–455, April 1996.

[68] Michael L. Gorodetsky, Andrew D. Pryamikov, and Vladimir S. Ilchenko. Rayleigh scattering in high-Q microspheres. *Journal of the Optical Society of America B*, 17(6):1051–1057, 2000.

[69] M.L. Gorodetsky and V.S. Ilchenko. Optical microsphere resonators: optimal coupling to high-q whispering-gallery modes. *Journal of the Optical Society of America B*, 16(1):147–154, 1999.

[70] Gloria Griffel, Stephen Arnold, Dogan Taskent, Ali Serpengüzel, John Connolly, and Nancy Morris. Morphology-dependent resonances of a microsphere-optical fiber system. *Opt. Lett.*, 21(10):695–697–, 1996.

[71] M. Grundmann, J. Christen, N. N. Ledentsov, J. Böhrer, D. Bimberg, S. S. Ruvimov, ‡, P. Werner, U. Richter, U. Gösele, J. Heydenreich, V. M. Ustinov, A. Yu. Egorov, A. E. Zhukov, P. S. Kop'ev, and Zh. I. Alferov. Ultranarrow luminescence lines from single quantum dots. *Phys. Rev. Lett.*, 74(20):4043–4046, May 1995.

[72] G. Guan, S. Arnold, and M. V. Otugen. Temperature measurements using a microoptical sensor based on whispering gallery modes. *AIAA journal*, 44(10):2385–2389, 2006.

[73] J. R. Guest, T. H. Stievater, X. Li, Jun Cheng, D. G. Steel, D. Gammon, D. S. Katzer, D. Park, C. Ell, A. Traänhardt, G. Khitrova, and H. M. Gibbs. Measurement of optical absorption by a single quantum dot exciton. *Physical Review B*, 65(24):241310(R), June 2002.

[74] Niranjan M. Hanumegowda, Caleb J. Stica, Bijal C. Patel, Ian White, and Xudong Fan. Refractometric sensors based on microsphere resonators. *Applied Physics Letters*, 87:201107, 2005.

[75] A. Hartmann, L. Loubies, F. Reinhardt, and E. Kapon. Self-limiting growth of quantum dot heterostructures on nonplanar 111b substrates. *Applied Physics Letters*, 71(10):1314–1316, September 1997.

[76] Jeff Hecht. *City of Light: The Story of Fiber Optics*. Oxford University Press US, 1999.

[77] D. J. Heinzen, J. J. Childs, J. E. Thomas, and M. S. Feld. Enhanced and inhibited visible spontaneous emission by atoms in a confocal resonator. *Physical Review Letters*, 58(13):1320–1323, March 1987.

[78] K. Hennessy, A. Badolato, M. Winger, D. Gerace, M. Atatiüre, S. Gulde, S. Falt, E. L. Hu, and A. Imamoglu. Quantum nature of a strongly coupled single quantum dot-cavity system. *Nature*, 445:896–899, 2007.

[79] H. Htoon, J. W. Keto, O. Baklenov, Jr. A. L. Holmes, and C. K. Shih. Cross-sectional nanophotoluminescence studies of Stark effects in self-assembled quantum dots. *Appl. Phys. Lett.*, 76(6):700, February 2000.

[80] H. Htoon, D. Kulik, O. Baklenov, Jr. A. L. Holmes, T. Takagahara, and C. K. Shih. Carrier relaxation and quantum decoherence of excited states in self-assembled quantum dots. *Physical Review B*, 63(24):241303(R), June 2001.

[81] H. Htoon, T. Takagahara, D. Kulik, O. Baklenov, A. L. Holmes Jr., and C. K. Shih. Interplay of rabi oscillations and quantum interference in semiconductor quantum dots. *Physical Review Letters*, 88(8):087401, February 2002.

[82] H. Htoon, H. Yu, D. Kulik, J. W. Keto, O. Baklenov, A. L. Holmes, B. G. Streetman, and C. K. Shih. Quantum dots at the nanometer scale: Interdot carrier shuffling and multiparticle states. *Physical Review B*, 60(15):11026, October 1999.

[83] Han Htoon. *Studies on quantum coherence phenomena of self-assembled quantum dots*. PhD thesis, The University of Texas at Austin, Austin, Texas, May 2001.

[84] Y. Z. Hu, S. W. Koch, M. Lindberg, N. Peyghambarian, E. L. Pollock, and Farid F. Abraham. Biexcitons in semiconductor quantum dots. *Physical Review Letters*, 64(15):1805–1807, Apr 1990.

[85] Vladimir S. Ilchenko, Anatoliy A. Savchenkov, Andrey B. Matsko, and Lute Maleki. Nonlinear optics and crystalline whispering gallery mode cavities. *Physical Review Letters*, 92(4):43903, 2004.

[86] Vladimir S. Ilchenko, X. Steve Yao, and Lute Maleki. Pigtailing the high-Q microsphere cavity: a simple fiber coupler for optical whispering-gallery modes. *Optics Letters*, 24(11):723–725, 1999.

[87] A. Imamoglu, D. D. Awschalom, G. Burkard, D. P. DiVincenzo, D. Loss, M. Sherwin, and A. Small. Quantum information processing using quantum dot spins and cavity qed. *Physical Review Letters*, 83(20):4204–4207, 1999.

[88] John David Jackson. Classical electrodynamics. 1999.

[89] E. T. Jaynes and Cummings F, W. Comparison of quantum and semiclassical

radiation theories with application to the beam maser. *Proceeding of the IEEE*, 51(1):89–109, 1963.

[90] B. R. Johnson. Theory of morphology-dependent resonances: shape resonances and width formulas. *Journal of the Optical Society of America A*, 10(2):343–352, 1993.

[91] Steven G. Johnson, Shanhui Fan, Pierre R. Villeneuve, J. D. Joannopoulos, and L. A. Kolodziejski. Guided modes in photonic crystal slabs. *Physical Review B*, 60(8):5751–5758, August 1999.

[92] R. C. Jones. A new calculus for the treatment of optical systems. *Journal of the Optical Society of America*, 31(7):488–493, 1941.

[93] H. Kamada, H. Gotoh, J. Temmyo, T. Takagahara, and H. Ando. Exciton Rabi oscillation in a single quantum dot. *Phys. Rev. Lett.*, 87(24):246401, December 2001.

[94] Marc A. Kastner. Artifical atoms. *Physics Today*, 46(1):24–32, January 1993.

[95] D. Kielpinski, C. Monroe, and D.J. D. J. Wineland. Architecture for a large-scale ion-trap quantum computer. *Nature*, 417(6890):709–711, June 2002.

[96] S. Kiravittaya, M. Benyoucef, R. Zapf-Gottwick, A. Rastelli, and O. G. Schmidt. Ordered GaAs quantum dot arrays on GaAs(001): Single photon emission and fine structure splitting. *Applied Physics Letters*, 89(23):233102, December 2006.

[97] J. C. Knight, G. Cheung, F. Jacques, and T. A. Birks. Phase-matched excitation of whispering-gallery-mode resonances by a fiber taper. *Optics Letters*, 22:1129–1131, August 1997.

[98] Emanuel Knill, Raymond Laflamme, and Wojciech H. Zurek. Resilient quantum computation. *Science*, 279(5349):342–345, January 1998.

[99] Hidenori Konishi, Hideki Fujiwara, Shigeki Takeuchi, and Keiji Sasaki. Polarization-discriminated spectra of a fiber-microsphere system. *Applied Physics Letters*, 89:121107, September 2006.

[100] F. H. L. Koppens, C. Buizert, K. J. Tielrooij, I. T. Vink, K. C. Nowack, T. Meunier, L. P. Kouwenhoven, and L. M. L. Vandersypen. Driven coherent oscillations of a single electron spin in a quantum dot. *Nature*, 442:776–771, August 2006.

[101] H. J. Krenner, M. Sabathil, E. C. Clark, A. Kress, D. Schuh, M. Bichler, G. Abstreiter, and J. J. Finley. Direct observation of controlled coupling in an individual quantum dot molecule. *Physical Review Letters*, 94(5):057402, February 2005.

[102] Scott Lacey, Hailin Wang, David H. Foster, and Jens U. Nöckel. Directional tunneling escape from nearly spherical optical resonators. *Physical Review Letters*, 91(3):033902, July 2003.

[103] M. Lalín. Mahler measure and volumes in hyperbolic space. *Geometriae Dedicata*, 107:211–234, 2004.

[104] C. C. Lam, P. T. Leung, and K. Young. Explicit asymptotic formulas for the positions, widths, and strengths of resonances in Mie scattering. *Journal of the Optical Society of America B*, 9(9):1585–1592, 1992.

[105] X. Li, Y. Wu, D. Steel, D. Gammon, T. H. Stievater, D. S. Katzer, D. Park, C. Piermarocchi, and L. J. Sham. An all-optical quantum gate in a semiconductor quantum dot. *Science*, 301:809–811, August 2003.

[106] H. Lipsanen, M. Sopanen, and J. Ahopelto. Luminescence from excited states in strain-induced $In_xGa_{1-x}As$ quantum dots. *Physical Review B*, 51(19):13868–13871(R), May 1995.

[107] B. E. Little, S. T. Chu, H. A. Haus, J. Foresi, and J. P. Laine. Microring resonator channel dropping filters. *Journal of Lightwave Technology*, 15(6):998–1005, 1997.

[108] B.E. Little, S. T. Chu, P. P. Absil, J. V. Hryniewicz, F. G. Johnson, F. Seiferth, D. Gill, V. Van, O. King, and M. Trakalo. Very high-order microring resonator filters for wdm applications. *IEEE Photonics Technology Letters*, 16(10):2263–2265, 2004.

[109] Brent E. Little and Sai T. Chu. Theory of polarization rotation and conversion in vertically coupled microresonators. *IEEE Photonic Technology Letters*, 12:401–403, April 2000.

[110] Brendon W. Lovett, John H. Reina, Ahsan Nazir, and G. Andrew D. Briggs. Optical schemes for quantum computation in quantum dot molecules. *Physical Review B*, 68(20):205319, November 2003.

[111] J. Y. Marzin, J. M. Gérard, A. Izraël, D. Barrier, and G. Bastard. Photoluminescence of single InAs quantum dots obtained by self-organized growth on GaAs. *Physical Review Letters*, 73(5):716–719, Aug 1994.

[112] Andrey B. Matsko and Vladimir S. Ilchenko. Optical resonators with whispering-gallery-modes–part I: Basics. *IEEE Journal of Selected Topics in Quantum Electronics*, 12:3–14, February 2006.

[113] Pierre Meystre and Murray Sargent III. *Elements of Quantum Optics*. Springer-Verlag, Berlin, 3rd edition, 1998.

[114] B. R. Mollow. Power spectrum of light scattered by two-level systems. *Physical Review*, 188(5):1969–1975, December 1969.

[115] Gordon E. Moore. Cramming more components onto integrated circuits. *Electronics*, 38(8), April 1965. http://www.intel.com/technology/mooreslaw/.

[116] A. Muller, E. B. Flagg, P. Bianucci, X. Y. Wang, D. G. Deppe, W. Ma, J. Zhang, G. J. Salamo, M. Xiao, and C. K . Shih. Resonance fluorescence from a coherently driven semiconductor quantum dot in a cavity. May 2007.

[117] A. Muller, D. Lu, J. Ahn, D. Gazula, S. Quadery, S. Freisem, D. G. Deppe, and C. K. Shih. Self-aligned all-epitaxial microcavity for cavity QED with quantum dots. *Nano Letters*, 6(12):2920–2924, 2006.

[118] A. Muller, C.K. Shih, J. Ahn, D. Lu, and D.G. Deppe. Isolated single quantum dot emitters in all-epitaxial microcavities. *Optics Letters*, 31(4):528–530, 2006.

[119] A. Muller, Q. Q. Wang, P. Bianucci, and C. K. Shih. Determination of anisotropic dipole moments in self-assembled quantum dots using Rabi oscillations. *Applied Physics Letters*, 84(6):981–983, February 2004.

[120] Andreas Muller. *Resonance Fluorescence and Cavity Quantum Electrodynamics with Quantum Dots*. PhD thesis, The University of Texas at Austin, Austin, Texas, May 2007.

[121] Ahmer Naweed, G. Farca, S. I. Shopova, and A. T. Rosenberger. Induced transparency and absorption in coupled whispering-gallery microresonators. *Physical Review A*, 71(4):43804, 2005.

[122] R. G. Neuhauser, K. T. Shimizu, W. K. Woo, S. A. Empedocles, and M. G. Bawendi. Correlation between fluorescence intermittency and spectral diffusion in single semiconductor quantum dots. *Physical Review Letters*, 85(15):3301–3304, Oct 2000.

[123] Michael A. Nielsen and Isaac L. Chuang. *Quantum Computation and Quantum Information*. Cambridge University Press, 2000.

[124] Jens U. Nöckel and A. Douglas Stone. Ray and wave chaos in asymmetric resonant optical cavities. *Nature*, 385:45–47, 1997.

[125] G. Ortner, M. Bayer, A. Larionov, V. B. Timofeev, A. Forchel, Y. B. Lyanda-Geller, T. L. Reinecke, P. Hawrylak, S. Fafard, and Z. Wasilewski. Fine structure of excitons in InAs/GaAs coupled quantum dots: A sensitive test of electronic coupling. *Physical Review Letters*, 90(8):086404, February 2008.

[126] Young-Shin Park, Andrew K. Cook, and Hailin Wang. Cavity QED with diamond nanocrystals and silica microspheres. *Nano Letters*, 6:2075–2079, August 2006.

[127] B. Patton, U. Woggon, and W. Langbein. Coherent control and polarization readout of individual excitonic states. *Physical Review Letters*, 95(26):266401, 2005.

[128] E. Peter, P. Senellart, D. Martrou, A. Lemaître, J. Hours, J. M. Gèrard, and J. Bloch. Exciton-photon strong-coupling regime for a single quantum dot embedded in a microcavity. *Physical Review Letters*, 95(6):067401, August 2005.

[129] Pierre M. Petroff, Axel Lorke, and Atac Imamoglu. Epitaxially self-assembled quantum dots. *Physics Today*, 54(5):46, May 2001.

[130] Alberto Pimpinelli. *Physics of Crystal Growth*. Cambridge University Press, 1998.

[131] David Press, Stephan Götzinger, Stephan Reitzenstein, Carolin Hofmann, Andreas Löffler, Martin Kamp, Alfred Forchel, and Yoshihisa Yamamoto. Pho-

ton antibunching from a single quantum-dot-microcavity system in the strong coupling regime. *Physical Review Letters*, 98:117402, 2007.

[132] I. Protsenko, P. Domokos, V. Lefèvre-Seguin, J. Hare, J. M. Raimond, and L. Davidovich. Quantum theory of a thresholdless laser. *Physical Review A*, 59(2):1667–1682, February 1999.

[133] E. M. Purcell, H. C. Torrey, and R. V. Pound. Resonance absorption by nuclear magnetic moments in a solid. *Physical Review*, 69(1-2):37–38, January 1946.

[134] J. P. Reithmaier, G. Sek, A. Löffler, C. Hofmann, S. Kuhn, S. Reitzenstein, L. V. Keldysh, V. D. Kulakovskii, T. L. Reinecke, and A. Forchel. Strong coupling in a single quantum dot-microcavity system. *Nature*, 432:197–200, November 2004.

[135] Jun John Sakurai. *Modern Quantum Mechanics*. Addison-Wesley Publishing Company, revised edition, 1995.

[136] S. Schiller. Asymptotic expansion of morphological resonance frequencies in Mie scattering. *Applied Optics*, 32(12):2181–2185, 1993.

[137] K. H. Schmidt, G. Medeiros-Ribeiro, and P. M. Petroff. Photoluminescence of charged InAs self-assembled quantum dots. *Physical Review B*, 58(7):3597–3600, Aug 1998.

[138] M. Schwab, H. Kurtze, T. Auer, T. Berstermann, M. Bayer, J. Wiersig, N. Baer, C. Gies, F. Jahnke, JP Reithmaier, et al. Radiative emission dynamics of quantum dots in a single cavity micropillar. *Physical Review B*, 74(4):45323, 2006.

[139] Bruce W. Shore and Peter L. Knight. The jaynes-cummings model. *Journal of Modern Optics*, 40(7):1195–1238, July 1993.

[140] David D. Smith, Hongrok Chang, and Kirk. A. Fuller. Whispering-gallery mode splitting in coupled microresonators. *Journal of the Optical Society of America B*, 20:1967–1974, September 2003.

[141] S. M. Spillane, T. J. Kippenberg, O. J. Painter, and K. J. Vahala. Ideality in a fiber-taper-coupled microresonator system for application to cavity quantum electrodynamics. *Physical Review Letters*, 91(4):043902, July 2003.

[142] Kartik Srinivasan, Matthew Borselli, Thomas J. Johnson, Paul E. Barclay, Oskar Painter, Andreas Stintz, and Sanjay Krishna. Optical loss and lasing characteristics of high-quality-factor algaas microdisk resonators with embedded quantum dots. *Applied Physics Letters*, 86:151106, 2005.

[143] M. Steffen, M. Ansmann, R. C. Bialczak, N. Katz, E. Lucero, R. McDermott, M. Neeley, E. M. Weig, A. N. Cleland, and J. M. Martinis. Measurement of the entanglement of two superconducting qubits via state tomography. *Science*, 313(5792):1423, 2006.

[144] T. H. Stievater, X. Li, D. G. Steel, D. Gammon, D. S. Katzer, D. Park, C. Piermarocchi, and L. J. Sham. Rabi oscillations of excitons in single quantum dots. *Physics Review Letters*, 87(13):133603, September 2001.

[145] T. H. Stievater, Xiaoqin Li, D. G. Steel, D. Gammon, D. S. Katzer, and D. Park. Transient nonlinear spectroscopy of excitons and biexcitons in single quantum dots. *Physical Review B*, 65(20):2205319, May 2002.

[146] L. F. Stokes, M. Chodorow, and H. J. Shaw. All-single-mode fiber resonator. *Optics Letters*, 7(6):288–290, June 1982.

[147] N. G. Stoltz, M. Rakher, S. Strauf, A. Badolato, D. D. Lofgreen, P. M. Petroff, L.A. Coldren, and D. Bouwmeester. High-quality factor optical microcavities using oxide apertured micropillars. *Applied Physics Letters*, 87:031105, 2005.

[148] S. Strauf, K. Hennessy, MT Rakher, Y.S. Choi, A. Badolato, LC Andreani, EL Hu, PM Petroff, and D. Bouwmeester. Self-tuned quantum dot gain in photonic crystal lasers. *Physical Review Letters*, 96(12):127404, 2006.

[149] S. Stufler, P. Machnikowski, P. Ester, M. Bichler, V. M. Axt, T. Kuhn, and A. Zrenner. Two-photon Rabi oscillations in a single $In_xGa_{1-x}As$/GaAs quantum dot. *Physical Review B*, 73(12):125304, 2006.

[150] M. Sumetsky, Y. Dulashko, and A. Hale. Fabrication and study of bent and coiled free silica nanowires: Self-coupling microloop optical interferometer. *Optics Express*, 12(15):3521–3531, 2004.

[151] Iwao Teraoka, Stephen Arnold, and Frank Vollmer. Perturbation approach to resonance shifts of whispering-gallery modes in a dielectric microsphere as a probe of a surrounding medium. *Journal of the Optical Society of America B*, 20(9):1937–1946, 2003.

[152] R. J. Thompson, G. Rempe, and H. J. Kimble. Observation of normal-mode splitting for an atom in an optical cavity. *Physical Review Letters*, 68(8):1132–1135, February 1992.

[153] Y. Toda, O. Moriwaki, M. Nishioka, and Y. Arakawa. Efficient carrier relaxation mechanism in InGaAs/GaAs self-assembled quantum dots based on the existence of continuum states. *Physical Review Letters*, 82(20):4114–4117, May 1999.

[154] F. Treussart, V. S. Ilchenko, J.F. Roch, J. Hare, V. Lefèvre-Seguin, J. M. Raimond, and S. Haroche. Evidence for intrinsic Kerr bistability of high-Q microsphere resonators in superfluid helium. *The European Physical Journal D*, 1(3):235–238, 1998.

[155] F. Troiani, U. Hohenester, and E. Molinari. Exploiting exciton-exciton interactions in semiconductor quantum dots for quantum-information processing. *Physical Review B*, 62(4):R2263, July 2000.

[156] Kerry J. Vahala. Optical microcavities. *Nature*, 424:839–846, August 2003.

[157] Wilfried G. J. H. M. van Sark, Patrick L. T. M. Frederix, Ageeth A. Bol, Hans C. Gerritsen, and Andries Meijerink. Blueing, bleaching, and blinking of single CdSe/ZnS quantum dots. *ChemPhysChem*, 3(10):871–879, October 2002.

[158] Gregory D. VanWiggeren and Rajarshi Roy. Transmission of linearly polarized light through a single-mode fiber with random fluctuations of birefringence. *Applied Optics*, 38:3888–3892, 1999.

[159] A. Vasanelli, R. Ferreira, and G. Bastard. Continuous absorption background and decoherence in quantum dots. *Physical Review Letters*, 89(21):216804, November 2002.

[160] D. W. Vernooy, V. S. Ilchenko, H. Mabuchi, E. W. Streed, and H.J. Kimble. High-Q measurements of fused-silica microspheres in the near infrared. *Optics Letters*, 23(4):247–249, 1998.

[161] J. M. Villas-Bôas, S. E. Ulloa, and A. O. Govorov. Decoherence of Rabi oscillations in a single quantum dot. *Physical Review Letters*, 94(5):57404, 2005.

[162] F. Vollmer, D. Braun, A. Libchaber, M. Khoshsima, I. Teraoka, and S. Arnold. Protein detection by optical shift of a resonant microcavity. *Applied Physics Letters*, 80:4057–4059, May 2002.

[163] Frank Vollmer, Stephen Arnold, Dieter Braun, Iwao Teraoka, and Albert

Libchaber. Multiplexed DNA quantification by spectroscopic shift of two microsphere cavities. *Biophysical Journal*, 85(3):1974–1979, 2003.

[164] Q. Q. Wang, A. Muller, P. Bianucci, E. Rossi, Q. K. Xue, T. Takagahara, C. Piermarocchi, A. H. MacDonald, and C. K. Shih. Decoherence processes during optical manipulation of excitonic qubits in semiconductor quantum dots. *Physical Review B*, 72(3):35306, 2005.

[165] Q. Q. Wang, A. Muller, P. Bianucci, C. K. Shih, and Q. K. Xue. Quality factors of qubit rotations in single semiconductor quantum dots. *Applied Physics Letters*, 87(3):031904, July 2005.

[166] Jonathan M. Ward, Danny G. O'Shea, Brian J. Shortt, Michael J. Morrissey, Kieran Deasy, and Sìle G. Nic Chormaic. Heat-and-pull rig for fiber taper fabrication. *Review of Scientific Instruments*, 77:083105, 2006.

[167] C. Weisbuch, R. Dingle, A. C. Gossard, and W. Wiegmann. Optical characterization of interface disorder in GaAs-$Ga_{1-x}Al_xAs$ multi-quantum well structures. *Solid State Communications*, 38(8):709–712, May 1981.

[168] Timothy D. Witham and Brent Baccala. Xoscope. http://xoscope.sourceforge.net.

[169] P. S. Wong, G. Balakrishnan, N. Nuntawong, J. Tatebayashi, and D.L. Huffaker. Controlled InAs quantum dot nucleation on faceted nanopatterned pyramids. *Applied Physics Letters*, 90:183103, 2007.

[170] Fengnian Xia, Lidija Sekaric, and Yurii Vlasov. Ultracompact optical buffers on a silicon chip. *Nature Photonics*, 1(1):65–71, January 2007.

[171] Qianfan Xu, Jagat Shakya, and Michal Lipson. Direct measurement of tunable optical delays on chip analogue to electromagnetically induced transparency. *Optics Express*, 14(14):6463–6468, 2006.

[172] Y. Yamamoto. Quantum communication and information processing with quantum dots. *Quantum Information Processing*, 5:299–311, 2006.

[173] Wang Yao, Ren-Bao Liu, and LJ Sham. Theory of control of the spin-photon interface for quantum networks. *Physical Review Letters*, 95(3):30504, 2005.

[174] T. Yoshie, A. Scherer, J. Hendrickson, G. Khitrova, H. M. Gibbs, G. Rupper, C. Ell, O. B. Shchekin, and D. G. Deppe. Vacuum Rabi splitting with a single quantum dot in a photonic crystal nanocavity. *Nature*, 432:200–203, November 2004.

[175] A. Zrenner. A closer look on single quantum dots. *Journal of Chemical Physics*, 112(18):7790, May 2000.

[176] A. Zrenner, E. Beham, S. Stufler, F. Findeis, M. Bichler, and G. Abstreiter. Coherent properties of a two-level system based on a quantum-dot system. *Nature*, 418:612, August 2002.

Vita

Pablo Bianucci was born in San Miguel de Tucumán, Tucumán, Argentina, the 4th of November, 1975, the son of Hugo Alberto Bianucci and Ruth Sofía Zagalsky. He graduated from high school ENET No. 1 (currently EET No. 4) de Avellaneda "Dr. Ernesto Longobardi", Avellaneda, Buenos Aires, Argentina, with a degree of Técnico Químico (technician in Chemistry) in 1994. He then enrolled at the Universidad of Buenos Aires, Buenos Aires, Argentina, where he received his Licenciado en Ciencias Físicas (Licenciate in Physical Sciences) degree in March 2001 and held a Teaching Assistant position from July 1999 to March 2001. In the Fall 2001 he entered the University of Texas at Austin as a graduate student in the Department of Physics, joining Prof. C. K. Shih nanoscale electronic materials research group during Summer 2002. In professor Shih's group he studied the optical properties of microsphere resonators and semiconductor quantum dots. He has held Teaching Asssistant, Assistant Instructor and Graduate Research Assistant positions during his stay at UT.

Permanent Address: 9 de Julio 179, 1° C
B1870CWC Avellaneda, Buenos Aires
Argentina

This dissertation was typeset with LaTeX 2_ε[1] by the author.

[1] LaTeX 2_ε is an extension of LaTeX. LaTeX is a collection of macros for TeX. TeX is a trademark of the American Mathematical Society.